LA-SUB. 99-12

FINAL REPORT

PART 1

RECEIVED
JUL 31 2000
OSTI

for Group MST-11
Los Alamos National Laboratory

Subcontract F01230017-3L
WEIRICH and ASSOCIATES, INC.

Task 1: Modeling Study of CO Effects on Polymer Electrolyte Fuel Cell Anodes

Task 2: Study of AC Impedance as Membrane/Electrode Manufacturing Diagnostic Tool

work performed by
Thomas E. Springer

January 30, 1998

Task 1: Modeling Study of CO Effects on PEFC Anodes

INTRODUCTION

Carbon monoxide poisoning of polymer electrolyte fuel cell anodes is a key problem to be overcome when operating a polymer electrolyte fuel cell (PEFC) on reformed fuels. CO adsorbs preferentially on the precious metal surface leading to substantial performance losses. Some recent work has explored this problem, primarily using various Pt alloys in attempts to lower the degree of surface deactivation. In their studies of hydrogen oxidation on Pt and Pt alloy (Pt/Sn, Pt/Ru) rotating disk electrodes exposed to H_2/CO mixtures, Gasteiger et al.[1,2] showed that a small hydrogen oxidation current is observed well before the onset of major CO oxidative stripping (*ca.* 0.4 V) on Pt/Ru. However, these workers concluded that such current observed at low anode overpotentials was "too low to be of practical value." Nonetheless, MST-11 researchers and others[3-5] have found experimentally that it is possible to run a PEFC, e.g., with a Pt/Ru anode, in the presence of CO levels in the range 10-100 ppm with little voltage loss. Such experimental results suggest that, in fact, PEFC operation at significant current densities under low anode overpotentials is possible in the presence of such levels of CO, even before resorting to air bleeding into the anode feed stream[6]. The latter approach has been shown to be effective in elimination of Pt anode catalyst poisoning effects at CO levels of 20-50 ppm for cells operating at 80^{o}C with low Pt catalyst loading[6]. The effect of oxygen bleeding is basically to lower P_{CO} down to extremely low levels in the anode plenum thanks to the catalytic (chemical) oxidation of CO by dioxygen at the anode catalyst[6]. In this modeling work we do not include specific description of oxygen bleeding effects and concentrate on the behavior of the anode with feed streams of H_2 or reformate containing low levels of CO.

The anode loss is treated in this work as a hydrogen and carbon monoxide electrode kinetics problem, but includes the effects of dilution of the feedstream with significant fractions of carbon dioxide and nitrogen and of mass transport losses in the gas diffusion backing. Not included in the anode model are ionic resistance and diffusion losses in the catalyst layer. We are looking to see if the overall pattern of polarization curves calculated based on such a purely kinetic model indeed mimics the central features of polarization curves observed for PEFCs operating on hydrogen with low levels of CO (see e.g., Ref. 6)

ANODE KINETIC MODEL FOR SPECIFIED H_2/CO CONCENTRATIONS

Assumptions

We assume the kinetic equations are not affected by the presence of N_2 and CO_2 except from their effect on the partial pressures of H_2 and CO. We also assume the feedstream is at all time saturated with water vapor so that we can assume the catalyst layer ionic resistance will be low enough to ignore any potential changes across the catalyst layer.

We assume the interfacial kinetics is determined by the four processes expressed in Eq. 1 to 4. By itself M corresponds to a vacant catalyst site, otherwise H or CO are attached to the site.

DISCLAIMER

This report was prepared as an account of work sponsored by an agency of the United States Government. Neither the United States Government nor any agency thereof, nor any of their employees, make any warranty, express or implied, or assumes any legal liability or responsibility for the accuracy, completeness, or usefulness of any information, apparatus, product, or process disclosed, or represents that its use would not infringe privately owned rights. Reference herein to any specific commercial product, process, or service by trade name, trademark, manufacturer, or otherwise does not necessarily constitute or imply its endorsement, recommendation, or favoring by the United States Government or any agency thereof. The views and opinions of authors expressed herein do not necessarily state or reflect those of the United States Government or any agency thereof.

DISCLAIMER

Portions of this document may be illegible in electronic image products. Images are produced from the best available original document.

$$CO + M \underset{b_{fc}k_{fc}}{\overset{k_{fc}}{\rightleftharpoons}} (M-CO) \quad [1]$$

$$H_2 + 2M \underset{b_{fh}k_{fh}}{\overset{k_{fh}}{\rightleftharpoons}} 2(M-H) \quad [2]$$

$$(M-H) \xrightarrow{k_{eh}} H^+ + e^- + M \quad [3]$$

$$H_2O + (M-CO) \xrightarrow{k_{ec}} M + CO_2 + 2H^+ + 2e^- \quad [4]$$

The first two equations represent the competing processes of CO adsorption and dissociative chemisorption of H_2. The forward rate constants for hydrogen and CO adsorption, k_{fh} and k_{fc}, are expressed in A/cm^2-atm (geometric) and the hydrogen and CO electrooxidation rate constants k_{eh} and k_{ec} are expressed in A/cm^2 in Eq. 1 to 4. The desorption rates are implicit in b_{fc} and b_{fh}, the ratio of backward to forward rate constants with units of atmospheres, i.e., the (inverse) equilibrium constants for processes (1) and (2), respectively. The current density corresponding to anodic hydrogen oxidation is generated by the third process (Eq. 3), i.e., the electrochemical oxidation of adsorbed hydrogen atoms. The fourth process (Eq. 4), corresponding to the electrochemical oxidation of CO to CO_2, reaches significant rates only at higher anode overpotentials, generating at such high overpotentials a larger number of CO-free catalyst sites under steady state conditions.

Equations 5 and 6 represent the steady state balance of equivalent current densities of adsorption, desorption, and charge transfer fluxes of carbon monoxide and of hydrogen species that will determine θ_{co}, the fraction of catalyst sites with adsorbed CO, and θ_h, the fraction with adsorbed H. The quantity ρ represents the molar areal density of catalyst sites times the Faraday constant.

$$\rho\dot{\theta}_{co} = k_{fc}P_{co}(1-\theta_{co}-\theta_h) - b_{fc}k_{fc}\theta_{co} - k_{ec}\theta_{co}e^{\frac{\eta}{b_c}} = 0 \quad [5]$$

$$\rho\dot{\theta}_h = k_{fh}P_h(1-\theta_{co}-\theta_h)^2 - b_{fh}\,k_{fh}\theta_h^2 - 2\theta_h k_{eh}\sinh\left(\frac{\eta}{b_h}\right) = 0 \quad [6]$$

$$j_h = 2k_{eh}\theta_h\sinh\left(\frac{\eta}{b_h}\right),\ j_{co} = 2k_{ec}\theta_{co}e^{\frac{\eta}{b_c}} \quad [7]$$

Expressions for the potential dependence of the current densities for hydrogen and CO oxidation, j_h and j_{co}, are given in Eq. 7. We assume a transfer coefficient of 0.5 for the electrooxidation of hydrogen, reducing the Butler-Volmer equation to a hyperbolic sine function that allows the current to go to 0 at zero overpotential. Note that the same overpotential is assumed at a given anodic potential for both H_{ads} and CO_{ads} electro-oxidation. This means that both k_{fh} and k_{fc} describe the rate of the anodic process at 0V RHE (at full surface coverage by the corresponding surface species). A Tafel relation can be used for the potential dependence of current density for CO oxidation because of its higher equilibrium potential.

This system of equations was solved analytically by Mathematica (Wolfram). Expressions for j_h and j_{co}, the current densities of hydrogen and of CO electro-oxidation, are given below in Eq. 8 and 9, in terms of: partial pressures of H_2 (P_h) and of CO (P_{co}), the forward rate constants and the equilibrium constants described above with Eq. 1 to 4, the overpotential η (vs. RHE) and effective Tafel slopes, b_h and b_c (assumed 60 mV/e-fold of current density.)

$$s_1 = k_{eh} \sinh\left(\frac{\eta}{b_h}\right)$$

$$a_1 = e^{\frac{\eta}{b_c}} k_{ec} + k_{fc}\left(b_{fc} + P_{co}\right),\ a_2 = \left(e^{\frac{\eta}{b_c}} k_{ec} + b_{fc} k_{fc}\right)^2,\ a_3 = b_{fh}\, k_{fh} + 2s_1$$

$$j_h = \frac{2s_1\left(a_1\sqrt{a_2 a_3 k_{fh} P_h + a_1^2 s_1^2} - a_1^2 s_1 - a_2 k_{fh} P_h\right)}{k_{fh}\left(b_{fh} a_1^2 - a_2 P_h\right)} \qquad [8]$$

$$j_{co} = \frac{2e^{\frac{\eta}{b_c}} k_{ec} k_{fc} P_{co}\left(a_1 b_{fh} k_{fh} + a_1 s_1 - \sqrt{a_2 b_{fh} k_{fh}^2 P_h + 2a_2 k_{fh} P_h s_1 + a_1^2 s_1^2}\right)}{k_{fh}\left(b_{fh} a_1^2 - a_2 P_h\right)} \qquad [9]$$

Applications of Equations 8 and 9

We first consider a base case using representative values of electrochemical and adsorption rate constants that would reflect the documented behavior of Pt/hydrogen and Pt/CO chemical and electrochemical systems near 80°C. Our goal is to determine whether qualitatively correct behavior of hydrogen PEFC anode polarization in the presence of CO can be obtained from this simple kinetic model. Table I lists the set of representative model parameters selected for the match. It can be recognized that values chosen reflect basic documented characteristics of this interfacial system , e.g., equilibrium coverage by CO is substantial (at 80°C) at partial pressures of CO as low as 10-100 ppm (see value chosen for b_{fc}), the rate of H_{ads} electro-oxidation at 0V is high (see k_{fh}) whereas the rate of CO_{ads} electro-oxidation at 0V is extremely low (see k_{fc}). This choice of parameters thus describes a catalyst surface with (a) highly preferential adsorption of CO from a CO/H_2 mixture and (b) a much higher specific rate per catalyst site at low anodic potentials for hydrogen electrooxidation vs. CO electrooxidation. These two key features determine the behavior of Pt-based PEFC anode catalysts exposed to a mixture of hydrogen with CO in the 100 ppm range of concentration.

Figure 1 shows the set of anode polarization curves (j_{fh} vs. η) for the system parameter values in Table I. Figure 1 shows clearly the characteristic feature recorded for the electrochemical system Pt/H_2+CO. The current at low anodic overpotentials can be enhanced by increasing η only up to a certain limiting value (about 0.2 A/cm^2 at 50 ppm CO). To raise the hydrogen oxidation current beyond that limiting value, a much larger increase of anode overpotential is required. This limiting current is the result of control of the overall rate of hydrogen electro-oxidation at the Pt catalyst by the limited rate of the

TABLE I. Base Case Parameters

Parameter	Value	Unit
b_{fc}	$2\ 10^{-5}$	atm
b_{fh}	0.5	atm
k_{fc}	.06	A/cm^2-atm
k_{fh}	4.	A/cm^2-atm
b_h	.06	V/e-fold
b_c	.06	V/e-fold
k_{ec}	$2x10^{-9}$	A/cm^2
k_{eh}	2.0	A/cm^2
P_h	2	atm

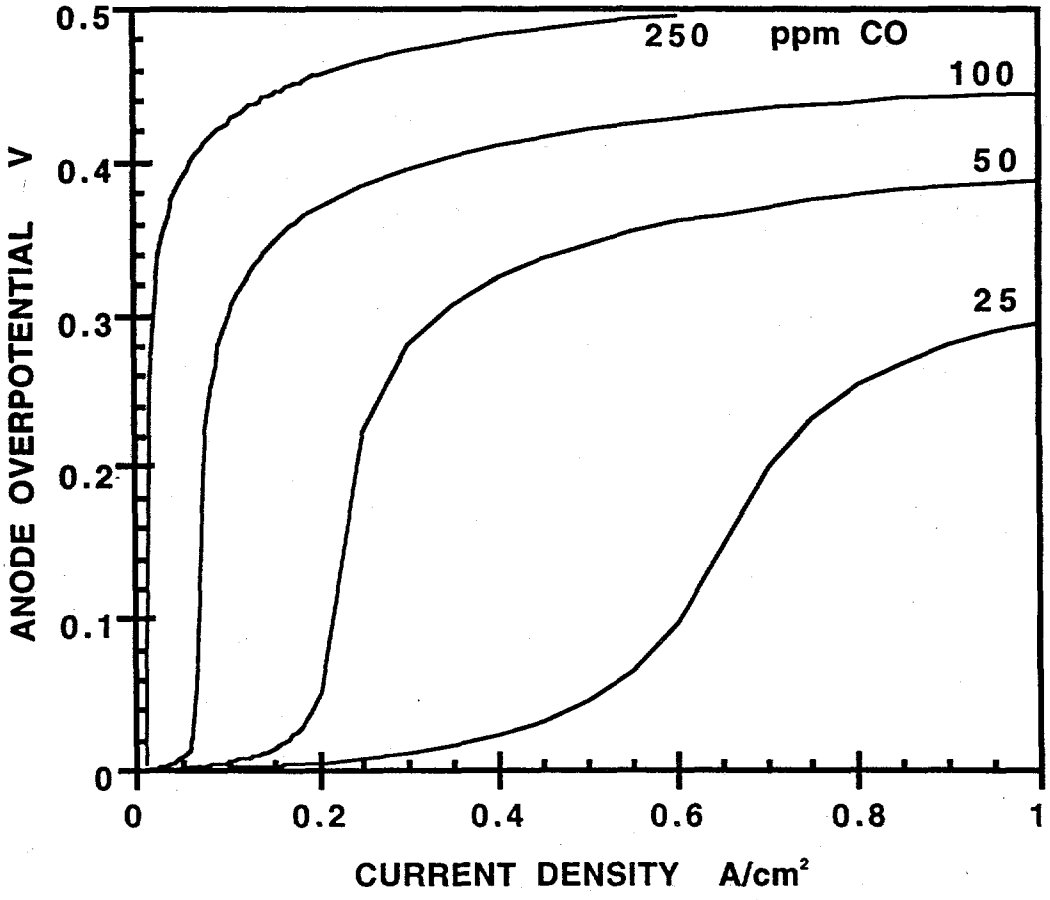

Figure 1: Anode overpotential as function of current density for base case parameters in Table I for different CO concentrations in the anode feed stream.

chemical process of dissociative chemisorption of hydrogen (Eq. 2) occurring on a limited number of CO-free Pt surface sites. When the rate of CO electrooxidation k_{ec} =0, this limiting current density, j_{hl}, is given by:

$$j_{hl} = k_{fh} P_h (1 - \theta_{co})^2 = k_{fh} P_h \left(\frac{b_{fc}}{b_{fc} + P_{co}} \right)^2 . \qquad [10]$$

It represents a limit, at given P_{CO} and cell temperature, on the current density that can be generated by the anode with minimal voltage losses. The finding that a limiting current density of hydrogen oxidation could arise at low anode overpotentials in the presence of CO was described in the 1975 work by Vogel, et al [7] for phosphoric acid fuel cell anodes, in which case the temperature of the fuel cell is significantly higher (190°C) and the relevant CO concentrations are much higher (about 1%).

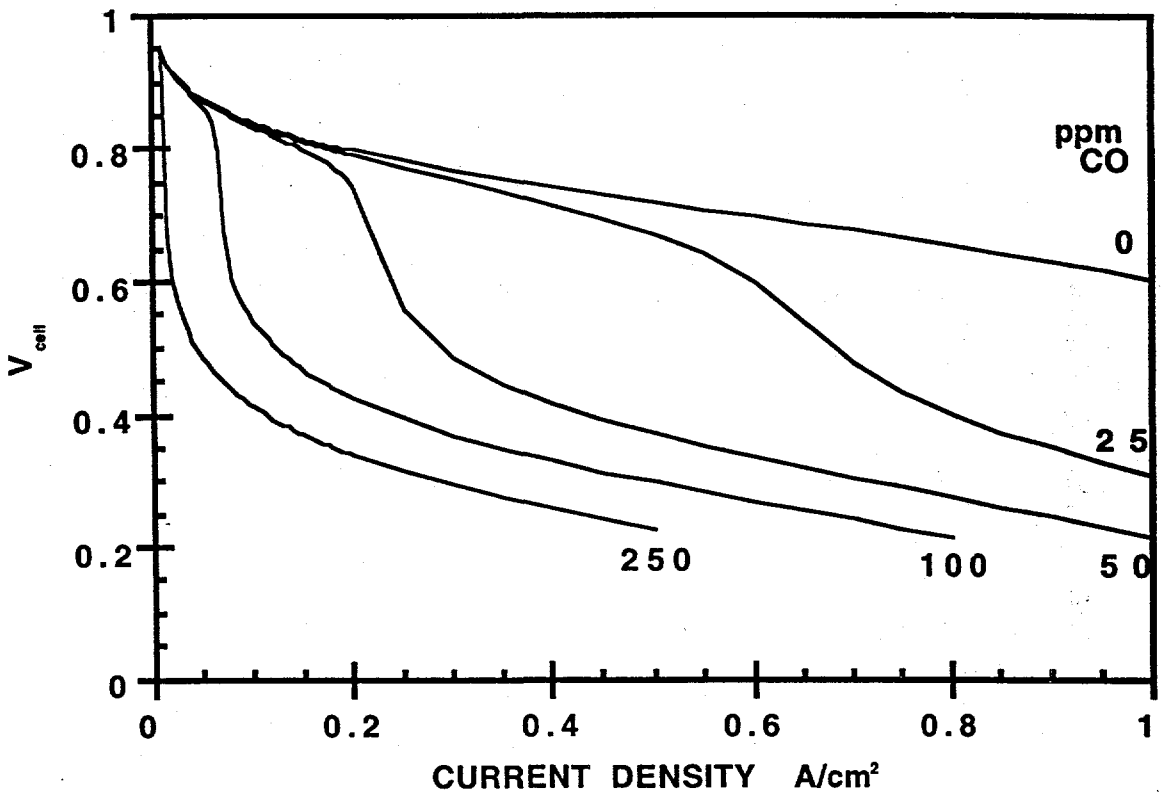

Figure 2: Cell polarization curve for base case parameters in Table I for different CO concentrations in anode feed stream.

For the purpose of comparison to the more common presentation of data in the literature, Fig. 2 shows calculated cell (PEFC) polarization curves for the same set of conditions as in Fig. 1. These polarization curves were obtained by subtracting excess anode polarization caused by some given level of CO at some current density from the typical voltage of a H_2/air PEFC at the same current density. This assumes negligible anode overpotential with pure hydrogen well saturated with water vapor. The calculated

polarization curves thus obtained are seen to exhibit several of the characteristic features of PEFC curves experimentally obtained for either Pt or PtRu-based anodes in the presence of CO in the anode feed stream. A typical experimental polarization curve is shown in FIg. 3, which is qualitatively very similar to the modeled Fig. 2. In each case shown in Fig. 1 and 2, there is a region of low current density for which little loss is observed as a result of addition of CO, followed by a much steeper decline in cell voltage and eventually leveling off at an almost constant level of cell voltage loss. The region of little polarization loss at low current densities is dependent on CO concentration, with higher current densities achievable at minimal voltage loss the lower the level of CO. As explained above, the current obtained in the low polarization region is apparently generated by hydrogen oxidation at a small fraction of uncovered (by CO) catalyst sites. The availability of such uncovered sites is related primarily to the equilibrium coverage of the catalyst by CO at the relevant temperature (i.e., by P_{co} and b_{fc}) and by any marginal catalytic activity of CO electro-oxidation at low anode overpotentials (i.e., by k_{ec}) . To quantify the possible effects of such factors, we examine below calculated variations in the polarization curve brought about by variations in these key model parameters.

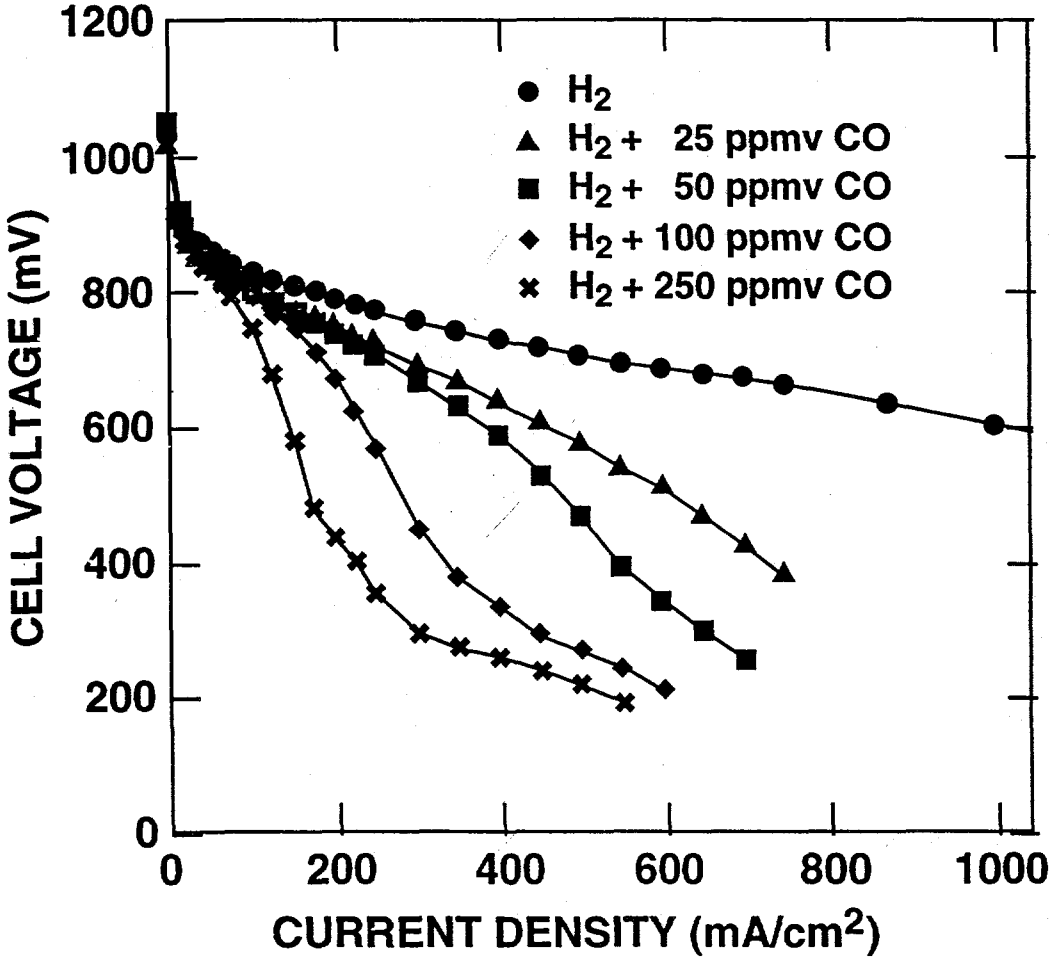

Figure 3: Measured IR corrected cell voltage on Pt anode with H_2/O_2 fuel cell with various concentrations of CO.

Anode Gas Pressure Effects

Lowering anode pressure should improve performance with CO when P_{co} is much greater than b_{fc}. Equation 10, which gives the limiting hydrogen current when k_{ec} =0, can be expressed in terms of total pressure and mole fractions of H_2 and CO.

$$j_{hl} = k_{fh} P_h \left(\frac{b_{fc}}{b_{fc} + P_{co}} \right)^2 = k_{fh} P_t x_h \left(\frac{b_{fc}}{b_{fc} + P_t x_{co}} \right)^2 \qquad [11]$$

If P_{co} is much larger than b_{fc} and $x_{co} << 1$, then if we fix x_{co}, the mole fraction of CO in H_2, we get

$$x_{co} \approx \frac{P_{co}}{P_t} \text{ and } j_{hl} \approx \frac{b_{fc}^2 k_{fh}}{P_t x_{co}^2}.$$

We see that when P_t, the total pressure is lowered, j_h will increase. Figure 4 demonstrates this with base case parameters, 100, 20, and 10 ppm CO, and pressures of 2, 1, 0.5 atm.

When x_{co} is dropped to 20 ppm, making P_{co} vary near the b_{fc} value of 2×10^{-5}, we see in the center plot of Fig. 4 crossover of the current density as η varies. When x_{co} is 10 ppm then the higher the pressure, the higher is the current density at a given overpotential. The model leads us to conclude that from an operational standpoint we should keep the anode pressure low if P_{co} is greater than b_{fc}. One may still want to keep the cathode pressure higher. Figure 5 shows this effect as measured by T. Rockward in MST-11.

Effect of Dilution

Now consider what happens if we dilute the feed stream with an inert gas. For experimental purposes, helium might be used to minimize transport diffusion losses. Let x_{dil} be the mole fraction of the diluent, x_h^o and x_{co}^o be mole fractions before dilution, and let $R = P_t x_{co}^o / b_{fc} = P_{co} / b_{fc}$ be the ratio of the undiluted partial pressure of CO to the CO adsorption rate. Then Eq. 10 or Eq. 11 can be expressed as

$$j_{kl} = \frac{k_{fh} P_t (1 - x_{dil}) x_h^o}{\left(1 + (1 - x_{dil}) R\right)^2}; \quad \frac{j_{kl}}{k_{fh} P_t (1 - x_{dil}) x_h^o} = \frac{j_{kl}}{j_{kl\,\text{no CO}}} = \frac{1}{\left(1 + (1 - x_{dil}) R\right)^2}. \qquad [12]$$

Keep in mind that Eq. 10 through 12 are to be applied at an overpotential small enough that CO electrooxidation is negligible, but large enough to obtain a measureable current. The term $k_{fh} P_t (1 - x_{dil}) x_h^o$ is the current density that would be obtained if no CO were present. Figure 6 plots as a function of dilution x_{dil} the ratio of j_{hl} to the limiting current density without CO for R values of 2 and 4. We can see that with x_{dil}=0, the limiting current ratio is $1/(1+R)^2$, rising to a maximum of 1/(4R) when x_{dil}=1-1/R, then rapidly dropping to zero as x_{dil} approaches 1.

This suggests a reasonable way to measure b_{fc} by diluting with helium a fixed CO/H_2 mixture. The use of He should minimize gas diffusion backing losses. By determining x_{dil} at the maximum current density, we should be able to determine b_{fc}. We will see in Fig. 7 in the next section on electrostripping that experimentally we can estimate j_{hl} by picking an anode overpotential slightly over 100 mV where the adsorption limiting current is reached but the onset of additional current from CO

electrostripping has not started. We should fix the anode overpotential for the various measurements

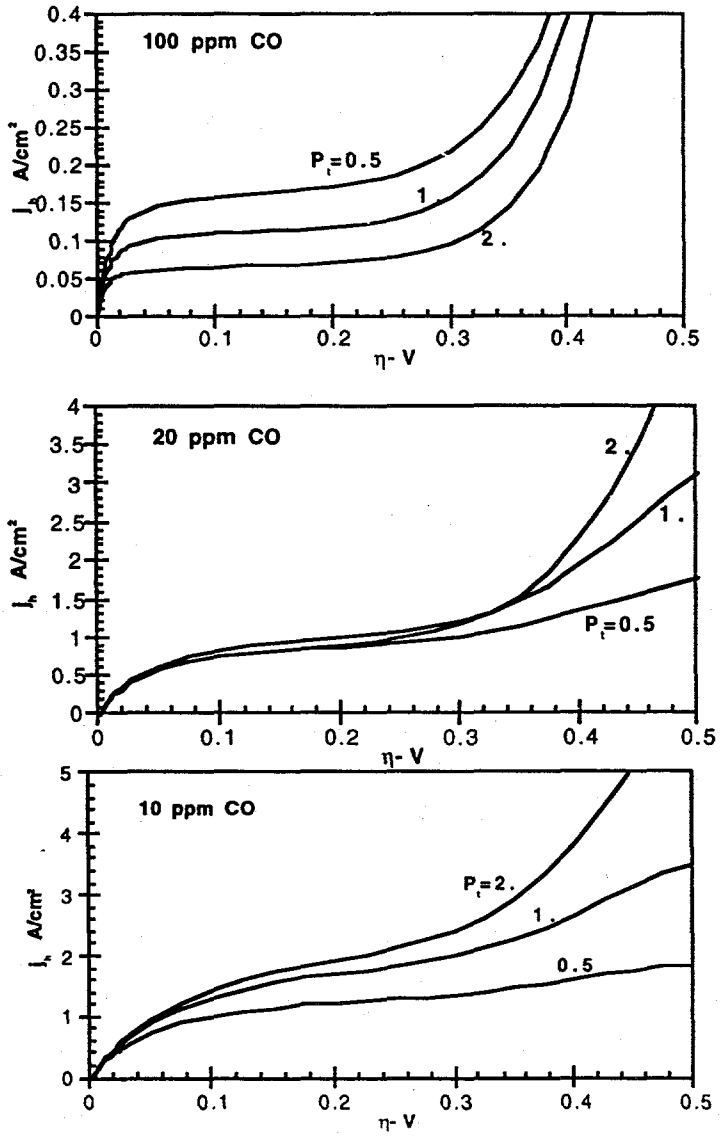

Fig. 4. Effect of total pressure on hydrogen current density using Table I parameters. When P_{co} is greater (top curves) than b_{fc} ($2x10^{-5}$atm) current density is greater at low pressure. Reverse is true when P_{co} is lower than b_{fc}.

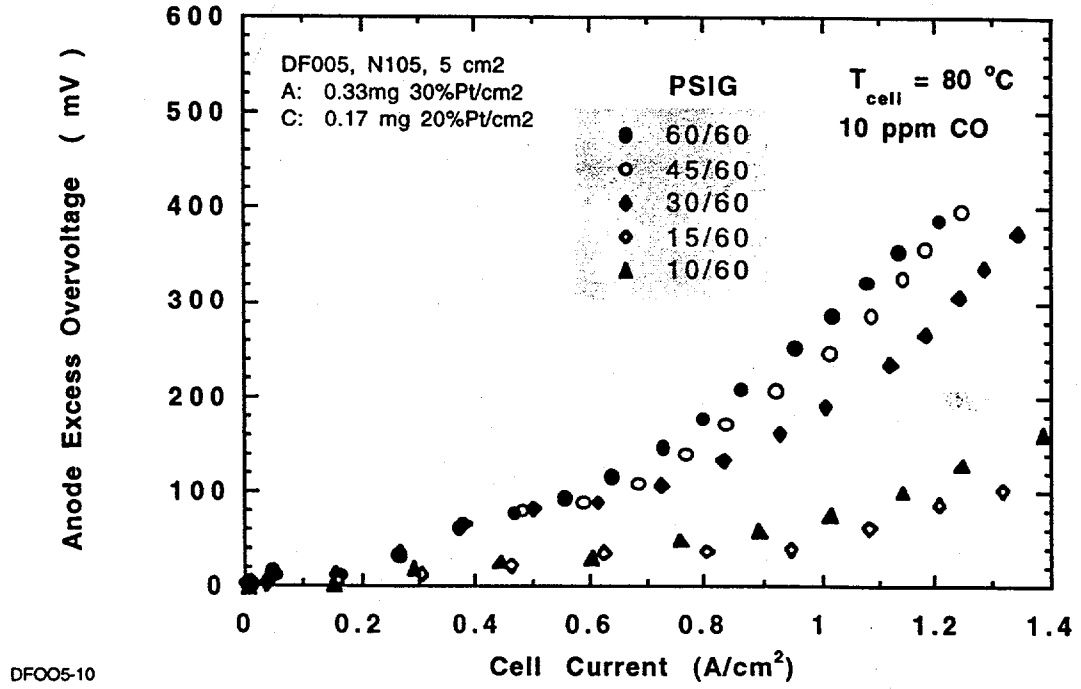

Fig. 5. Overpotential on Pt anode with 10 ppm CO at 5 anode pressures.

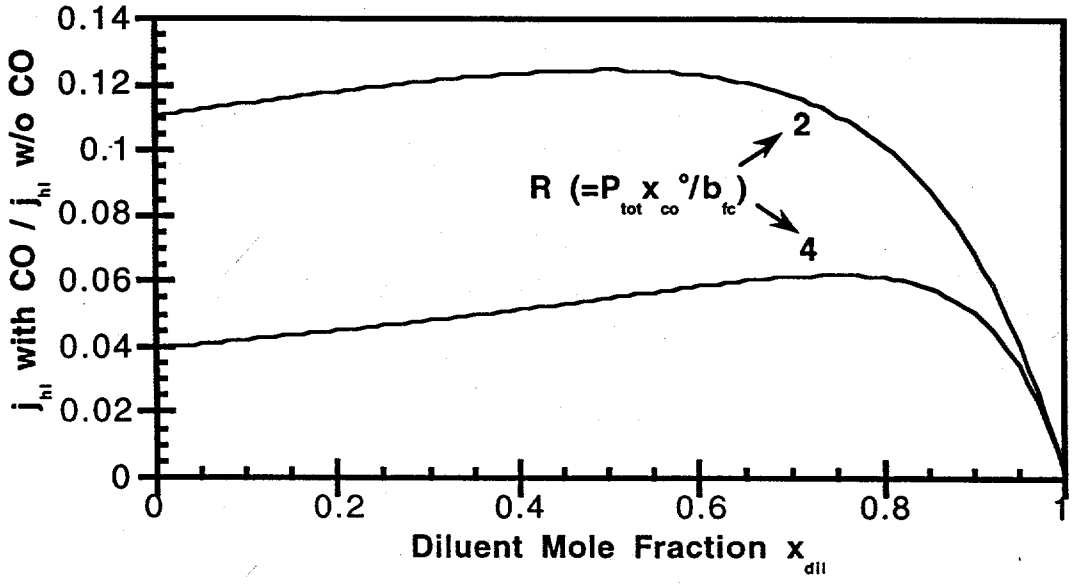

Fig. 6. By plotting the ratio of J_{hl} using a fixed ppm CO concentration befor He dilution to that of J_{hl} for pure H_2 before dilution as a function of He mole fraction x_{dil}, the model predicts that the value of x_{dil} at the peak can be used to determine b_{fc}.

needed to obtain a plot like Fig. 6. CO coverage might be determined more accurately by adsorbing CO in hydrogen at a known concentration, then flushing with nitrogen to remove the hydrogen, then electrochemically sweeping the anode voltage and recording the charge transferred by CO oxidation. However, the question remains whether the equilibrium CO level has shifted and whether adsorbed hydrogen remains that can be identified during the voltage sweep. The dilution experiment would at least have steady, equilibrium gas concentrations during the current measurements.

Effect of CO electrostripping

Figure 7 shows the effect of k_{ec} on determining the anode overpotential loss at high current density. We see that CO electrostripping does not effect the extremely low current region. We obtained the limiting current density j_{hl} of Eq. 10 by evaluating Eq. 8 when k_{ec} was 0 and η was large, which indicates the location of the steep inflections in Fig. 1 and which is indeed a limiting current if k_{ec} were really zero as we show in Fig. 7 and 8. Figure 8 shows the effect on the current without CO electrostripping of various CO concentrations. Note that Eq. 10 goes to the forward dissociative adsorption current density for hydrogen in the case where P_{co} is 0, as one would expect. It only gets small when P_{co} becomes much larger than the CO desorption-adsorption rate ratio b_{fc}.

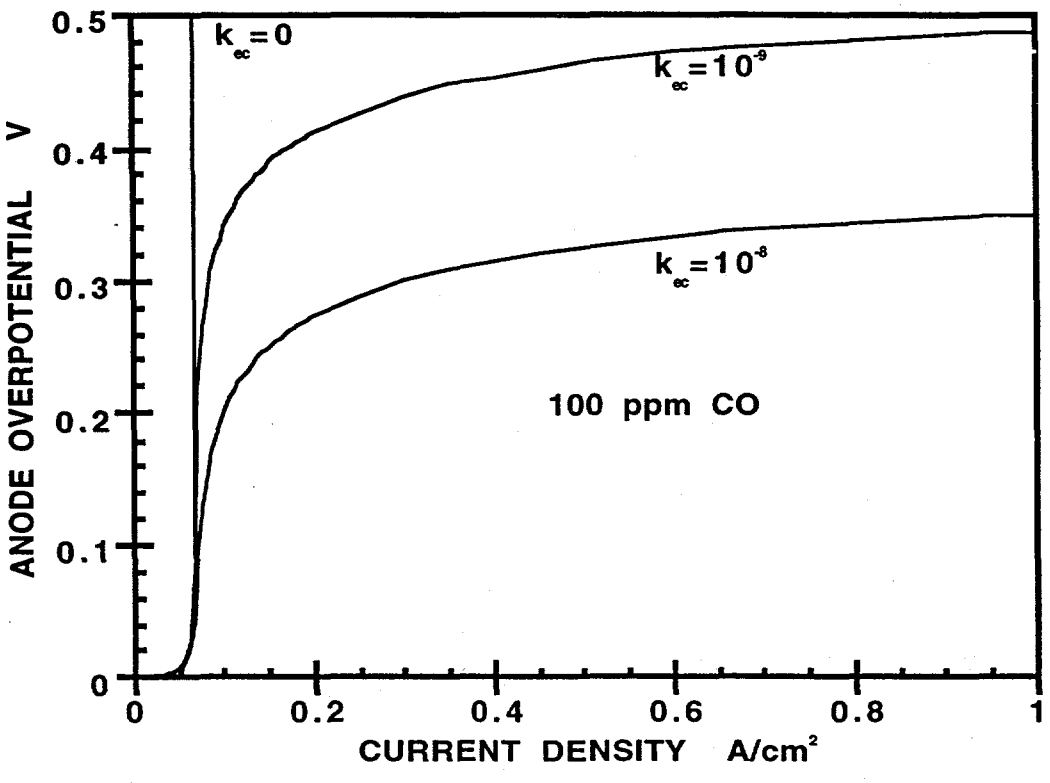

Fig. 7. Anode polarization for k_{ec} =0, 10^{-9}, and 10^{-8}, base case otherwise for 100 ppm CO illustrating the limiting current of Eq. 10 and effect of k_{ec} on high current CO losses.

ANODE OVERPOTENTIAL V

Calculated Effects of Variations in Equilibrium Coverage of CO

To develop further insight into the factors allowing effective hydrogen oxidation in the presence of CO, we proceed to explore effects of other variations in base case parameters. Figure 9 shows the effect of varying b_{fc}, the (inverse of) the equilibrium constant for CO adsorption. Figure 9 has three parts. The upper part shows the rate of CO electro-oxidation as function of applied potential as k_{ec} is kept at the base case level of 10^{-9} A/cm^2 at 0V RHE. Under such conditions, the rate of CO stripping is sub μA/cm^2(geom.) in the potential domain of interest (< 0.2V) , and the effect on steady-state CO coverage in the potential domain of interest is negligible, as can be seen from the middle part of Fig. 6. This middle part shows the variation of CO coverage as a function of anode potential for two cases of b_{fc} , the base case (b_{fc} = 2x10^{-5}atm) and a case of a ten times smaller inverse equilibrium constant (b_{fc} = 2x10^{-6}atm). Lowering affinity of CO to the catalyst surface to that extent is seen to lower the equilibrium CO coverage in the most relevant potential domain (around 0.1V) from 97% to 90%. This has a very substantial effect on the hydrogen oxidation current in this potential domain, as can be expected from the approximate dependence of the hydrogen oxidation current on

Fig. 8. Anode polarization for k_{ec}=0. for 3 CO concentrations, showing effect of P_{co} in Eq. 10.

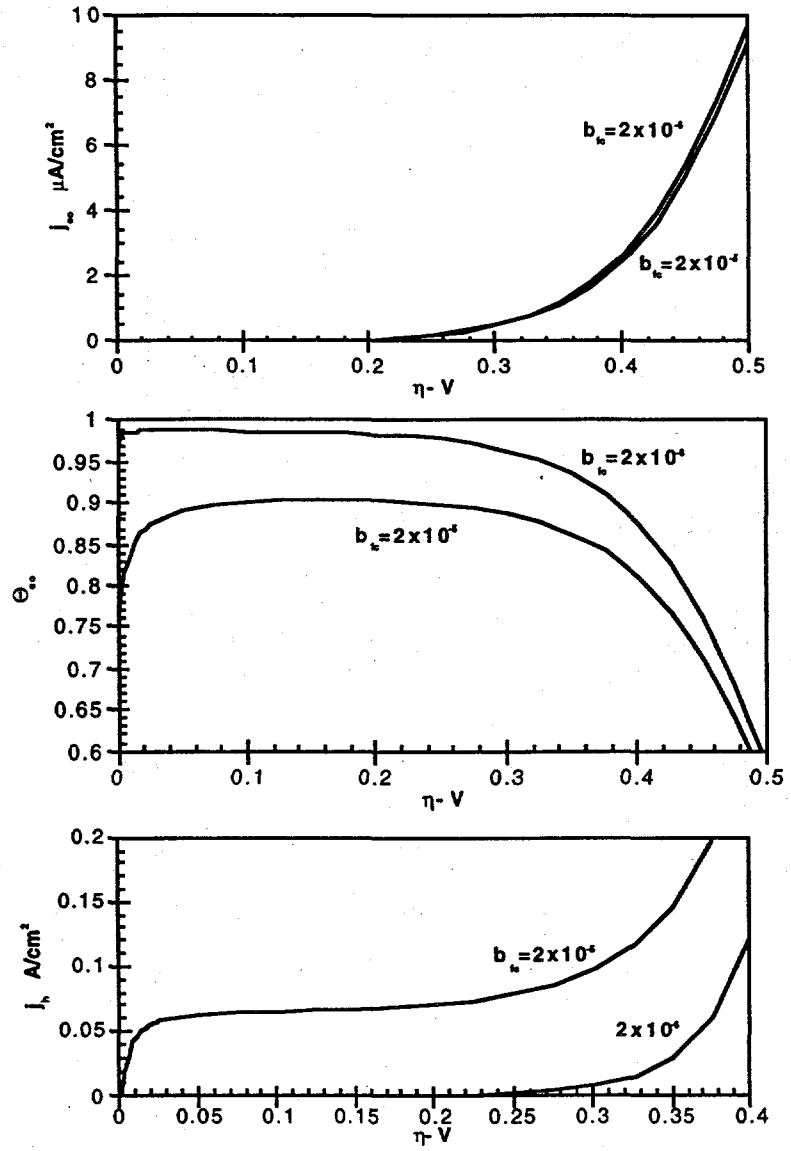

Fig. 9: Effect of change by factor 10 in b_{fc} (inverse equilibrium constant for CO adsorption on CO surface coverage (middle part) and, consequently, on hydrogen electro-oxidation current (lower part). CO concentration is 100 ppm. Other model parameters have values as in Table I. (Upper part shows CO electro-oxidation current corresponding to the very low electrocatalytic activity assumed -- see Table I). The abscissa in all plots shows anode overpotential vs. RHE.

$(1-\theta_{co})^2$, discussed above, and this beneficial effect is clearly seen in the lower part of Fig. 9.

Such a change in b_{fc} could thus assist effectively in increasing the anodic current density achievable with small voltage loss from a PEFC operating on H_2 with, e.g., 100 ppm CO. To achieve such a change in b_{fc} experimentally, what would be required is to

either raise the temperature of the PEFC with a given Pt, or Pt alloy catalyst, or, alternatively, develop novel anode catalysts with active sites (most probably Pt sites) of lower affinity to CO at 80°C, achieved thanks to various possible effects of alloying. In the latter type of effort, the diagnostic criterion for success should be enhancement of hydrogen electro-oxidation currents at the alloy catalyst around 0.1V vs. RHE (see lower part of Fig. 9.

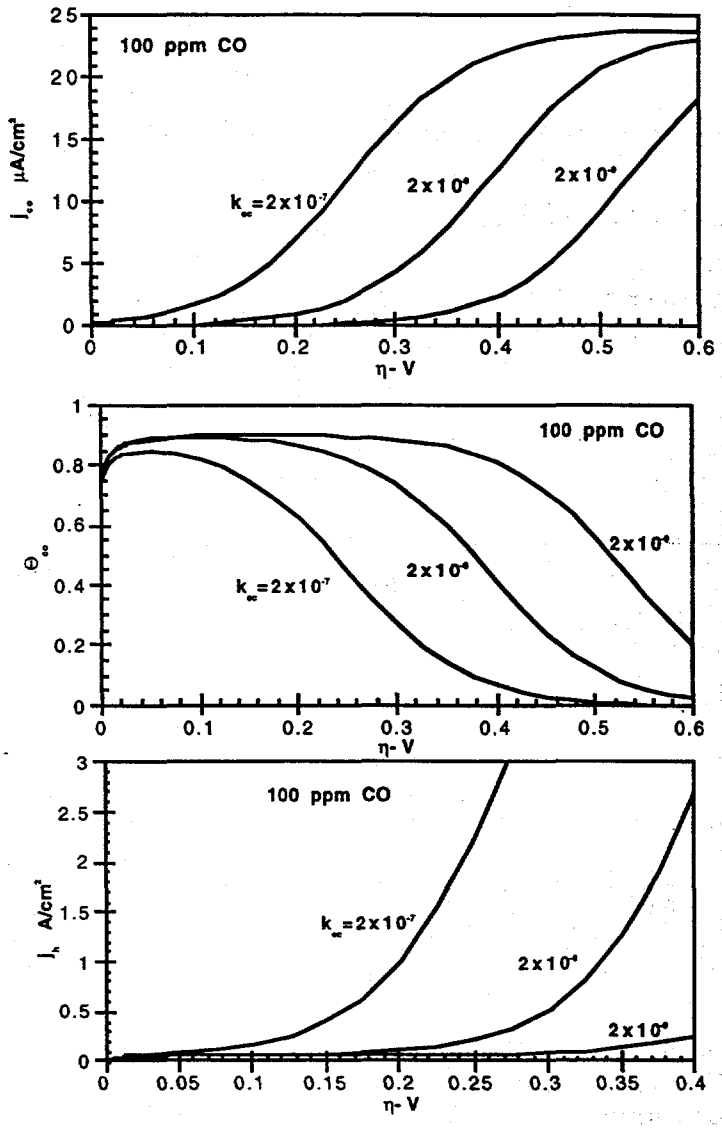

Fig. 10. Effect of increase by factor 10, or 100, in rate constant for CO electro-oxidation on: CO electrooxidation current (upper part), CO surface coverage (middle part) and hydrogen electro-oxidation current (lower part).Other model parameters have values as in Table I. The abscissa in all plots shows anode overpotential vs. RHE.

Calculated Effects of Marginal Rates of Electrochemical Stripping of CO at Low Anodic Potentials

Figure 10 shows calculated effects for the case of 100 ppm CO in H_2, of raising the rate constant for electrochemical stripping of CO, k_{ec}, (process described by Eq. 4) by one or two orders of magnitude above the very low level of $2x10^{-9}$ A/cm^2 (geom.) at 0V, assumed in the base case. The top part of Fig. 10 shows calculated CO stripping currents, the middle part shows the corresponding CO coverage as function of anode potential and the bottom part of Fig. 10 shows the resulting hydrogen oxidation currents as function of anode potential. Other parameters are kept as in the base case (see Table I). It is evident from these curves that quite low CO stripping current densities, on the order of a few μA/cm^2 (geom.) (i.e., nA/cm^2 Pt), can translate into quite significant effects on steady state CO coverage in the relevant anode potential range and, consequently, into significant hydrogen oxidation current densities. For example, for the case of $k_{ec} = 2 \times 10^{-7}$, j_{co} at an anode potential of 0.2V is just about 6 μA/cm^2 (geom.), but this results in a lowering in CO steady state coverage sufficient to enable a hydrogen oxidation current density of 1 A/cm^2 at the same anode potential. The strong effect of what is still a very low CO electro-oxidation rate, is a consequence of the high rate of the hydrogen electro-oxidation process per catalyst site available. Note, however, that there is still a substantial penalty in terms of voltage loss to be paid at this current density -- at least 0.15V in excess over the anode loss at 1A/cm^2 with pure H_2.

POSSIBLE DIFFUSION EFFECTS IN CATALYST LAYER

Previously we have examined what happens on the surface of a catalyst when the CO partial pressure is fixed at the gas/catalyst interface. Now we examine the possible use of diffusion effects to improve anode performance in the presence of CO. As we have seen in the oxygen cathode catalyst layer[8], the effective diffusion coefficient is approximately 100 times higher than what would be expected for diffusion through pure nafion or similar ionomer. The mean free path for H_2 at 1 atm is around 235 Å, which is approximately the carbon particle size used in the catalyst layer ink. Whereas in the gas diffusion backing layer we expect the probability of a hydrogen molecule colliding with other gas molecules to be high relative to colliding with fixed surfaces, in the catalyst layer we cannot say that this is true. Rather than use Stefan- Maxwell equations in which one gas species diffuses through another, we will assume each species diffuses independently through the layer.

Let C^o_{co} be the concentration of CO in the catalyst layer in equilibrium with 1 atm CO gas. Similarly let C^o_h be the concentration of H_2 in equilibrium with 1 atm H_2. We assume the actual concentration in the catalyst layer of each species at a gas interface is proportional to the partial pressure of the species in the gas at the interface. We do not speculate on the physical form of the species in the catalyst layer, i.e. dissolved in ionomer, adsorbed on graphite surfaces, etc. We let D_{co} and D_h be the effective diffusion coefficients for H_2 and CO in the catalyst layer. The local concentration of species i is $C_i = C^o_i P_t x_i$ where x_i is the mole fraction of the species in an equilibrium gas phase and P_t is the ratio of the total external pressure to 1 atm pressure. With these definitions the flux f_i of the i^{th} species using Fick's law in the catalyst layer is

$$f_i = -D_i \frac{\partial C_i}{\partial z} = -D_i C^o_i P_t \frac{\partial x_i}{\partial z} \qquad [13]$$

where i can be co or h . Let $y=z/L$ be the fractional distance through the catalyst layer of thickness L.. The rate constants have been selected for the thickness L. Applying the steady state continuity equation we get :

$$-\nabla \cdot f_i = \frac{j_i(\eta, x_h, x_{co})}{n_i FL} = \frac{D_i C_i^o P_t}{L^2} \frac{\partial^2 x_i}{\partial y^2}$$

$$\frac{\partial^2 x_i}{\partial y^2} = \frac{j_i(\eta, x_h, x_{co})}{P_t I_{Di}}; \left.\frac{\partial x_i}{\partial y}\right|_{y=1} = 0 \; ; \; x_i|_{y=0} = x_i^o \qquad [14]$$

$$\text{where } I_{Di} = \frac{n_i F D_i C_i^o}{L}.$$

The characteristic diffusion current density, I_{Di} is the fictitious current density per atm that would be obtained from one atm of species i on the gas side of a catalyst layer of thickness L being completely electro-converted at the membrane/catalyst layer interface rather than within the catalyst layer. I_{Di} is intended to be a measure of the diffusion coefficient for species i in a catalyst layer, and not a function of the actual thickness or partial pressure. We would expect the characteristic diffusion current density for hydrogen and CO to be approximately related by the square root of the molecular weight ratio times the Henry constant ratio. While the Henry constant values for CO and H_2 dissolved in water were taken at 20°C [9], the ratio should be similar at other temperatures.

$$\frac{I_{Dco}}{I_{Dh}} = \sqrt{\frac{M_h}{M_{co}}} \frac{C_{co}^o}{C_h^o} \approx \sqrt{\frac{2.016}{28.01}} \bullet \frac{6.83 \bullet 10^4}{4.9 \bullet 10^4} \approx 0.2673 \qquad [15]$$

We reasonably expect I_{Dh} to have a value of at least 2 A/cm^2-atm, which would from Eq. 15 make I_{Dco} = 0.534. A/cm^2-atm. With these values of I_{Di} we find negligible performance improvement because, if the catalyst layer can transport hydrogen well enough to allow the observed high current densities observed, it can also transport CO sufficiently well to poison the catalyst. By artificially decreasing the CO diffusion coefficient by a factor R we can magnify the effect to see if improvement is possible if such selective diffusion reduction of CO could be attained. In Fig. 11 we have calculated as a function of anode overpotential using Table I parameters at 50 ppm CO the effective mole fraction of H_2 and CO at the membrane/catalyst layer interface for I_{Dh} = 2 A/cm^2-atm for R=1., .01, and .001 and the resulting total current density. We can see that it would be necessary to decrease the CO transport by several orders of magnitude to obtain improvement by diffusion.

A more achievable use of diffusion is to lower I_{Dh} to 0.2 and .02 and correspondingly I_{Dco} keeping R=1. In Fig. 12 we see that for lower (and usable) overpotentials, the hydrogen concentration drops, but the CO does not, resulting in poorer performance when I_D is decreased. We conclude that CO diffusion loss in the catalyst layer is not a realistic process for improving anode performance.

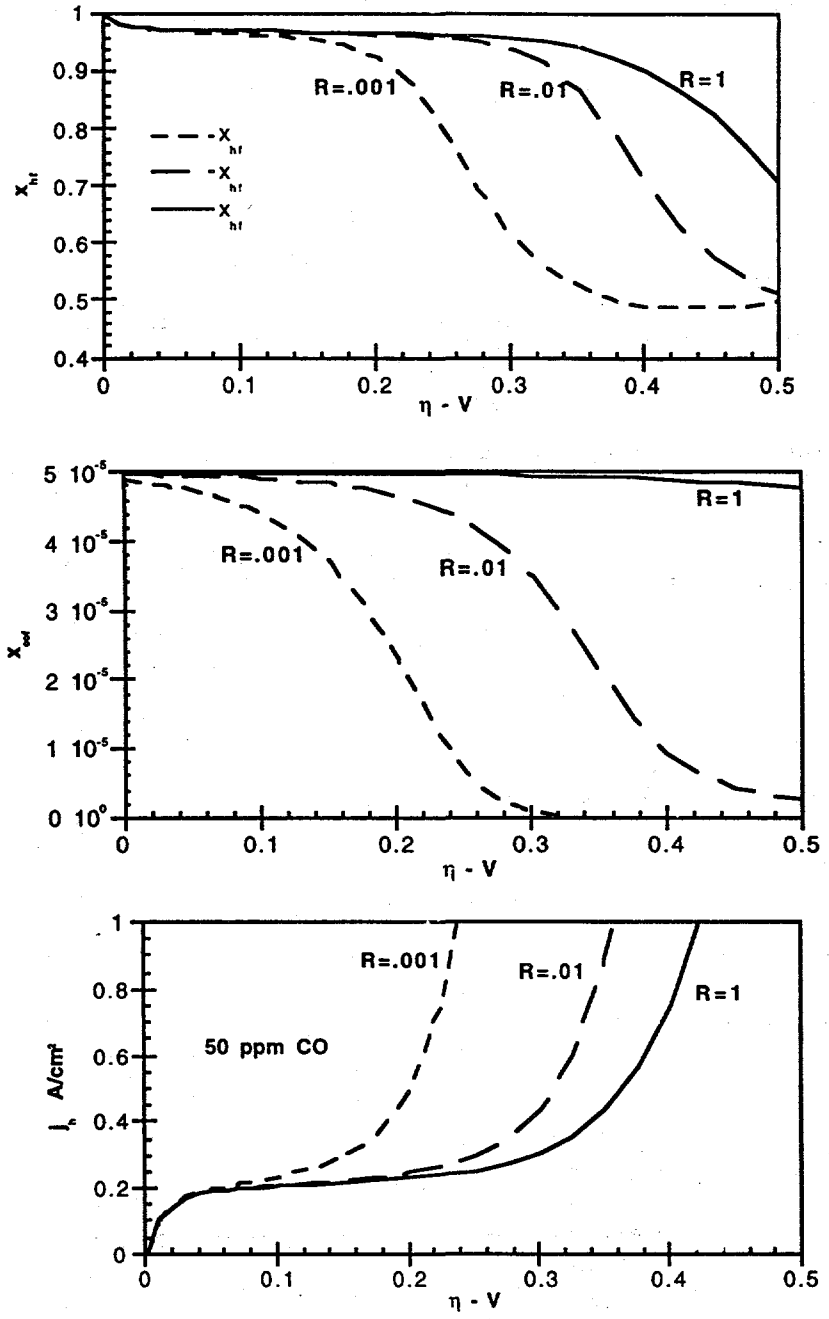

Fig. 11. Top and middle plots show as a function of η the equivalent mole fraction of hydrogen and CO at membrane/catalyst layer interface for I_{Dh} = 2 A/cm^2. The solid curve (R=1) uses expected corresponding CO diffusion coefficient, the other two reduce the CO diffusion coefficient proportional to R. The bottom plot shows the corresponding current density. We use the base case conditions of Table I with 50 ppm CO.

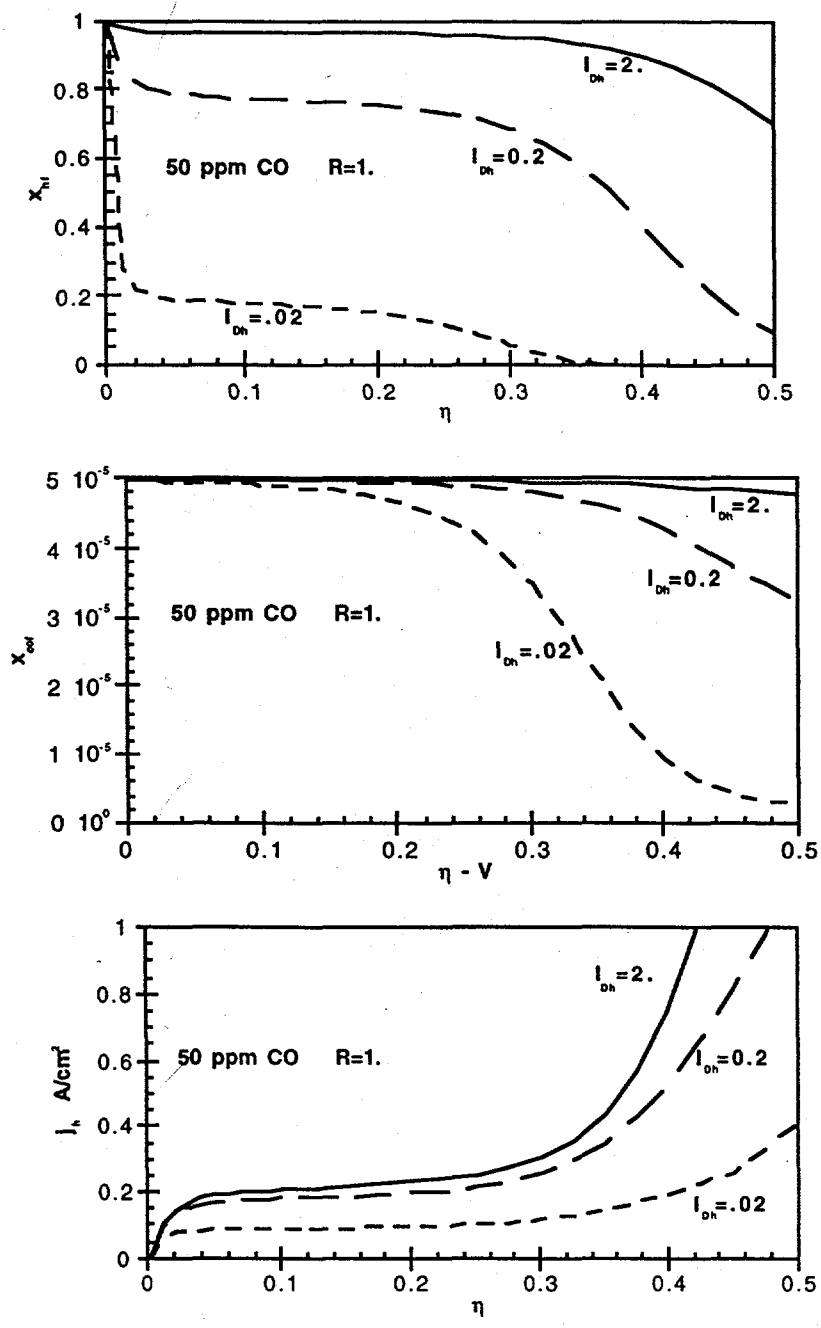

Fig. 12. Same plots as Fig. 11 except R=1 and I_{Dh} =2., 0.2 and .02 A/cm^2-atm.

GAS DIFFUSION BACKING MODEL

Equations

Multicomponent diffusion through a porous medium of porosity ε and tortuosity τ is described by the Stefan-Maxwell equations. Given a set of fluxes N_i (mol/cm^2-s), the gradient of the mole fractions x_i of the various gas components is:

$$\frac{dx_i}{dz} = \frac{\mathcal{V}_m(T_k / T_s)}{(\varepsilon / \tau)} \sum_{j \neq i=1}^{n} \frac{x_i N_j - x_j N_i}{P_{tot} \mathcal{D}_{ij}}. \qquad [16]$$

Here $\mathcal{V}_m$ is the standard molar volume, T_s is 273K, T_k is the temperature in K and P_t is the total pressure. The binary diffusion coefficients (cm^2/s) times pressure (atm) are given by the Fuller, Schettler, Giddings relation[8]: (

$$P_t \mathcal{D}_{ij} = \frac{10^{-3} T_k^{1.75} \sqrt{1/M_i + 1/M_j}}{\left(\sqrt[3]{\Sigma v_i} + \sqrt[3]{\Sigma v_j}\right)^2} \qquad [17]$$

where M_i is the molecular weight and $(\Sigma v)_i$ is the atomic diffusion volume.of the i^{th}

Table II

INDEX	SPECIES	M_I	Σv
1	H_2	2.0158	7.07
2	CO	28.01	18.9
3	N_2	28.0134	17.9
4	CO_2	44.01	26.9
5	H_2O vapor	18.0153	12.7

We are given the feed stream mole fractions entering the gas diffusion backing. The fluxes of H_2 and CO are determined by the electrode potential and the kinetic equations. The fluxes of N_2 and CO_2 are assumed to be zero. We need to determine the gas mole fractions at the catalyst layer side of the backing with thickness ℓ. We combine all the known constants from above into a matrix α where $\alpha_{ij} = \frac{\mathcal{V}_m(T_k / T_s)}{(\varepsilon / \tau) P_{tot} \mathcal{D}_{ij}}$. While there are 5 components, we actually have only 4 equations and 4 unknowns to determine the exit $x_i(\ell)$. Because of the saturation condition on the 5th component, water, the 5th equation is $dx_5 / dz = 0 = x_w(\alpha_{1w}N_1 + \alpha_{2w}N_2) - N_w(\alpha_{1w}x_1 + \alpha_{2w}x_2 + \alpha_{3w}x_3 + \alpha_{4w}x_4)$, from which we can solve for the water flux, N_w. We now use the subscript w instead of 5, since we have eliminated the 5th equation. Unlike the other two fluxes, N_w is not exactly constant because the mole fractions vary across the backing and the resulting equations are not linear. However, if we assign N_w its value N_w^o at the entrance conditions, determine the exit conditions and reevaluate N_w at the exit conditions, we find it has changed less than a percent. Thus we will use N_w^o and have a set of 4 first order differential equations with constant coefficients to solve. Letting

$$x_i' = \frac{dx_i}{dz} \text{ and } N_j^\circ = \frac{x_w(\alpha_{1w}N_1 + \alpha_{2w}N_2)}{(\alpha_{1w}x_1^o + \alpha_{2w}x_2^o + \alpha_{3w}x_3^o + \alpha_{4w}x_4^o)}$$

we have the following set of linear first order equations to solve to obtain the mole fractions at the catalyst layer/backing interface. We assume the hydrogen and CO fluxes, N_1 and N_2 are equated to the kinetic current density fluxes $j_h/2F$ and $j_{co}/2F$ respectively.

$$\begin{bmatrix} x_1' \\ x_2' \\ x_3' \\ x_4' \end{bmatrix} = \begin{bmatrix} \alpha_{12}N_2 + \alpha_{1w}N_w^o & -N_1\alpha_{12} & -N_1\alpha_{13} & -N_1\alpha_{14} \\ -N_2\alpha_{12} & \alpha_{12}N_1 + \alpha_{2w}N_w^o & -N_2\alpha_{23} & -N_2\alpha_{24} \\ 0 & 0 & \alpha_{13}N_1 + \alpha_{23}N_2 + \alpha_{3w}N_w^o & 0 \\ 0 & 0 & 0 & \alpha_{14}N_1 + \alpha_{24}N_2 + \alpha_{4w}N_w^o \end{bmatrix}$$

$$\cdot \begin{bmatrix} x_1 \\ x_2 \\ x_3 \\ x_4 \end{bmatrix} - \begin{bmatrix} N_1\alpha_{1w}x_w \\ N_2\alpha_{2w}x_w \\ 0 \\ 0 \end{bmatrix} \qquad [18]$$

Analytic Solution of Linear First Order

Since we could not readily find a computer library routine to solve Eq. 18 analytically, we briefly describe briefly SUBROUTINE DVINT we wrote to integrate such equations. We have a set of linear first order equations of the form

$$\mathbf{x}'(z) = \mathbf{A}\mathbf{x}(z) + \mathbf{B}, \qquad [19]$$

where $\mathbf{x}(z)$ is the dependent variable vector, in our case the component mole fractions, $\mathbf{A}$ is a real, non symmetric, constant matrix that has an inverse, $\mathbf{B}$ is a known real, constant vector, z is the independent variable (position through gas diffusion backing, and $\mathbf{x_o}(0)$ are the known initial conditions. We used the routine DEVVUN from the Language Systems MATH77 library to solve for the eigenvalues λ_i and eigenvectors $\mathbf{T}$ of the matrix $\mathbf{A}$. We transform Eq. [19] to a new set of variables $\mathbf{y}$ such that

$$\mathbf{x} = \mathbf{T}\,\mathbf{y} \qquad [20]$$

Substituting Eq. 20 into Eq. 19 we get $\mathbf{T}\,\mathbf{y}' = \mathbf{A}\,\mathbf{T}\,\mathbf{y} + \mathbf{B}$ and multiplying by $\mathbf{T}^{-1}$, we get $\mathbf{y}' = \mathbf{T}^{-1}\mathbf{A}\,\mathbf{T}\,\mathbf{y} + \mathbf{T}^{-1}\mathbf{B} = \lambda\,\mathbf{I}\,\mathbf{y} + \mathbf{C}$; where $\mathbf{C} = \mathbf{T}^{-1}\mathbf{B}$ and $\mathbf{I}$ is the identity matrix. This will give us N (=4) separate equations

$$y_i' = \lambda_i y_i + c_i. \qquad [21]$$

The initial conditions are given by $\mathbf{y_o} = \mathbf{T}^{-1}\ \mathbf{x_o}$. The solution of Eq. 21, a set of decoupled, first order, linear differential equations is

$$y_i(z) = \left(y_i^o + \frac{c_i}{\lambda_i} \right) e^{\lambda_i z} - \frac{c_i}{\lambda_i}. \qquad [22]$$

Once the $y_i(z)$ are determined, we can determine $x_i(z)$ from Eq. 20.

Effect of Anode Backing on Gas Composition

We will assume the porosity and tortuosity of the anode backing are similar to what we have used for the cathode backing[10] and will use 0.4 and 8 respectively for ε and τ. Using a feed composition of 40% H_2, 35% N_2, and 25% CO_2, that expected for autothermal reforming on methanol, Fig. 13 shows the relative mole fraction change for CO from inlet composition as a function of backing thickness for combinations of two current density values each of hydrogen and CO. The inlet CO composition is 100 ppm before saturation with water vapor at 80°C and the pressure is 2 atm. We see for 3 of the 4 cases that CO increases mole fraction through the backing. Only for low hydrogen current and relatively high CO current does the backing lower CO concentration. Figure

14 shows the H_2, CO_2 and N_2 compositions through the backing at 1 A/cm^2 of hydrogen current. Only the CO composition is measurably affected by CO current.

Effect with CO of Anode Dilution and Backing on Cell Performance

We can now calculate the effect on anode CO losses caused by the dilution that would occur in a reformate feed stream and by gas diffusion in the anode backing. Figure 15 shows predicted cell voltage as a function of current density for water-vapor-saturated feed gas of pure hydrogen, a reformate mixture using external heating of 0.75/0.25 H_2/CO_2 proportions, and an autothermal reformate mixture of 0.4/0.35/0.25 $H_2/N_2/CO_2$ proportions. A reference curve for neat hydrogen without CO is also shown. If we look at the losses at 0.4 A/cm^2 by differencing the various curves we see in Table III that the greatest loss is from CO itself (239 mV), the next greatest loss is from dilution (28mV and 80 mV) and the lowest loss is from the backing (14 mV and 9 mV).

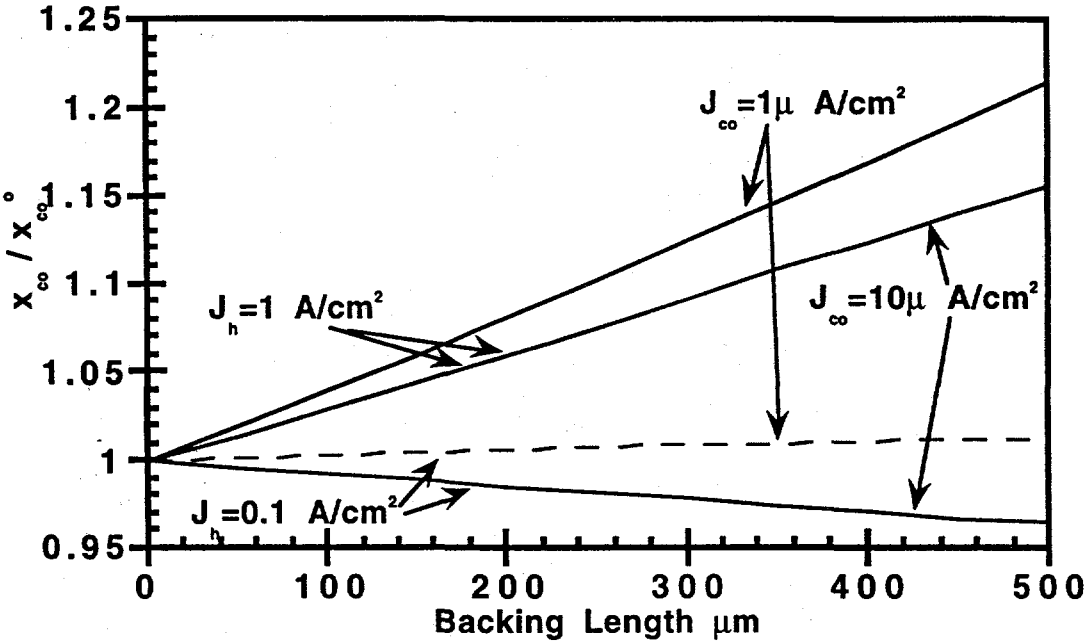

Fig. 13 Relative change in CO composition from inlet conditions for different hydrogen and CO current combinations as a function of backing thickness.

Table III. Losses at 0.4 A/cm^2 from 50 ppm CO, dilution, and backing per Fig. 13.

TYPE OF LOSS	mV
Loss from CO in pure H_2	239
Loss from dilution in .75/.25	28
Loss from dilution in .4/.35/.25	80
Loss from backing in H_2	14
Loss from backing in .75/.25	9
Loss from backing in .4/.35/.25	9

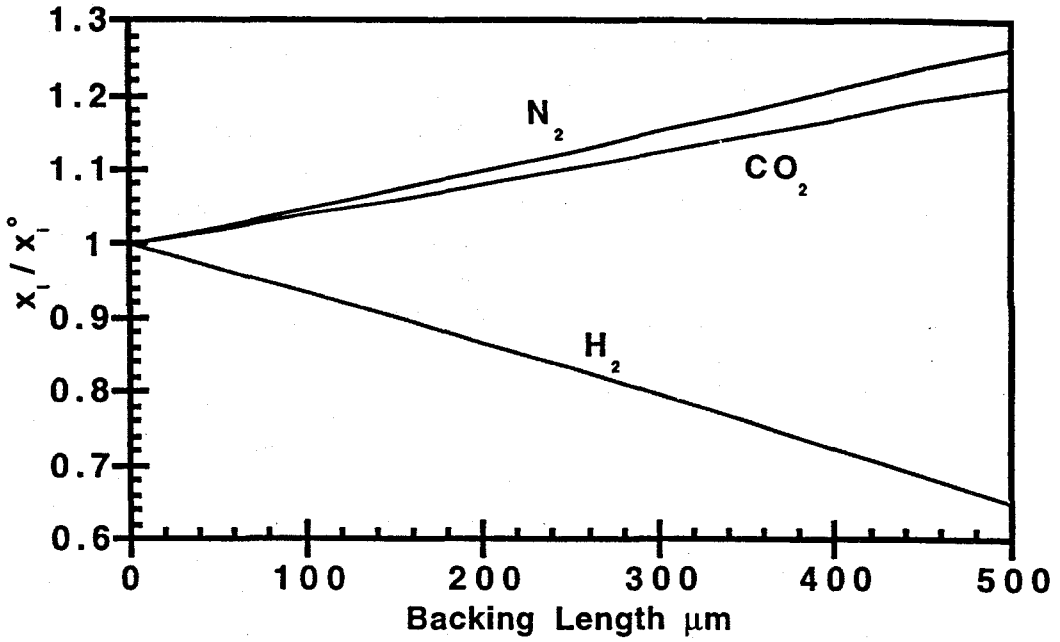

Fig. 14. Relative change in H_2, CO_2, and N_2 compositions for 1 A/cm^2 hydrogen current density as a function of backing thickness.

CARBON MONOXIDE TRANSIENT EFFECTS

Transient Time for CO Concentration Variations in Fuel Cell Stack

In order to understand transient effects of CO concentration, we need to determine the number of sites available in the anode for hydrogen or CO adsorption. Measurement in MST-11 by J. Bauman of CO poisoning on Pt/Ru finds the time T_f to reach a new equilibrium current density following either introduction or non-introduction of x_{CO}=100 ppm CO into an equivalent flow rate I_h=2 A/cm^2 of hydrogen to be about 142 s. If s_d is quantity of CO occupied per geometric electrode area, then we might expect, assuming complete access of all gas molecules to the catalyst layer, that

$$s_d = \frac{x_{co} T_f I_h}{2F}. \qquad [23]$$

For the above numbers this corresponds to 1.42 x 10^{-7} mol/cm^2 (geom). The anode catalyst loading for this experiment was 0.39 mg/cm^2. Using an average density of 16.93 gm/cm^3 and a catalyst particle size of about 25 Å, we find the catalyst surface area/geometric area to be 0.00039/16.93x3/25x10^{-8}=276.4 cm^2 PtRu/cm^2 geom . The number of occupied sites per PtRu surface is 1.42 x 10^{-7} x 6.02 x 10^{23} /276.4 = 3.09 x 10^{14} sites/cm^2 PtRu.. Experiments may be performed in which the fill time is measured for several hydrogen flows and various CO mole fractions. As the flow is increased, mass transport from the flow channels to the catalyst layer will eventually limit the actual fill time from that calculated for complete gas access.

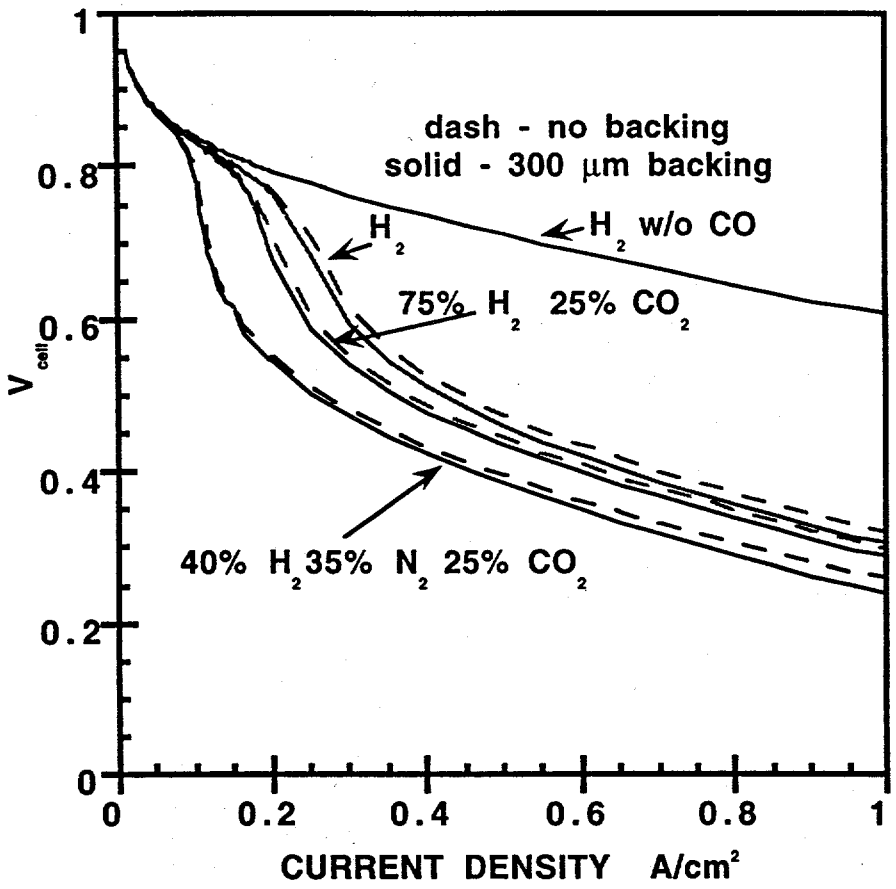

Fig. 15. Predicted cell polarization curves for typical air cathode comparing different water vapor saturated anode feed streams with and without anode backing losses for 50 ppm CO in all 3 anode gas compositions. Table I parameters are used.

Transient Switching of Cell Potential with the HP Electronic Loads

We briefly experimented with positive pulsing the anode voltage of a fuel cell containing 50 ppm CO in the anode gas. This was an attempt to strip the CO off the catalyst sites in a short time period with high overpotential and then obtain hydrogen current for a longer period of time at a low overpotential. Because of the high double layer capacitance, we were unable to apply 0.5 V to the anode in a short enough time and the average current and average overpotential were the same with the pulsed system as if a steady potential were applied. The method of applying the potential might have application for future experiments and is reported here.

For slow pulsing that can be done by manual switching, the circuit in Fig. 16 was used. With the toggle switch open a resistance less than 2000 Ω in series with the positive voltage sense line has no effect. When the switch is closed a positive voltage between 0 and 1.5 V is added to the sense voltage, depending on the potentiometer setting. This lowers the cathode voltage or raises the anode voltage relative to the

cathode. For faster switching we used the transient switching mode of the electronic load, where in a time as short as 3 ms out of 100 ms the cathode can be pulsed negatively.

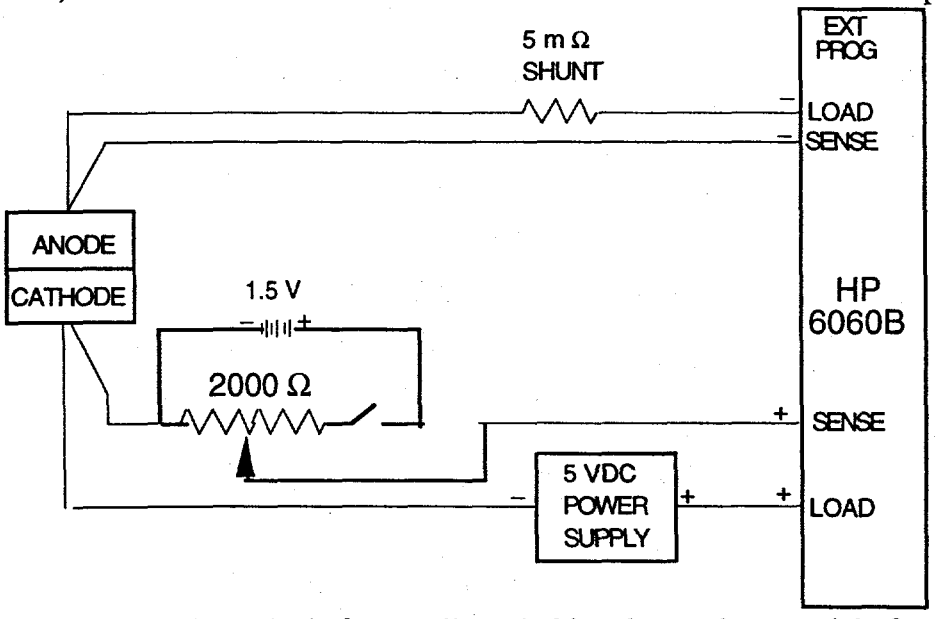

Fig. 16. Simple method of manually switching the anode potential of a test fuel cell relative to the cathode between two levels.

TASK 1 COMPUTER CODES

The computer programming to carry out this study was performed on a Power Macintosh Desktop computer using both *MATHEMATICA* from Wolfram Research Inc. and FORTRAN 77 from Language Systems. Both *MATHEMATICA* notebooks (programs) and FORTRAN source codes and application programs written for this project are available in the computer in SM40, Room N177. For *MATHEMATICA* the analytic solution to Eq. 5 to 7 is in COEQN.NB, evaluation and plots of hydrogen and CO coverage and current densities as a function of potential are in notebook COKIN.NB, effects of diffusion in the catalyst layer are in COBACK.NB. While initial investigation used *MATHEMATICA* , we then produced a set of FORTRAN codes which produced spreadsheet files to make KALEIDAGRAPH plots. These application programs could be used on other computers by MST-11 personnel without needing *MATHEMATICA* or FORTRAN software. The FORTRAN programs also made publication plots easier to produce. The kinetic equation model of hydrogen and CO current density and coverage for a specified gas concentration on a catalyst surface is in source file COKIN.F. The addition of a gas diffusion backing to the kinetic model is in source file COBKKIN.F. This uses subroutines that are in DEVV.F and DVINT.F. The effect of catalyst layer diffusion in modeled in source file CODIF.F. A number of variations to these three basic codes are also present. The application programs have the same name without the ".F" appended.

TASK 1 CONCLUSIONS

Modeling presented here for PEFC performance on H_2 + CO has relied on simple kinetic equations which describe adsorption and electrochemical reactivity of hydrogen and CO at Pt anode catalysts and which depend on the partial pressure of hydrogen and CO employing parameters typical for a temperature around 80°C. The model manages to demonstrate effectively the following features:

Invoking only interfacial kinetic equations (Eq. 1 to 4) and solving analytically for steady state coverage and currents, we have been able to explain the generic form of the polarization curve for a PEFC operating on hydrogen with CO concentrations in the range 10-100 ppm CO (see Fig. 2).

"CO tolerance", i.e., PEFC operation in the presence of about 100 ppm CO in the anode feed stream with excess anode overpotential (additional voltage loss) smaller than, e.g., 50 mV, is achievable with Pt anode catalysts only up to a certain limiting current density. This limiting current value, given by Eq. 11 (typically 50-200 mA/cm^2 at 80°C) is smaller for larger P_{CO} and clearly appears in the model (as in experimental) polarization curves under conditions of high CO coverage and negligible rates of electrochemical stripping of CO. These are the relevant conditions for a Pt anode catalyst at 80°C operating at overpotentials lower than 0.2V. To generate higher current densities, the model shows, in agreement with experiment, that Pt anode overpotentials larger than 0.4V would be required at 80°C. This high overpotential is required to remove CO electrochemically at a substantial rate and corresponds to unacceptably high PEFC voltage losses.

The model shows that steady-state CO coverage can be lowered somewhat by changes of one to two orders of magnitude in either the equilibrium constant for CO adsorption or the very low rate of CO electrochemical stripping around 0.1V. Although the resulting lowering in steady state CO coverage could be quite modest , e.g., from 97% to 90%, the $(1-\theta_{CO})^2$ dependence of the hydrogen oxidation rate brings about large resulting increases in hydrogen oxidation current.

The model shows that anode performance may be improved by lowering only an operational parameter, total anode pressure, if the partial pressure of CO is greater than b_{fc}.

The model indicates a method of measuring equilibrium CO coverage from steady current measurement using decreasing concentrations of H_2/CO mixtures diluted in helium is possible.

Performance improvement from CO liquid diffusion loss in the catalyst layer is not to be expected unless the CO diffusion coefficient were 1% or less of its actual value. Improvement would then occur only at unacceptably high overpotential.

With 50 ppm CO or more, anode performance with is affected much less by dilution than by CO poisoning. Losses through the backing are negligible by comparison. The dilution and backing losses appear to be relatively independent of the CO losses.

Transient effects from changes in CO composition are mostly caused by the storage volume on the catalyst sites rather than by physical gas volume.

Task 2: AC Impedance as Membrane/Electrode Manufacturing Diagnostic Tool

INTRODUCTION

Large scale manufacturing of membrane/electrode assemblies for polymer electrolyte fuel cells will require quality control and assurance. The question has been asked if ac impedance measurements might be used as a diagnostic tool for quality control. We have previously modeled[10] the ac impedance of a working PEM fuel cell, which includes the effects of the cathode catalyst layer, gas diffusion backing and membrane separator resistance. For this preliminary study we will use this model to examine how ac impedance might be used.

Because the exact model that accurately represents all membrane/electrode assemblies with a manageable, finite set of determinable, hopefully physically interpretable parameters does not exist, a feasibility study of the use of ac impedance for manufacturing diagnostics *needs a strong experimental component.*, which at present we do not have. At this initial point in the investigation, we can only speculate on possible ways to perform "on line" impedance measurements and assume that parameters previously extracted from test fuel cells might also represent the impedance that would be measured in a production line test fixture.

AC MODEL AND PARAMETER ESTIMATION

Assumptions

Figure 17 shows schematically the backing and catalyst layers in the cathode and anode. Because of the much higher activity of hydrogen relative to oxygen, the anode tends to serve as a counter electrode and reference. The ac model is of cathode performance and considers the cathode gas diffusion backing and the cathode catalyst layer. The assumptions of the model[10] are similar to those in a previous steady state model[8]. These include:

- uniform effective ionic conductivity σ in the catalyst layer
- uniform effective oxygen diffusion coefficient D in the catalyst layer
- negligible electronic resistance throughout the electrode
- uniform porosity in backing with gas transport following Stefan-Maxwell equations and with water vapor assumed saturated.

For the ac model, we use these additional assumptions:

- uniform double layer capacitance within the catalyst layer
- uniform O_2 storage capacity throughout the catalyst layer.

Refer to the previous papers for the model equations themselves.

Least Squares Fitting

By least squares fitting measured impedance data to the model, we can extract estimates for the membrane of ionic resistance, R_{mem}, and for the cathode of catalyst layer resistance, R_{cl}, catalyst layer characteristic diffusion current density, I_D, catalyst layer kinetic current density, $A_r i^*$, catalyst layer double layer capacitance, C_{DL}, and gas diffusion backing tortuosity, τ. By extracting some of these parameters we conceivably could identify certain malfunctions in the manufacturing process .

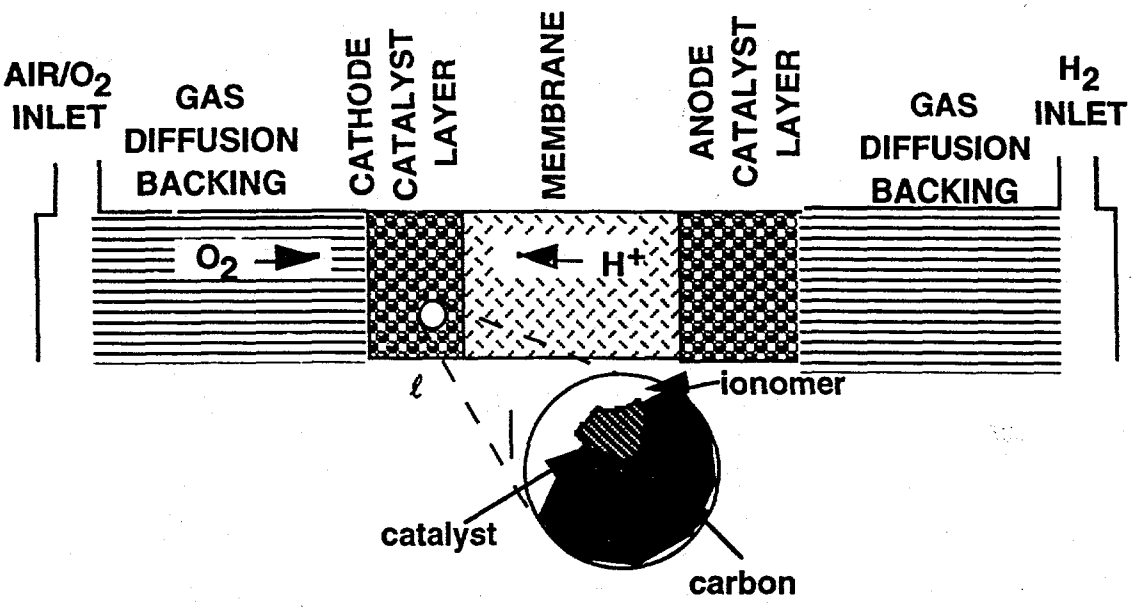

Fig. 17. Schematic of fuel cell, which could represent a diagnostic cell for membrane/electrode quality measurements.

Our previous paper on ac impedance showed that some of the extracted parameters which were assumed to be independent of operating potential or current density, actually varied with potential. (See Ref. 10, Tables I to III.) We pointed out that better estimates of the model parameters could be obtained by fitting simultaneously several impedances measured at different cathode potentials. The fact that parameter estimations, which were assumed to be independent of cathode potential, actually varied some, indicates that the present model is incomplete. For example, it does not consider that water content may change in the electrode with different operating conditions. The present model does reproduce all the features observed in impedance data for a range of cathode potentials, as can be seen in Fig. 18a and 18b (Ref. 10, Fig. 5). The value of ac impedance as a diagnostic tool is not limited by the incompleteness of the model because one can compare measured impedance data from a known optimized membrane/electrode assembly or from one with a known defect to a measured impedance from an electrode assembly under test.

Previously with the simultaneous fitting at different potentials, we were interested in evaluating the model's ability to match physical impedance data. When we use ac impedance as a diagnostic tool, we will probably find it more useful to extract parameters from a spectrum at a single overpotential. The variance in the estimate of the fitted parameter will then be much tighter. Parameter estimation techniques are discussed by Beck and Arnold[11]. The choice of potential may depend on which failure mechanism is being sought. Several potentials may be used, with separate fitting of parameters for each.

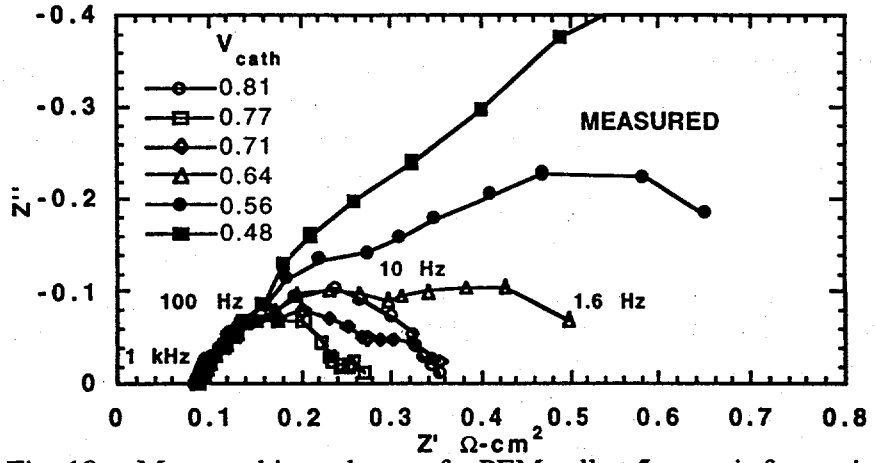

Fig. 18a. Measured impedance of a PEM cell at 5-atm air for various cathode potentials.

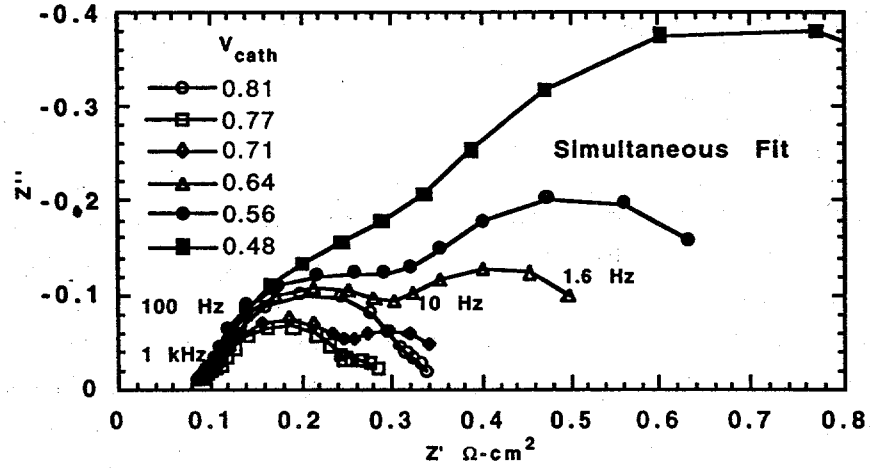

Fig. 18b. Simultaneously fitted impedances for data in Fig. 18a Legend is the same.

IMPEDANCE VARIATION PREDICTED FROM MODEL

Plotting Impedance

For this preliminary analysis of ac impedance usage for diagnostics, we can postulate a series of possible unintended modifications of a working fuel cell and model the expected impedance with that modification. We will assume that all other parts of the cell remain in proper order. We will associate these unintended modifications with a variation of some parameter of the model and see what the expected impedance change might be. Impedance associated with electrochemical systems is normally plotted in the Nyquist plane, which plots the locus as frequency varies of the impedance in the real / imaginary plane. The shape of the loops in this plot generally indicates the equivalent

circuit representing the process. The role of frequency in this plot can only be incorporated by noting the position along the locus of various frequencies. Because we are now interested in variation in impedance from that of a "good" or "typical" cell, we may find Bode plots of log-magnitude and phase as a function of log-frequency to also be useful, so that features shifted in frequency will be more apparent. However, the numerical value of the phase in a normal Bode plot loses some of its interpretive capability when another resistance is in series with the portion of the impedance we wish to detail.

We cite an example that might represent an ionic resistance R_1 in series with a simple charge transfer resistance R_2 in parallel with a double layer capacitance C. The Nyquist plot of such an impedance is shown in Fig. 19a. The impedance point at ω=0.25 radian/s is indicated by a dot. Values of R_1, R_2, and C are indicated. For a Bode plot the length of the dashed line from the origin to the point represents the magnitude and the angle $\Phi_{int} = \text{Atan}(Z_{imag} / Z_{real})$ represents the phase. The numerical value of this "integral" phase only has real significance near the origin and only if the locus approaches the origin.

One way to force this condition would be to first determine the high frequency resistance and then subtract it from the measured impedance. Using the measured data of Fig. 18a we can subtract the resistance of about 0.08 Ω-cm^2 where the high frequency locus hits the real axis. The remaining impedance approaches the origin in this case at about 45°, indicative of distributed resistance and capacitance in the catalyst layer.

A second way would be to use what we term "differential" phase, also depicted in Fig. 19a. $\Phi_{dif} = A\tan\left[\frac{dZ_{imag}}{d\omega} / \frac{dZ_{real}}{d\omega}\right]$. This can help us not only resolve the same features that could be seen in the Nyquist plot, but also to associate the features directly with a particular frequency. Figure 19b shows the associated Bode plot with magnitude, Φ_{int}, and Φ_{dif}. We can see from Φ_{dif} that the Nyquist locus goes from straight up (-90°) to straight down (90°) as we go from low frequency to high frequency. This is not apparent with Φ_{int}. For now in the cases that follow we will use the former method of subtracting the high frequency resistance from the total impedance and will plot the normal type of phase. However, differential phase plots may be useful to us later.

Model Parameter Variation in Cathode Model

The model for ac impedance has been described in Ref. 1. The parameters for the base case are listed here in Table IV. The base case parameters correspond to those we have extracted fitting typical fuel cell impedance data. By varying one parameter at a time, we compare the predicted impedance of the base case to that in which the catalyst layer conductivity, O_2 diffusion coefficient, and catalytic activity are respectively lowered by a factor of ten. The results appear in Fig. 20 for a low cathode overpotential η of 0.1 V and in Fig. 21 for a higher overpotential η of 0.3 V. These impedances are modeled as if the high frequency resistance R_{hf} is zero to enhance the usefulness of the phase plot, as discussed earlier. The use of high frequency resistance as a diagnostic will be discussed later, as it is independent of the cathode model. It is usually considered to be a measure of R_{mem}, the membrane resistance.

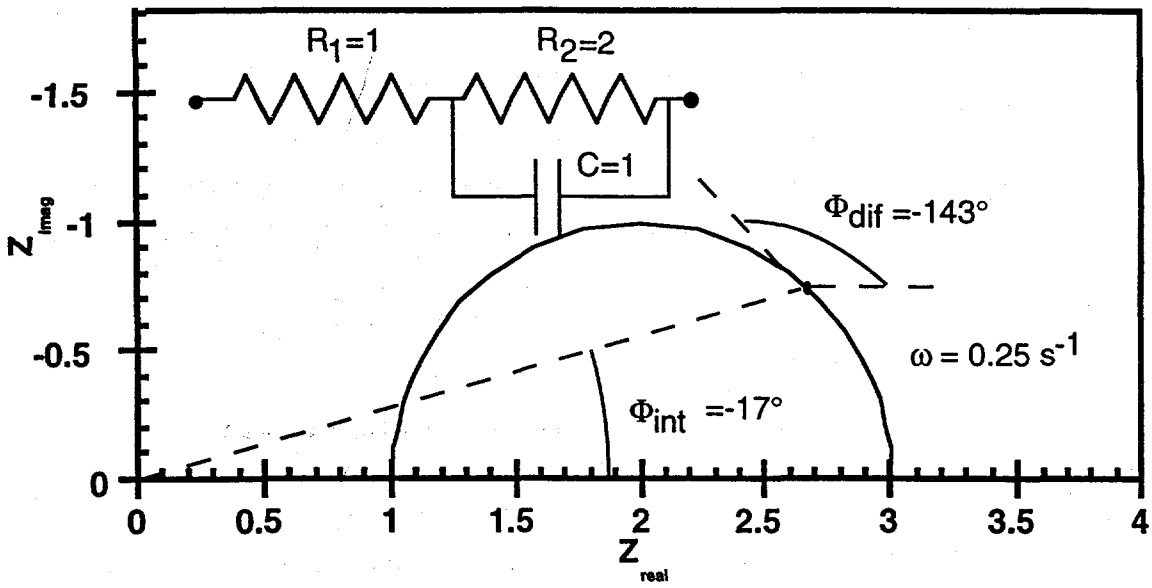

Fig. 19a. Example Nyquist plot with integral and differential phase Φ indicated.

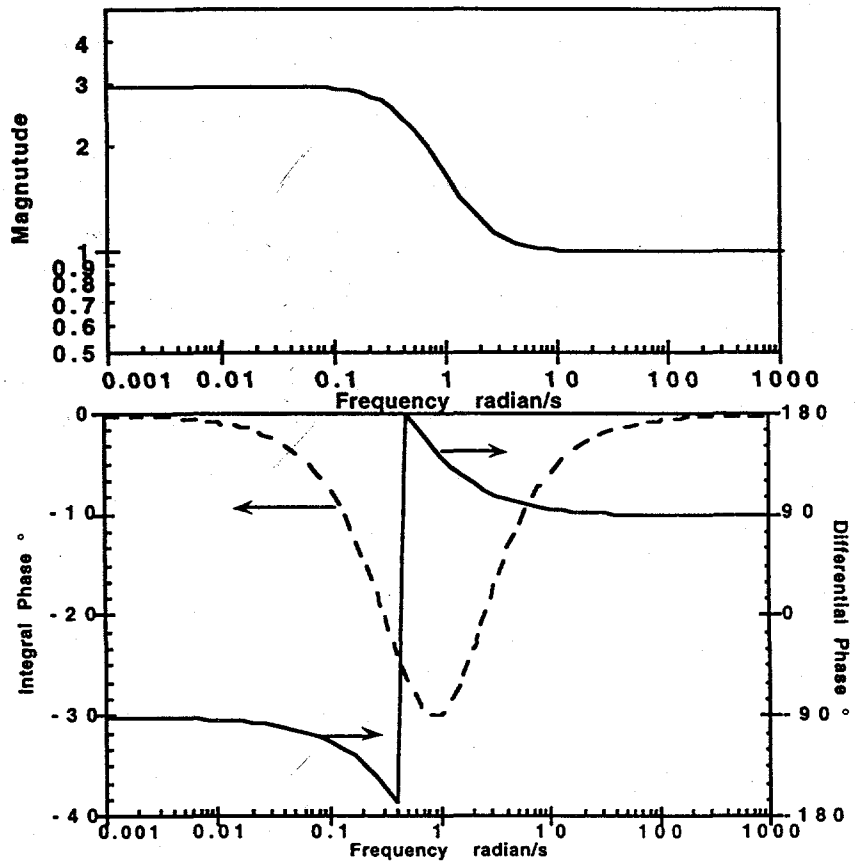

Fig. 19b. Bode plot of example impedance of Fig. 19a showing integral and differential phase.

Table IV. Base Case Parameters

R_{HF}	0.08	Ω cm^2	High frequency resistance
R_{CL}	0.106	Ω cm^2	Catalyst layer resistance
$I_D=4FC^*D/\ell$	0.984	A/cm^2	Characteristic diffusion current density
$A_r i^*$	.0328	A/cm^2	Current density per atm O_2 at .9 V RHE
τ	7.7	-	Backing tortuosity
ℓ	5	μm	Catalyst layer thickness
ℓ_B	300	μm	Backing thickness
C_{DL}	0.0137	F/cm^2	Double layer capacitance
ε_B	0.4	-	Backing porosity

We note for the lower overpotential case in Fig. 20 that the high frequency data can reveal the increase in R_{cl}, the catalyst layer resistance, but provides no information about changes in I_D or $A_r i^*$. The 45° phase shift at high frequency, indicative of distributed resistance, is extended to lower frequency (>20 Hz) and the magnitude of the impedance is increased by the square root of the change in R_{cl}. The low frequency impedance gives us information on the catalyst kinetics where the change in impedance is inversely proportional to the change in $A_r i^*$. In the Nyquist plot we can see a minor increase in impedance at low frequencies when the diffusion parameter I_D is lowered, but the change is hardly apparent on the Bode plot.

Looking at the higher overpotential case in Fig. 21 we see R_{cl} at high frequency is still the only parameter whose change is revealed. At low frequency the fractional shift in magnitude is much more apparent than in Fig. 20. This is seen either Fig. 21a or 21b. Thus effects of catalyst layer O_2 diffusion problems would be best observed at lower frequency and higher overpotential.

In all cases the impedance above 300 Hz is the same for all potentials. In this region only ionic resistance and double layer capacitance control the impedance.

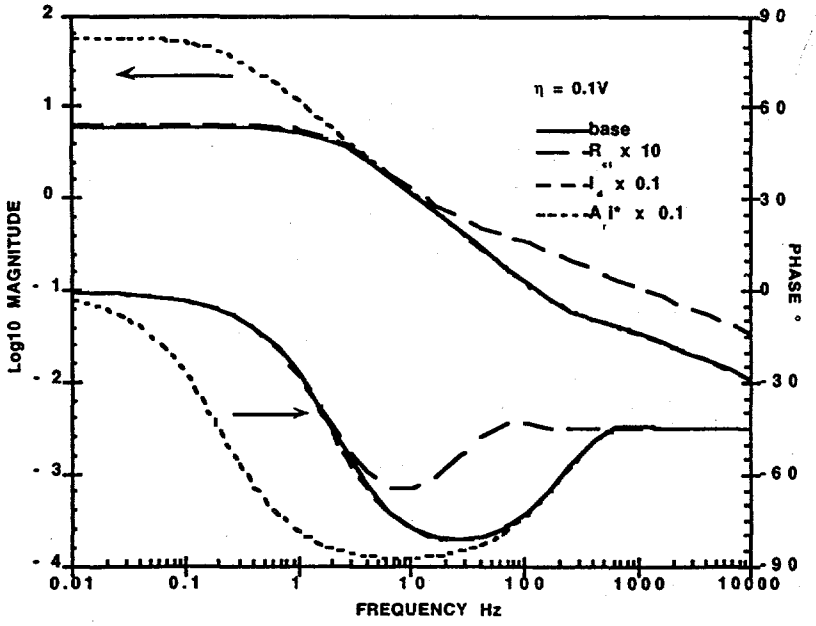

Fig. 20a. Bode plot of impedance for base case and three variations of parameters for overpotential of 0.1 V.

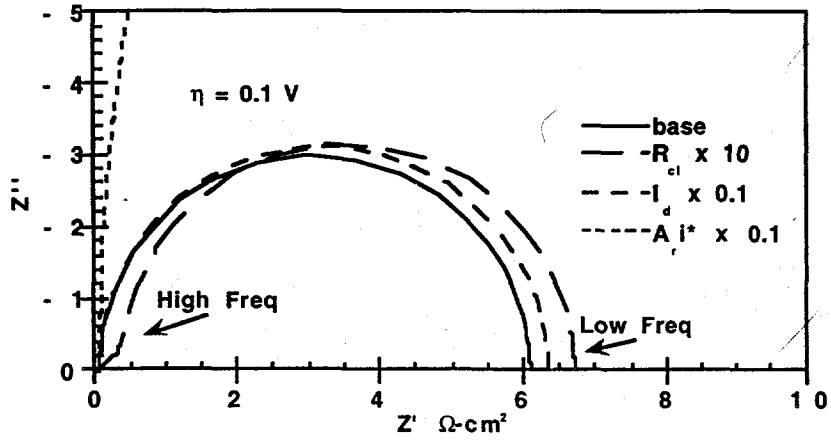

Fig. 20b. Corresponding Nyquist plot for Fig. 20a.

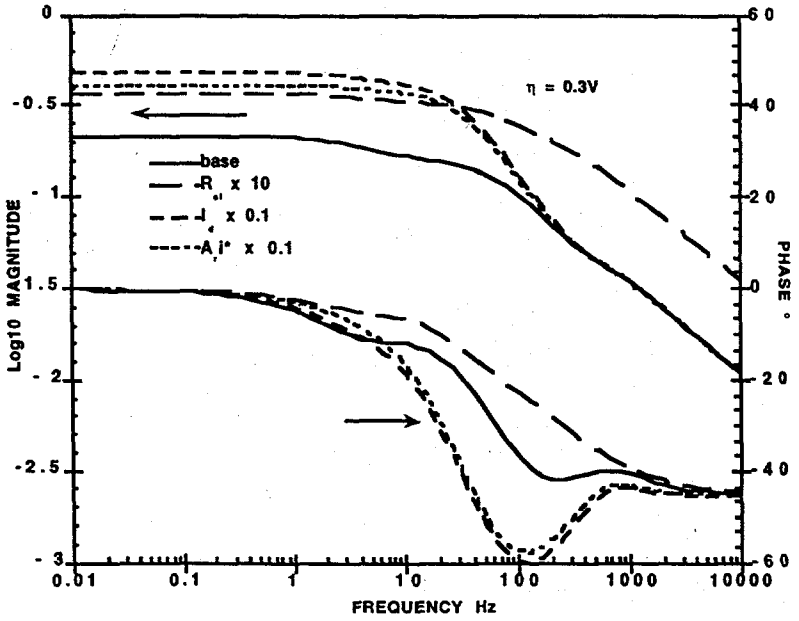

Fig.21a. Bode plot of impedance for base case and three variations of parameters for overpotential of 0.3 V.

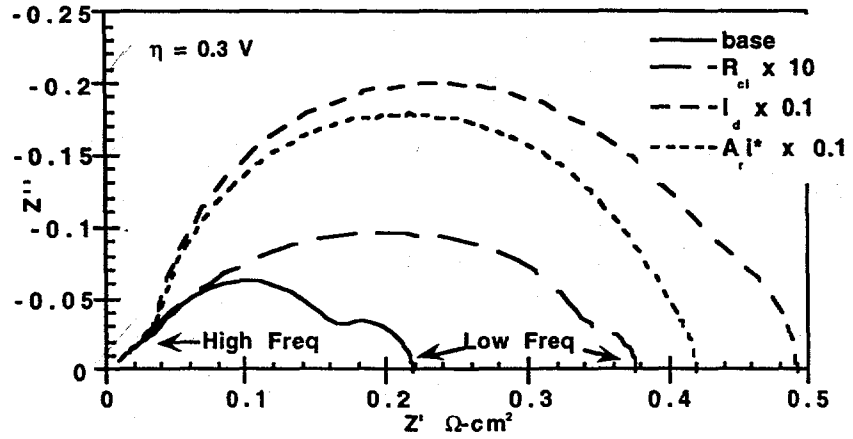

Fig. 21b. Corresponding Nyquist plot for Fig. 21a.

IMPEDANCE VARIATIONS PREDICTED FROM FAILURE MECHANISMS

Although there are electrodes on both sides of the membrane, one could distinguish them by reversing reactant gases. This assumes each electrode is active to both gases, as would be the case with platinum. For the following failures, we assume the opposite electrode is a normal hydrogen anode.

Delamination

If a fraction f of the electrode area delaminated and the remaining part under test remained intact, we might expect that no current would pass through the delaminated

area. Because the thickness of the membrane and two catalyst layers is less than .02 cm while the width is several cm, we can assume one dimensional current flow. We would then expect the voltage/current density relation over the undelaminated portion to remain unaffected. The average impedance of the total test cell would increase by $Z_{delaminated} = Z_{normal} / (1-f)$. We would expect to see the same phase shift at all frequencies and all potentials, but the magnitude uniformly increased.

Membrane Resistance Shift

During the manufacturing process the Nafion membrane separator starts in the sodium form and the catalyst layer ionomer ink in the tetra butyl ammonium form. After pressing the electrodes to the membrane and passing the assembly through H_2SO_4 and water wash baths, both separator and catalyst layer ionomers should be converted to the protonic form. The conductivity of Nafion at 80°C is about 0.1 S/cm in protonated Nafion as opposed to about 0.02 S/cm in sodium form[4]. Xu and Pak[5,6] report at 12°C in Dow shorter-side chained XUS membranes a conductivity of 0.019 S/cm and 0.0062 S/cm respectively in the protonated and sodium forrms. The conductivities of the XUS membranes and their ratio should both be greater at higher temperatures, according to their variation with temperature at 12°C. Thus we might expect the base case high frequency resistance to increase from .08 Ω cm^2 to approximately 0.4 Ω cm^2 if the protonation step failed. We might also expect the membrane resistance to be higher if other contaminants entered it. In addition to providing a diagnostic for this protonation step it is necessary to determine the high frequency intercept of the impedance with the real axis to ensure all Faradaic processes in the electrode have been completely shorted out by the double layer capacitance. This real resistance, which could also include any (hopefully negligible) electronic contact resistance, needs to be subtracted from the measured impedance at lower frequencies before inferring problems in the catalyst layer itself.

No Metal Catalyst Present

If the catalyst were inert, not present, or not in contact with the surrounding carbon, then the impedance at low frequencies should be much higher, while at higher frequencies (>300 Hz) it should be the same.

Poor Electronic Connectivity in Carbon

If the impedance were higher than normal at higher frequencies, we would suspect problems with the carbon in the catalyst layer and the absence of proper electronic connectivity. When the electronic resistance equals the ionic resistance, the 45° phase shift can completely vanish.

Little or No Ionomer in Catalyst Layer

If the catalyst ionic resistance is greatly increased, we would observe the increased impedance in the 45° phase region, as discussed earlier. One might get a quantitative measure of this increased ionic resistance.

TASK 2 COMPUTER CODES

The FORTRAN source codes that were written to compute the ac impedance expected under certain fuel cell abnormalities are available in the Macintosh 8100 computer in SM40, Room N177.

FCIMPFIT.F fits measured impedance data by least squares to the model and estimates the parameter values of R_{cl}, I_D, A_ri^*, C_{DL} and τ. While it can fit multiple spectra obtained at different overpotentials, fitting a single spectrum at one potential is preferred for diagnostic use.

ACDIAG3.F provides spreadsheet impedance data of frequency, Z_{real}, Z_{imag}, log magnitude, and phase using the ac impedance model. Cell parameters are supplied by the user on file ACMODEL3.IN and spreadsheet data for KALEIDAGRAPH is written into ACMODEL.OUT.

The example impedance used in Fig. 19a and 19b illustrating Nyquist, Bode and differential phase forms of impedance is calculated in DIFPHASE.F and results are in DIFPHASE.OUT.

TASK 2 CONCLUSION

The present investigation does not address the question of how a diagnostic test cell is implemented on a membrane/electrode production line. Using a model for a working fuel cell, we have examined how the impedance might be affected following certain malfunctions. Some of the conclusions reached follow.

A strong experimental component to the investigation is needed before deciding on the validity of ac impedance as a production line diagnostic tool.

Measured impedances of real failures using real test fixtures should ideally be used in fault determination.

Parameter estimation by least squares fitting can pinpoint an electrode fault.

Bode plots and differential phase plots may be a useful tool for diagnostic analysis.

Partial delamination would be indicated by a phase plot similar to normal but a uniformly increased magnitude plot as a function of frequency.

An increased magnitude above 300 Hz and extension of the 45° phase region to lower frequency can indicate ionic resistance problems in the catalyst layer.

Higher impedance at low frequency can indicate catalyst inactivity.

A factor of 4 to 5 increase in high frequency resistance can indicate a membrane in the sodium form. The catalyst ionic resistance might also be higher.

REFERENCES

1. H. A. Gasteiger, N. M. Markovic and P. N. Ross, *J. Phys Chem.*, **99**, 8290 (1995).

2. H. A. Gasteiger, N. M. Markovic and P. N. Ross, *J. Phys Chem.*, **99,** 16757 (1995).

3. M. Iwase and S. Kawatsu, in *Proton Conducting Membrane Fuel Cells I*, S. Gottesfeld, G. Halpert and A. Landgrebe, Editors, **PV 95-23**, p12, The Electrochemical Society Proceedings Series, Pennington, NJ (1995).

4. T. A. Zawodzinski Jr., C. Karuppaiah, F. Uribe and S. Gottesfeld, *Extended Abstracts*, Electrochemical Society Fall Meeting: San Antonio, TX, October 1996: **Vol 96-2**, Abstract No. 781.

5. C. Karuppaiah, F. Uribe, T. A. Zawodzinski Jr. and S. Gottesfeld, *Extended Abstracts,* Electrochemical Society Spring Meeting: Montreal, Canada, May 1997: **Vol . 97-1**

6. (a) S. Gottesfeld and J. Pafford, *J. Electrochem. Soc.* **135**, 2651-2652 (1988);
(b) M. S. Wilson, T. E. Springer, T. A. Zawodzinski, and S. Gottesfeld, *Proceedings of the 28th Intersociety Energy Conversion Engineering Conference*, 1993, Atlanta, Georgia, Vol 1, pp. 1203-1208.

7. W. Vogel, J. Lundquist, P. Ross and P. Stonehart, *Electrochim. Acta*, **20** , 79 (1975)

8. T. E. Springer, M. S. Wilson and S. Gottesfeld, *J. Electrochem. Soc.* **140,** 3513 (1993).

9. R. H. Perry and D. W. Green, Chemical Engineers' Handbook 6th Ed, McGraw-Hill (1984).

10. T. E. Springer, T. A. Zawodzinski and S. Gottesfeld, *J. Electrochem. Soc. **143,** 587 (1996).*

11. J. V. Beck and K. J. Arnold, *Parameter Estimation in Engineering Science* , John Wiley & Sons, New York (1977).

12 T. A. Zawodzinski, Private communication.

13. G. Xu and Y. S. Pak, *J. Electrochem. Soc.* **139,** 2871 (1992).

14 C. S. Zaluski and G. Xu, *J. Electrochem. Soc.* **141,** 448 (1994).

FINAL REPORT

PART 2

for Group MST-11
Los Alamos National Laboratory

Subcontract F01230017-3L
WEIRICH and ASSOCIATES, INC.

Task 3: Modeling Aspects of Direct Methanol Fuel Cells

work performed by
Thomas E. Springer

January 30, 1998

Task 3: Modeling Aspects of Direct Methanol Fuel Cells

INTRODUCTION

The improved catalytic activity of platinum-ruthenium alloy anode catalysts for electrooxidation of methanol in direct methanol fuel cells DMFCs using perfluoro-sulfonate ionomer membranes and electrode impregnants has prompted much research activity in this field. The improvement over use of a pure Pt anode catalyst results from the bifunctional role of an approximate 50 a/o Pt/Ru catalyst in which adsorbed methanol is first partially oxidized to form adsorbed CO on a Pt surface[1].

$$CH_3OH_{ads} \rightarrow CO_{ads} + 4H^+ + 4e^- \qquad [1]$$

For this reaction to proceed continuously the adsorbed CO must also be electro-oxidized. This requires a two step process:

$$H_2O \leftrightarrow OH_{ads} + H^+ + e^- \qquad [2]$$

which proceeds much faster on Ru (at 0.2 V) than on Pt (at 0.5 V), followed by:

$$CO_{ads} + OH_{ads} \rightarrow CO_2 + H^+ + e^-. \qquad [3]$$

The latter 2 equations are the same processes occurring in the CO poisoning treated in Task 1. However there the CO was introduced as a gas whose partial pressure could be separately adjusted relative to the accompanying fuel hydrogen gas. In this case the attached CO bond results from and is inseparable from the methanol fuel. The overall reaction is limited by the rate that OH_{ads} can be electrooxidized. The overall reaction is independent of MeOH concentration. Thus in the ensuing modeling we can treat the anode kinetics as reversible with an exchange current density and a similar forward and backward Tafel slope.

Because we believe the most valuable contribution of modeling to understanding and optimizing the DMFC concerns mass transport issues, we will address certain processes relevant to the DMFC involving diffusion, migration, electroosmotic drag, and convection. As is our usual philosophy, we will use simple models and solutions that will still capture the essence of the physical phenomena involved, will give the correct understanding of the processes involved, and should predict observable results in the laboratory.

The models address fuel efficiency and cell efficiency. We shall examine methanol crossover to the cathode and its effect on cell voltage at a given current density. For this evaluation we have found a simpler approximate solution for our previous cathode model[2] that still includes the catalyst layer resistance and oxygen diffusion loss. Methanol crossover involves diffusion effects in the anode backing and diffusion and electroosmotic drag effects in the membrane separator. Because direct removal of methanol crossover flux may be possible by use of tubulated membranes through which water flows, this option is examined, as is the possibility of recycling some or all of the removed methanol into the anode feed stream. Finally, the need for a compact DMFC power supply has prompted development of bipolar anode/ cathode methanol and air feed plates made of shaped metal foil, for which we have calculated the expected pressure drop.

DESCRIPTIVE EQUATIONS FOR DMFC ANODE AND CATHODE

In this section we will extend some of our previous modeling of hydrogen /air fuel cell electrodes to the DMFC. For the anode decreased kinetic activity will make resistance effects more prominent, but concentration effects will disappear because the activity is independent of methanol concentration. We have also simplified solution methods for the cathode catalyst layer model.

Anode Model

Methanol crossover affects the cathode potential, so we need to represent both anode and cathode overpotential as a function of current density. The overall anode reaction resulting from Eq. 1 to 3 on .5/.5 PtRu catalyst is

$$CH_3OH + H_2O \rightarrow CO_2 + 6H^+ + 6e^- . \qquad [4]$$

Because the reaction is zeroth order in MeOH concentration until starvation occurs, a simple kinetic equation appears to represent the anode when adequate methanol is present and when catalyst layer resistance is neglected.

$$J_a = i_{oa}A_{ra}\left(e^{\frac{\eta_a}{b_a}} - e^{-\frac{\eta_a}{b_a}}\right) = 2i_{oa}A_{ra}\sinh(\frac{\eta_a}{b_a}) \text{ or } \eta_a = b_a \operatorname{asinh}\left(\frac{J_a}{2i_{oa}A_{ra}}\right) \qquad [5]$$

Typical values for $i_{oa}A_{ra}$ and b_a are 10^{-5} A/cm^2 and 0.033 V. The quantity i_{oa} is the exchange current density on a Pt Ru surface and A_{ra} is the catalyst area per geometric area. Laboratory experience indicates that there is negligible MeOH concentration drop in the catalyst layer, but ionic or electronic resistance in the catalyst layer may be present. This may be because electronic conduction is through Pt and Ru black, rather than carbon. If the anode potential is well above b_a we can neglect the reverse reaction and use a simple exponential function Tafel relation to get an analytic solution for anode overpotential that includes catalyst layer resistance. Figure 1 shows how electronic current gets progressively converted to ionic current along the fractional distance y through the catalyst layer. Equation 6 describes the change in currents and potentials through the catalyst layer. The sum of the ion current plus the electron current at any point y always adds to the total current density J so I^- can be eliminated.

$$\frac{\partial I^+}{\partial y} = i_{oa}A_{ra}\exp\left(\frac{\eta_d}{b_a}\right); \quad \frac{\partial \eta_d}{\partial y} = \frac{\partial \eta^+}{\partial y} - \frac{\partial \eta^-}{\partial y} = R_a^+ I^+ - R_a^-\left(J - I^+\right) \qquad [6]$$

In Eq. 7 and 8 we equate dy to several other differentials, then separate variables and relate I^+ and η_d across the catalyst layer if we specify η_{do} at the feed side of the catalyst layer (y=0). We can determine the local overpotential η_d driving the electron exchange reaction and the current density everywhere without having to solve for η^- or η^+. We can integrate later to get this contribution to the total anode overpotential.

$$\int_0^y dy = \int_{\eta_{do}}^{\eta_d} \frac{d\eta_d}{(R^+ + R^-)I^+ - R^- J} = \int_0^{I^+} \frac{dI^+}{i_{ao}A_{ra}e^{\eta_d / b_a}} \qquad [7]$$

$$\int_{\eta_{do}}^{\eta_d} i_o e^{\eta_d / b_a} d\eta_d = \int_0^{I^+} \left[(R^+ + R^-)I^+ - R^- J\right] dI^+ \qquad [8]$$

$$i_{ao}A_{ra}b_a\left[e^{\eta_d/b_a}-e^{\eta_{do}/b_a}\right]=(R^+ + R^-)I^{+2}/2 - R^- JI^+ \qquad [9]$$

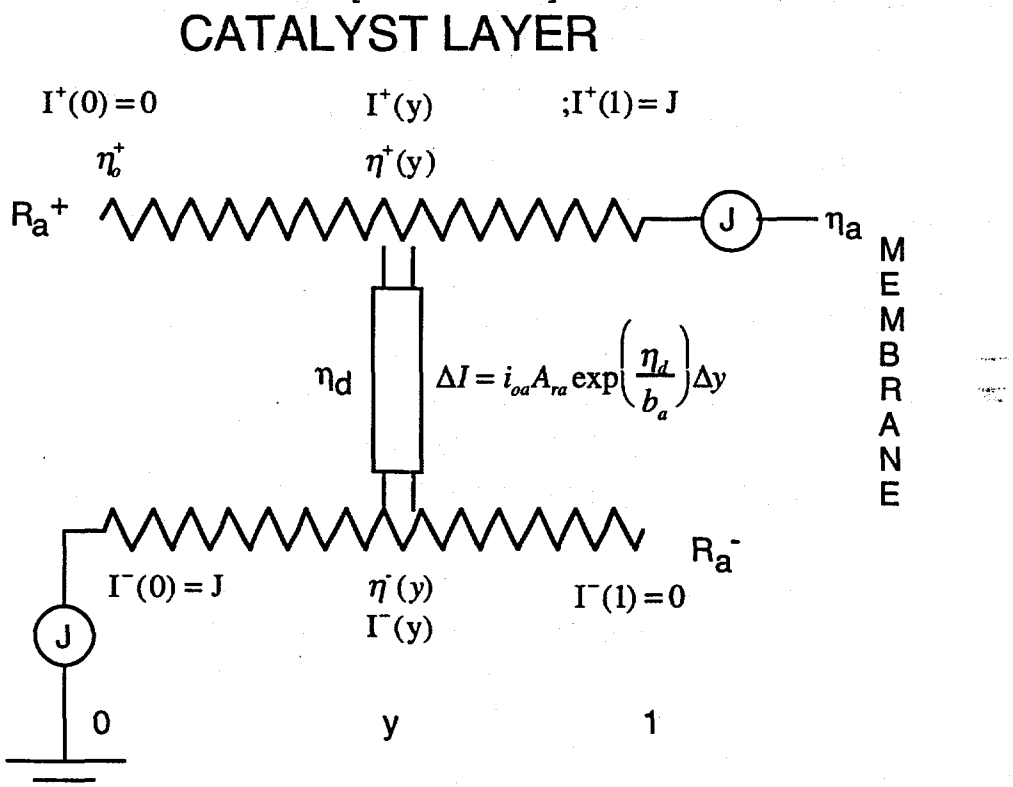

Fig. 1 Schematic diagram of anode with both ionic and electronic resistance

Define $J_{kin} = i_{oa}A_{ra}e^{\eta_{ao}/b_a}$ to be the kinetic current density at the specified η_{do}. We can determine the total current density J for a specified η_{do} by recognizing that the leftmost integral in Eq. 7 equals 1 when y=1 and by expressing the denominator of the right hand integral of Eq. 7 in terms of I^+ from Eq. 9. This gives an implicit relation that determines J.

$$1=\int_0^J \frac{b_a dI^+}{(R^+ + R^-)I^{+2}/2 - R^- JI^+ + b_a J_{kin}} = \qquad [10]$$

$$\frac{A\tan\left[\dfrac{0.5JR^-/b_a}{\sqrt{.5J_{kin}(R^+ + R^-)/b_a - \left(.5JR^-/b_a\right)^2}}\right] + A\tan\left[\dfrac{0.5JR^+/b_a}{\sqrt{.5J_{kin}(R^+ + R^-)/b_a - \left(.5JR^-/b_a\right)^2}}\right]}{\sqrt{.5J_{kin}(R^+ + R^-)/b_a - \left(.5JR^-/b_a\right)^2}}$$

For the special case when $R^-=0$, Eq. 10 can be solved explicitly for J and Eq. 9 can be used to get η_a.

$$J = J_{kin}\tan\sqrt{\frac{J_{kin}R^+}{2b_a}}\Big/\sqrt{\frac{J_{kin}R^+}{2b_a}};\quad \eta_a = b_a\log\left[\frac{R^+J^2}{2i_{oa}A_{ra}b_a}+e^{\frac{\eta_{ao}}{b_a}}\right];\quad J_{kin}=i_{oa}A_{ra}e^{\frac{\eta_{ao}}{b_a}} \qquad [11]$$

We see that for negligible catalyst layer resistance, the current density approaches J_{kin}, as we would expect, and otherwise is greater than J_{kin}.. Likewise because the argument of the tangent can never be greater than $\pi/2$, the value of J_{kin} will approach $\pi^2 b_a/(2R^+)$. as the applied potential η_a at the membrane interface becomes very large. For the case when there is only electronic resistance, we get a similar condition, but we have to specify j_{kin} at the membrane side of the catalyst layer. For the general case we used Eq. 10 to determine J and then integrated numerically by the Runge Kutta method to get $\eta^-(1)$. Figures 2a-2c show the local current density and the overpotentials η^- and η^+ through the catalyst layer for a total resistance of 0.3 Ω cm^2 on the ion side, on the electronic side, and equally split. For the equally split case (Fig 2c) the minimum current production is in the center. The applied overpotential is 0.34 for each case, but the current density is less if the resistance is equally split. If all the resistance is on the ion side, at least the electrochemical interface at y=1 sees the whole overpotential to drive the electron exchange exponentially, whereas in the split case no interface ever sees this full potential, so the average current density is less for a given applied potential.

Figure 3 shows predicted anode overpotential for several assumed ionic catalyst layer resistances. A set of experimental data is overlaid on the curve.

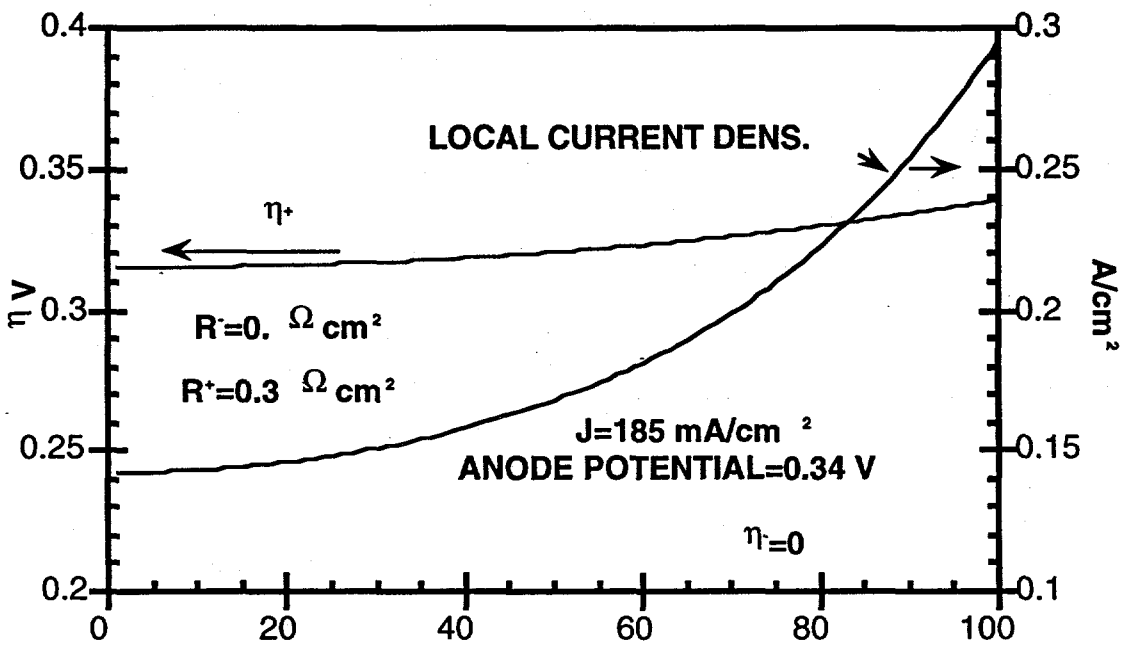

Fig. 2a. Anode current generation and local overpotential with ionic resistance of 0.3 Ω cm^2. Kinetic parameters are i_{oa} A_{ra}= 10^{-5} A/cm^2 and b_a= 0.033 V.

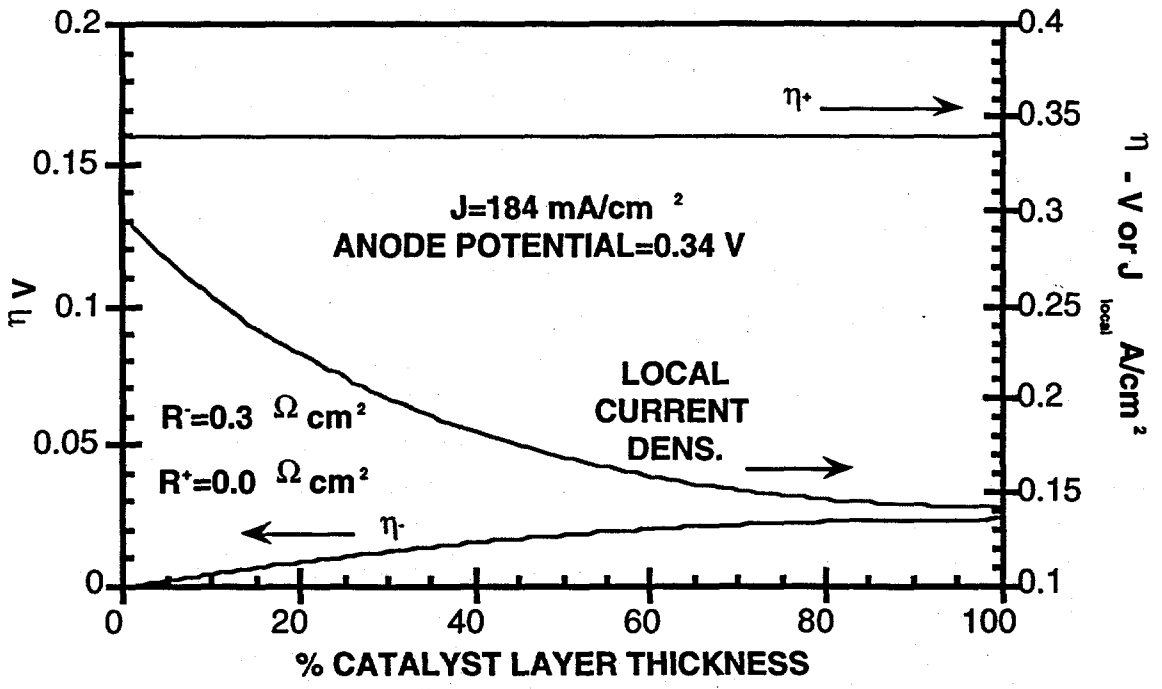

Fig. 2b. Anode current generation and local overpotential with electronic resistance of 0.3 $\Omega\,cm^2$. Kinetic parameters are i_{oa} A_{ra}= 10^{-5} A/cm^2 and b_a= 0.033 V.

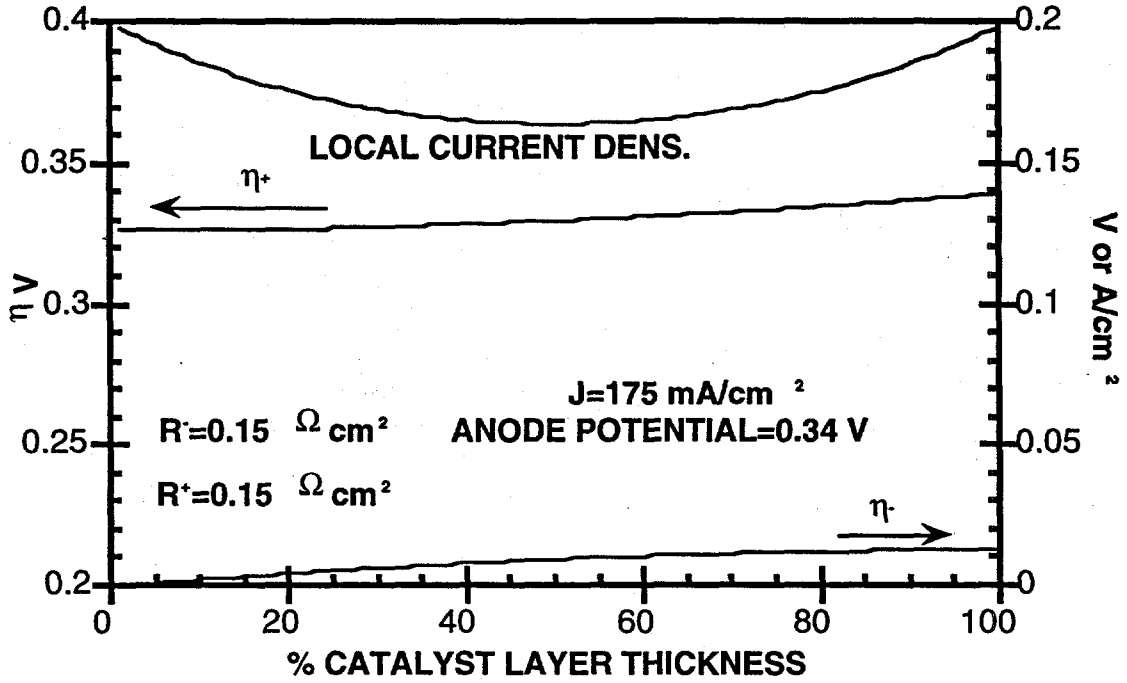

Fig. 2c. Anode current generation and local overpotential with ionic and electronic resistance split equally at 0.15 $\Omega\,cm^2$. Kinetic parameters are i_{oa} A_{ra}= 10^{-5} A/cm^2 and b_a= 0.033 V.

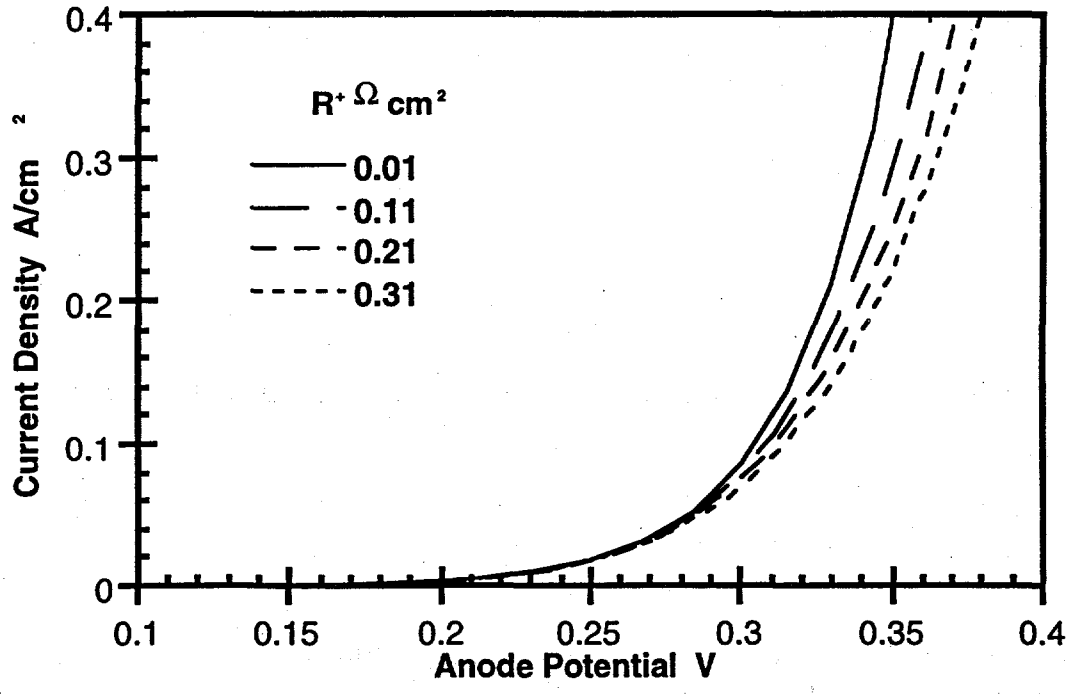

Fig. 3. Anode current density vs overpotential using Eq. 11 with $i_{oa}A_{ra} = 10^{-5}$ A/cm^2 and b_a =0.033 V.

Cathode Model

For the cathode we have developed a simpler model than was used in our earlier work[2] which requires an iteration on explicit equations but no integration or matrix solutions. This model still incorporates kinetics, O_2 catalyst layer diffusion losses, and catalyst layer resistance, but eliminates much of the calculation used previously. We start from Eq. A-2 to A-4 in Ref. 2 but let η_o be an average overpotential use to determine the concentration profile and current density and $\eta'(y)$, the additional overpotential due to ionic resistance along the fractional distance y through the catalyst layer when using an average concentration. The equations describing this overpotential η', the local current density I(y) and the local concentration ratio C'(y) to that at y=0 are:

$$\frac{\partial \eta'}{\partial y} = IR_{cl} \qquad [12$$

$$\frac{\partial I}{\partial y} = p_{ox} i^* A_{rc} C\, e^{\eta_o / b_c} e^{\eta' / b_c} \qquad [13]$$

$$\frac{\partial C}{\partial y} = \frac{I - J_c}{p_{ox} I_D} \qquad [14]$$

The boundary conditions are I(0)=0, C'(0)=1, and we arbitrarily set $\eta'(0)=0$ so that $\eta'(1)$ will represent the total overpotential loss from ionic resistance. At the membrane side of the cathode catalyst layer $I(1)=J_c$, the total cathode current density. R_{cl} is the catalyst layer resistance, p_{ox} is the O_2 partial pressure at the backing/catalyst layer interface and is a function of current density because of the backing, and I_D is the characteristic diffusion current density ($4FC^*D/\ell$ where C^* is the O_2 concentration in equilibrium with 1 atm and D

is the effective diffusion coefficient in the catalyst layer.) We simplify the solution by noting that Eq. 12 and 13 can be solved analytically if C' is constant, and that Eq. 13 and 14 can likewise be solved analytically if η' is constant (or zero). Using the latter two equations:

$$C(1) = \operatorname{sech}\sqrt{\frac{i^* A_{ra} e^{\eta_o / b_c}}{I_D}};\ \bar{C}' = \int_0^1 C(y)dy = \tanh\sqrt{\frac{i^* A_{ra} e^{\eta_o / b_c}}{I_D}} \Big/ \sqrt{\frac{i^* A_{ra} e^{\eta_o / b_c}}{I_D}} \quad [15]$$

$$J_c = p_{ox}\sqrt{i^* A_{ra} e^{\eta_o / b_c} I_D}\tanh\sqrt{\frac{i^* A_{ra} e^{\eta_o / b_c}}{I_D}} \quad [16]$$

Eliminate ∂y from the former two equations , use $\bar{C}'$, and separate variables getting:

$$R_{cl} I dI = p_{ox} i^* A_{ra} e^{\eta_o / b_c} \bar{C}' e^{\eta' / b_c} d\eta';$$

$$R_{cl} J_c^2 / 2 = p_{ox} i^* A_{ra} e^{\eta_o / b_c} \bar{C} b_c \left(e^{\eta'(1)/b_c} - 1\right) \approx p_{ox} i^* A_{ra} e^{\eta_o / b_c} \bar{C} \eta'(1); \quad [17]$$

$$\eta'(1) = b_c \ln\left[1 + \frac{R_{cl} J_c^2}{2 p_{ox} i^* A_{ra} e^{\eta_o / b_c} \bar{C} b_c}\right] \approx \frac{R_{cl} J_c^2}{2 p_{ox} i^* A_{ra} e^{\eta_o / b_c} \bar{C}}$$

For a given current density J_a solve Eq. 16 implicitly to determine η_o. Then using that average value of C', solve Eq. 11 to get $\eta'(1)$. The cathode overpotential at the membrane/catalyst layer interface, $\eta_\ell = \eta_o + 0.5\,\eta'(1)$.

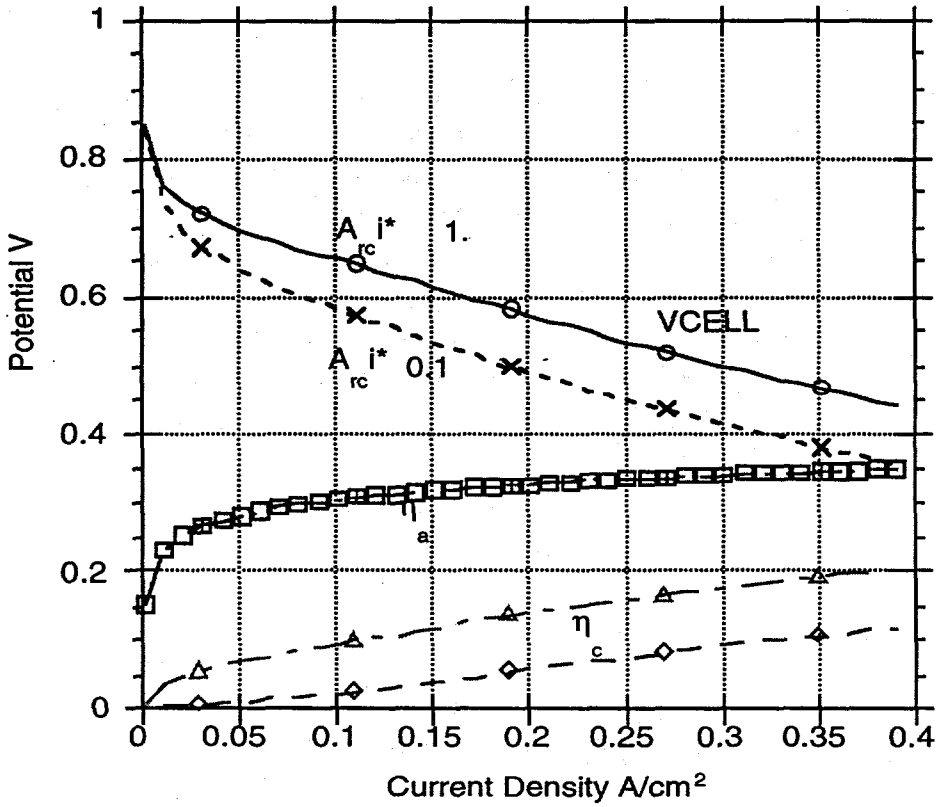

Fig. 4. Cell voltage and anode and cathode overpotentials for 2 cathode catalyst loadings.

Figure 4 shows the cell voltage and anode and cathode overpotentials for 2 different values of cathode catalyst loading, using the model. The parameters of the model are shown in Table I. With an anode and cathode model, we can study the effect of methanol cross over on the cell voltage. We shall indicate the cross-over flux in terms of its equivalent electrooxidized current density, j_m (6F x cross-over flux). Later we use F_{cath} for the average methanol flux to the cathode when it differs from that leaving the anode.

Table I. Model Parameters

$i_{oc}A_{rc}$	0.1 or 1.0 A/cm^2 cathode kinetic parameter
$i_{oa}A_{ra}$	1. x 10^{-5} A/cm^2 anode kinetic parameter
b_a	0.033 V
b_c	0.036.9
T_c	80°C
R_{cl}	0.1 Ω cm^2
p_{ox}	0.21
I_D	0.96 A/cm^2 Characteristic O_2 diffusion current density
I_B	2.5 A/cm^2 Characteristic backing current density
R_{mem}	0.17 Ω cm^2 Membrane resistance

TRANSPORT EFFECTS IN MEMBRANE AND BACKING

Effect of diffusion and electroosmotic drag in membrane

The electroosmotic drag of water through a Nafion® membrane incurred by protonic current has been studied by many groups.[3,4] Similar methanol transport due to electroosmotic drag in Nafion has also been reported.[5,6] For Nafion membranes in contact with liquid water, the total fluid drag coefficient ξ has been measured at 30°C to be 2.5 H_2O/H^+.[7,8] and 2.86 and 3.16 at 60° and 80°C respectively.[9]

Let C_a be the methanol concentration at the anode/membrane interface. Because the methanol diffusion loss is much higher across the backing and membrane than across the thin anode catalyst, we will consider C_a to be the same throughout the anode. Let C_{tot} be the total concentration of fluid, approximately that of water (55.55 moles/li). For diffusion processes we shall let k represent the diffusion coefficient D to thickness τ ratio of a diffusing medium (i.e. D/τ) and the subscripts b and m to refer to the anode backing and membrane. Gottesfeld[10] and Gough[11] use the term "permeability" for k, which has units of cm/s and could be called a superficial velocity[12].

We calculate the normalized MeOH concentration profile $C(y)/C_a=u(y)$ across the membrane as a function of fractional position y from the continuity equation for MeOH flux in terms of equivalent current density j_m across the membrane,

$$\nabla . j_m = 0 = -6FC_a k_m u''(y) + \frac{6 j_a \xi C_a}{C_{tot}} u'(y), \text{ b.c.'s are } u(0)=1,\ u(1)=0. \qquad [18]$$

The solution of this equation is

$$u(y) = \frac{e^{\alpha} - e^{\alpha y}}{e^{\alpha} - 1} \text{ where } \alpha = \frac{j_a \xi}{C_{tot} F k_m} \qquad [19]$$

and the methanol crossover current density is

$$j_m = 6FC_a k_m \frac{\alpha e^{\alpha}}{e^{\alpha}-1} \approx 6FC_a k_m (1+\frac{\alpha}{2}) \approx 6FC_a k_m + 3j_a \xi \frac{C_a}{C_{tot}} \qquad [20]$$

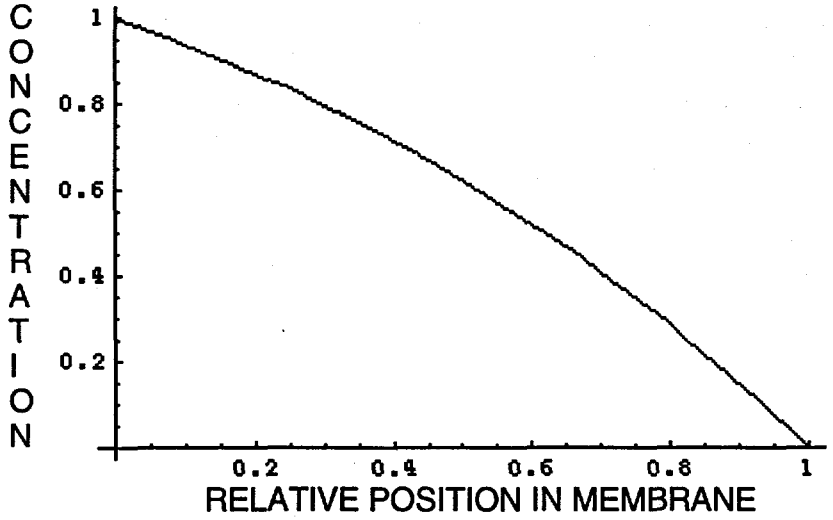

Fig. 5. Normalized methanol concentration through membrane when proton current density is equal to equivalent methanol flux current density (4 molar feed).

We see when α is small that the crossover flux is equal to the expected diffusion flux without drag plus one half the initial drag flux. We shall use the rightmost approximation in Eq. 20 for j_m. Figure 5 shows the methanol concentration profile for $C_a = 4$ molar. As the concentration drops the slope becomes steeper as the diffusion driving force replaces the decreasing drag force.

Backing Effect

Diffusion loss in the anode backing utilizes the methanol consumption in the anode to lower the anode concentration C_a and per Eq. 21 to 23 consequently to lower the resulting crossover flux j_m. Equating the backing flux to the anode consumption plus the crossover flux we get:

$$6Fk_b(C_f - C_a) = j_a + j_m = j_a + 6FC_a k_m + 3j_a \xi \frac{C_a}{C_{tot}} \qquad [21]$$

$$C_a = \frac{6FC_f k_b - j_a}{6F(k_b + k_m) - (3\xi / C_{tot}) j_a} \qquad [22]$$

$$j_m = \left(6Fk_b C_f - j_a\right) \frac{6Fk_m + 3\xi j_a / C_{tot}}{6Fk_m + 6Fk_b + 3\xi j_a / C_{tot}} \qquad [23]$$

In the next few sections we will look at effects of methanol crossover on cell performance. We will find it convenient to ignore electroosmotic drag effects because it simplifies the analysis without affecting the overall understanding or the general conclusions. If we should consider implementing the tubulated membranes to reduce crossover effects, then drag should be included before final consideration. Without drag, Eq. 23 for crossover current density becomes:

$$j_m = \left(6Fk_bC_f - j_a\right)\frac{k_m}{k_m + k_b} \qquad [24]$$

EFFECT OF MeOH CROSSOVER ON CELL VOLTAGE

When methanol reaches the membrane/cathode catalyst interface, it sees the high cathode potential and is electrooxidized according to Eq. 4 in the first small fraction of the catalyst layer near the membrane interface. This reaction produces additional H^+ ions which join the H^+ ions that crossed the membrane from the anode to increase the cathode current density when combining with O_2 in the remainder of the catalyst layer according to:

$$4H^+ + O_2 + 4e^- \rightarrow 2H_2O. \qquad [25]$$

The electron flow for this reaction is opposite to that from the electrooxidation of methanol on the cathode, and only the difference of these two current densities flows in the external circuit. Because the cathode now sees greater current density, it will have a greater overpotential and the cell voltage will be reduced. The cell model uses Eq. 19 to determine cell voltage. Equation 11 for the anode and Eq. 16 and 17 for the cathode are used implicitly to determine η_a and η_c.

$$j_c = j_a + j_m; \quad V_{cell} = V_{oc} - \eta(j_a) - \eta(j_c) - j_aR_{mem} \qquad [26]$$

Equations 23 or 24 described the methanol crossover flux. We will be looking at several possible methods for lowering the methanol flux to the cathode. The simplest method is to increase the membrane thickness. Another, to be discussed later, is the use of flushing water through tubulated membranes to remove some of the methanol crossing to the cathode. If at a particular thickness L_o corresponding to k_{mo} there exists a crossover current density j_{mo} and if the α is the ratio of the actual membrane thickness to that corresponding to k_{mo}, we can determine j_m as a function of membrane thickness αL_o.

$$j_m = \left(6Fk_bC_f - j_a\right)\frac{k_m\alpha}{k_m\alpha + k_b} \qquad [27]$$

Figure 6 illustrates the tradeoff between membrane resistance and cross-over flux obtained by varying membrane thickness for the case of negligible concentration drop across the backing (r=0). The 180 μm thickness (L_{mo}) corresponds to Nafion 117. The cross-over flow for this thickness was taken to be 50 mA/cm^2 and 100 mA/cm^2 respectively. Interestingly, Nafion 117 appears to have close to the optimal thickness. The optimal thickness does vary with operating current density. For comparison purposes in these plots, j_{mo} is held at the same value for the three operating current densities. If the feed methanol concentration were held constant, J_{mo} would drop at higher current because of greater consumption in the anode.

We have been examining optimization of the DMFC by adjusting direct tradeoff of membrane resistance for reduced crossover flux. We will next look at intercepting some of this flux to remove or recycle it.

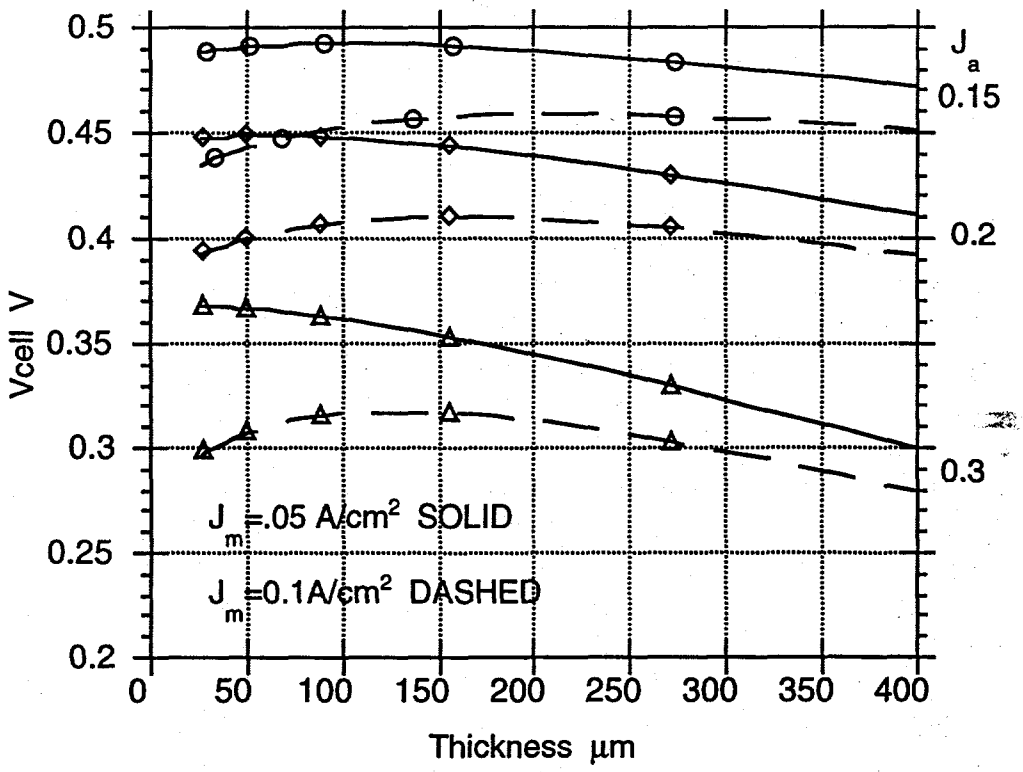

Fig. 6. Cell voltage variation with membrane thickness.

ANALYSIS OF TUBULATED MEMBRANES FOR DMFCs

Direct methanol fuel cells for transportation applications require low catalyst loading to be economically feasible. If the methanol fuel is not totally consumed in the anode, some will cross to the cathode by diffusion and electroosmotic drag. Unless we have extremely high cathode catalyst loading, this will result in an increase in cathode overpotential. If water can be introduced into the membrane between anode and cathode, the amount of methanol reaching the cathode will be decreased but the amount leaving the anode may be increased. We will analyze such a scheme to determine its feasibility to improve performance in a practical and economic manner. During the analysis several needed design features will become obvious and are discussed briefly now.

In the first place to maximize the flux of MeOH diverted from the cathode to the tube, the MeOH concentration in the tube will have to remain low so the flux from the tube to the cathode is small compared to what it would be if there were no flow in the tubes but perfect mixing over the tube cross section was maintained. This would require an infinitely large fluid flow through the tube for the exit concentration to approach zero. For a given flow through circular tubes the pressure drop-inverse fourth power of tube radius relation strongly suggests large diameters. And if the tube shape is elliptical, the pressure drop is much higher, strongly suggesting maintaining circular cross sections. Because we would like to keep the tube flow low while maintaining a low exit concentration, we would like to minimize any additional methanol drawn from the anode by the presence of the tube. One

potential way of doing this is to block the side of the tubes closest to the anode to permeation by water and methanol, forcing the methanol to be diverted from the cathode without increasing the overall flux from the anode. At this time we shall ignore electroosmotic drag because the diffusion calculation can be performed using existing Laplace equation solver codes. When the flux from a 1 M methanol solution diffusing across the membrane is equivalent to the cell current density, the electroosmotic driving force along the protonic path is about 13% in magnitude of the diffusion driving force. In crossover experiments previously done by Ming Ren, where the methanol is oxidized on the cathode, the methanol flux and cell current were locked together and this 13% contribution by drag would hold all the time, but in the DFMC operation, the cell current and crossover flux are not tied together and the drag driving force contribution can become much larger. But because we would have to develop a two dimensional code to solve the combined diffusion and convection flow we chose to do the initial studies ignoring drag. By ignoring drag forces at this time, we get a more optimistic picture and if we still conclude that the advantages of increased cell performance do not warrant the added complexity, redoing the solution to include convection will not be necessary.

Tubulated Membranes

Lynntech, Inc. of College Station, Texas has developed several tubulated Nafion membranes for the purpose of hydrating the membrane in normal hydrogen-air fuel cells to prevent drying on the anode side and consequent increase in membrane ionic resistance. One such membrane is formed by hot pressing together two membranes such as Nafion 115 on each side of an array of parallel wires (typically 200 μm diameter spaced 500 μm apart). After rehydrating the membrane, the wires may be removed. The electrodes should be hot pressed to the membrane before the wires are removed. An optical micrograph of the cross section of a Lynntech membrane/electrode assembly as it appeared in a NASA Conference publication[13] is shown in Fig. 7. The black regions are the electrodes pressed on two 5 mil Nafion 115 membranes. The hole-forming wires and resulting tubes were pressed into an elliptical shape with major diameter 500 μm and minor diameter 250 μm, and the membrane-electrode interface is not flat but curves unevenly around the elliptical holes maintaining a thickness between 75 and 100 μm, as opposed to the 125 μm half thickness in the region away from the holes. The effect of non flat interfaces and elliptical rather than circular holes will be be analyzed, as it appears possible to fabricate them either way by use of higher temperatures with the TBA (tetrabutyl ammonium) substitution in the membrane during the forming process.

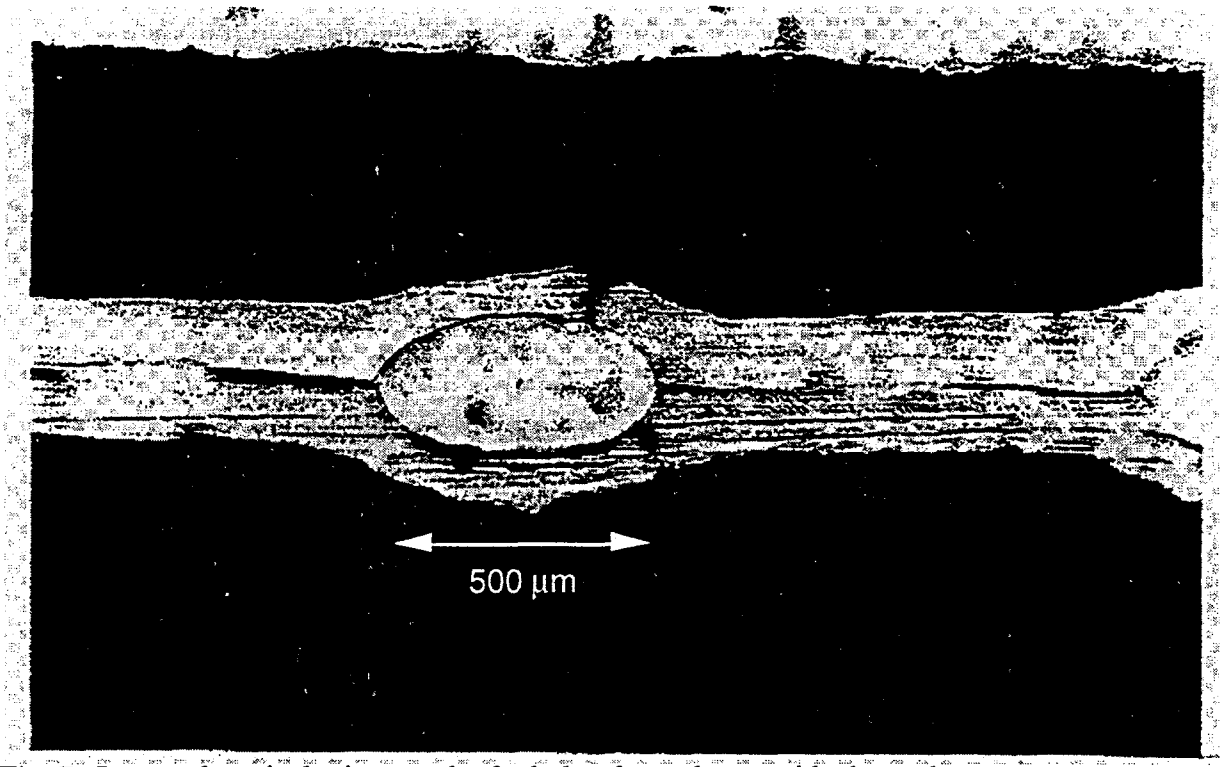

Fig. 7. Lynntech optical micrograph of tubulated membrane with electrodes.

Figure 8 is a cartoon showing the fluxes or flows of MeOH and H_2O in a tubulated DMFC. In the *Laplace Equation Calculations* section we will determine the integrated MeOH flux to the tubes and to the cathode. This flux is primarily driven by diffusion and secondarily by electroosmotic drag, which we ignore at present. While the cartoon shows circular tubes and plane anode and cathode interfaces, these may respectively be elliptical and curved. Consider for now in a cross sectional plane at a fixed value of y only diffusion transport of MeOH between the three source/sink boundaries of anode, tube, and cathode corresponding to subscripts a, t, or c. We assume the concentration across the tube radius at a given y is uniform even though the fluid flow itself is laminar. Earlier we considered one dimensional flow through the membrane or backing and related a uniform flux to the product of a permeability or superficial velocity k (cm/s) and a concentration difference between the two ends of the membrane or backing. This k had a single subscript representing the medium (b or m). Now we have two dimensional flow in the h-z directions and more than two boundaries to the medium. We now relate integral flow per unit length F_{ij} from boundary i to j rather than a non uniform flux to the product of a flow coefficient K_{ij} (cm^2/s) times the concentration difference between boundaries i and j. If C_a is the MeOH concentration at the anode/membrane interface, C_t (y) the concentration in the tube at position y and at the cathode, C_c, is zero, then

$$F_{at} = K_{at}(C_a - C_t);\ F_{tc} = K_{at}C_t;\ F_{at} = K_{ac}C_a \qquad [28]$$

If the tubes were eliminated in Fig. 8, then only remaining coefficient K_{ac} which we will call K_D or base transport coefficient would be

$$K_D = \frac{D_{MeOH} h}{\tau} = k_m h \qquad [29]$$

where D_{MeOH} is the MeOH diffusion coefficient in the membrane and h and τ are the height and thickness of the membrane. With the tubes present a two dimensional solution of the Laplace equation is needed to determine the diffusional transport coefficients.

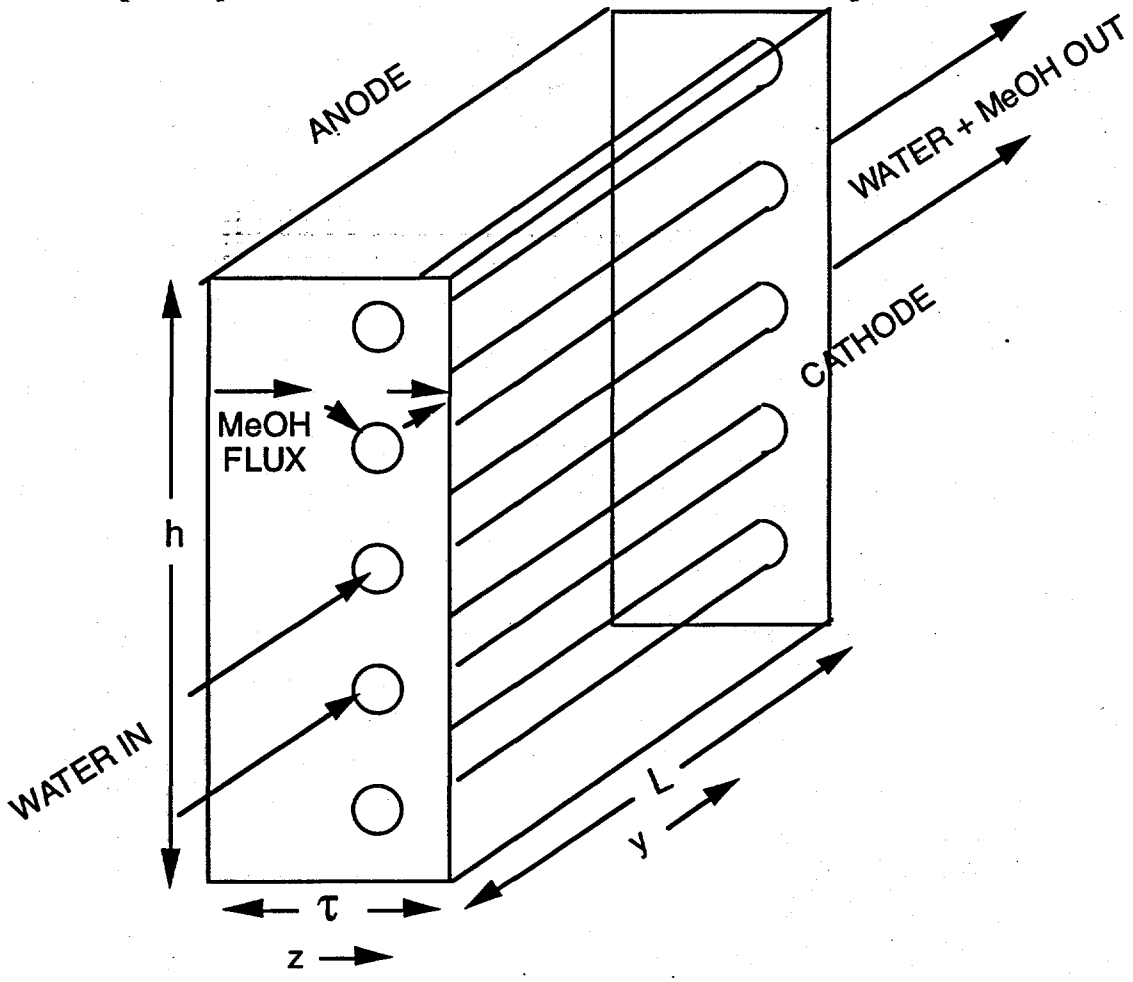

Fig. 8. Cartoon of tubulated membrane.

Laplace Equation Calculations

With the membrane fully in contact with liquid water and methanol, we assume the methanol flux N moves through a fixed water and membrane medium and is described by Fickian diffusion. $N = -D_{MeOH} \nabla C$. One argument for the fixed water-membrane medium is the observation that the membrane takes up additional MeOH without a corresponding decrease in water uptake as the external MeOH concentration is increased.[14] For steady state conditions in which the divergence of the methanol flux is zero, the concentration satisfies the Laplace equation $\nabla^2 C = 0$ and the boundary conditions are C_a, C_t and C_c. To simplify accounting for the membrane partition coefficient, concentrations refer to that of a methanol solution in equilibrium with the membrane, and the diffusion coefficient is appropriate for this definition. To compute the diffusion transport coefficients, we used Green's boundary integral method to solve the two

dimensional LaPlace Equation[15]. Green's formula relates the potential u inside and on the boundary S of a region satisfying the Laplace equation for the two-dimensional Cartesian coordinate system by:

$$u(x,y)=\frac{1}{2\pi}\int_s\left[\ln\frac{1}{\sqrt{x^2+y^2}}\frac{\partial u}{\partial n}-u\frac{\partial}{\partial n}\ln\frac{1}{\sqrt{x^2+y^2}}\right]dS \qquad [30]$$

Along the boundaries, which are discretized into a series of n_p points, the potential u, its normal derivative $\partial u / \partial n$, or a linear combination of both must be specified. Additionally Green's formula provides an additional equation for each boundary point relating its potential to a linear combination of the potential and normal derivative at all points. The coefficients in these equations are calculated from the boundary geometry. There are 2 n_p equations from which the unknown values of u or $\partial u / \partial n$, at each point can be calculated. For interior regions the potential may then be calculated anywhere inside the boundary. The standard program treats boundaries composed of straight lines, circular arcs and circles. To handle elliptical shaped tubes, we added a special semi-elliptical arc boundary, which required defining as a function of arc length t and position coordinates x and y of the ellipse, the following:

$$x(t),\ y(t),\ \frac{dx(t)}{dt},\ \frac{dy(t)}{dt},\ \frac{1}{2}\left[\frac{dx(t)}{dt}\frac{d^2y(t)}{dt^2}-\frac{dy(t)}{dt}\frac{d^2x(t)}{dt^2}\right]. \qquad [31]$$

Figure 9a and 9b shows the geometries for a typical calculations. The tube boundary of a membrane cross section may be elliptical or circular, the anode and cathode boundaries may be either straight or curve with two reversing circular arcs maintaining approximately constant membrane thickness around the tube. Figure 9a represents the present Lynntech geometry of Fig. 7 in which b/a = 2. For the MeOH flux u represents the concentration C. The boundary conditions along the symmetry lines are $\partial u / \partial n = 0$; along the elliptical tube boundary either $u=C_t$ without any impermeable part of the tube wall, or $\partial u / \partial n = 0$ on part of the tube wall and $u=C_t$ along the rest; along the cathode $u=C_c=0.$; and along the anode $u=C_a$. Figure 9b shows another geometry with straight, parallel electrodes and a more circular tube. We believe the latter geometry will perform better and is achievable with proper fabrication methods, so both geometries are investigated.

Figure 10 shows equally spaced contours of concentration on the left and potential on the right for the Lynntech geometry when the methanol concentration in the tube is zero. This is the case when we compute the transport coefficients (see Eq. 34 and 35). Figure 11 shows selected contours for the flat edge, circular tube geometry when the front half of the tube wall is both impermeable and permeable. The impermeable front wall reduces the methanol entering the tube while still diverting flow from reaching the cathode.

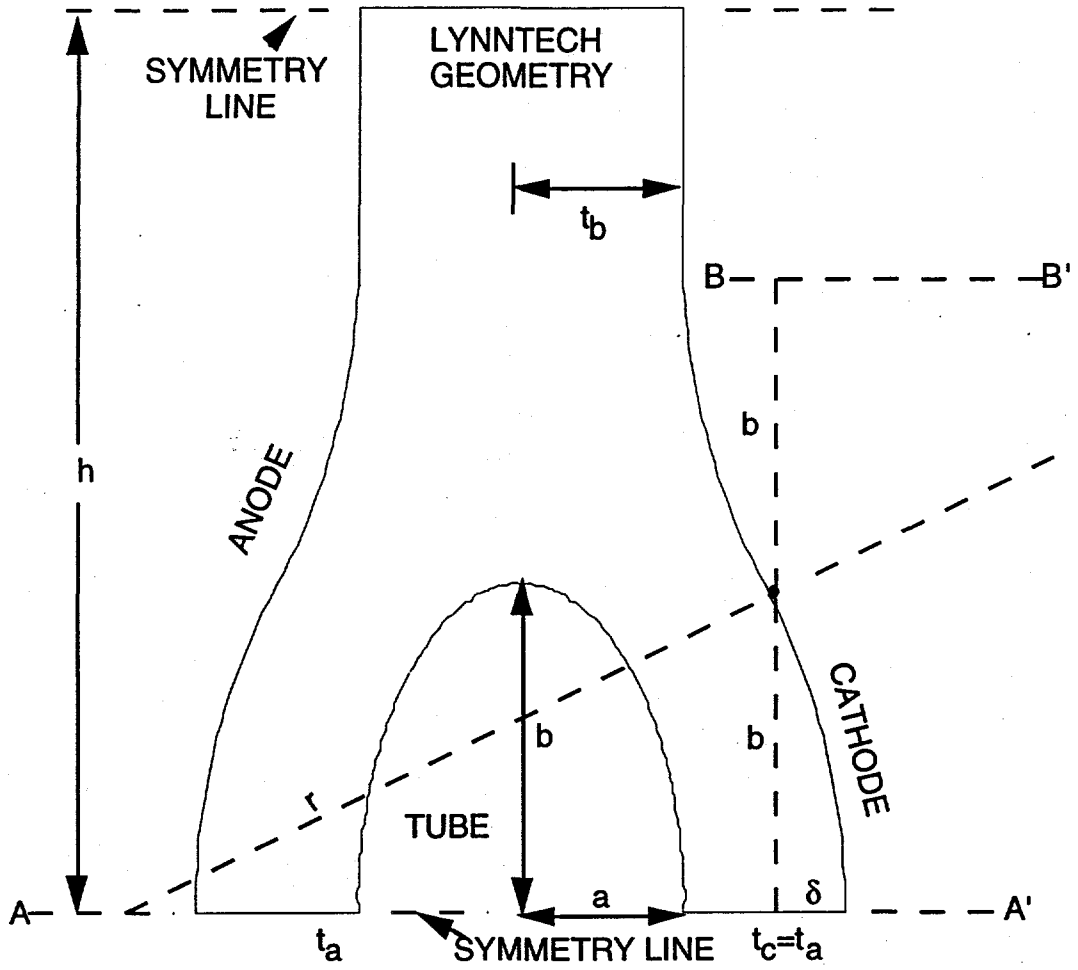

Fig. 9a. Lynntech geometry showng nomenclature.

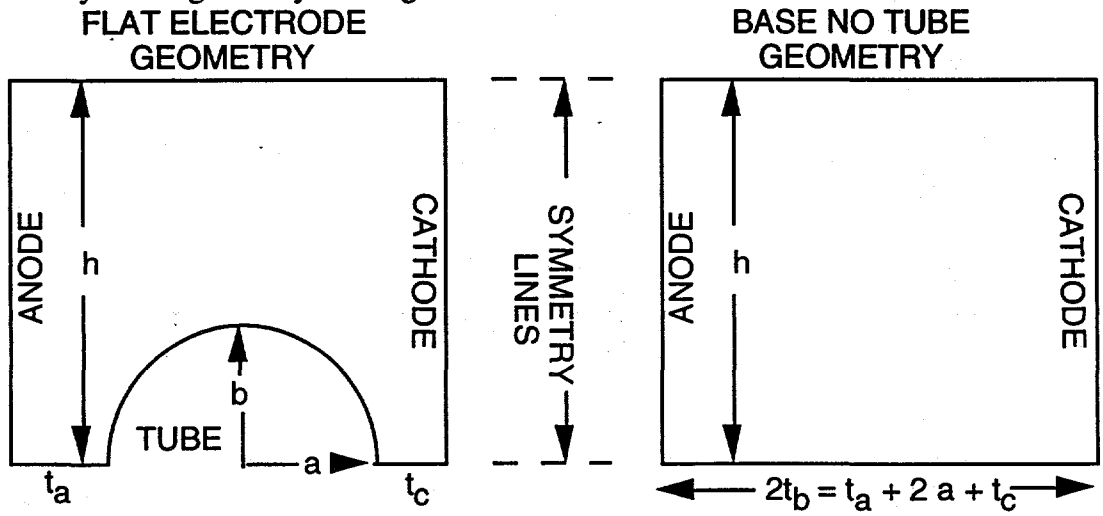

Fig. 9b. Flat membrane and nomenclature with and without tube.

While using the tubes will lower the MeOH flow to the cathode, it will also raise the ionic resistance of the membrane by constricting the proton flow. This resistance can also be calculated using the same geometry but changing the boundary conditions. For ionic

resistance we let u represent the membrane potential. The symmetry line boundary conditions are the same as before, but the tube boundary becomes $\partial u / \partial n = 0$ on both penetrable and impenetrable sections because no protonic current can cross it.

For both methanol and proton flow problems, the calculation needed is the total flow per unit length across the sections of the boundary S_i where the potential was specified, i.e.

$$\frac{\text{MeOH flow}}{\text{unit length}} = D\int_{S_i}\frac{\partial C}{\partial n}dS; \quad \frac{\text{H}^+ \text{ flow}}{\text{unit length}} = \sigma\int_{S_i}\frac{\partial V}{\partial n}dS. \qquad [32]$$

The code computes $\int_{S_i}\partial u / \partial n\, dS$. Because we will compare performance to that of a similar membrane in thickness and transport properties without the tube, we do not in general need to know D or σ for the comparison, only to get performance numbers for a specific configuration.

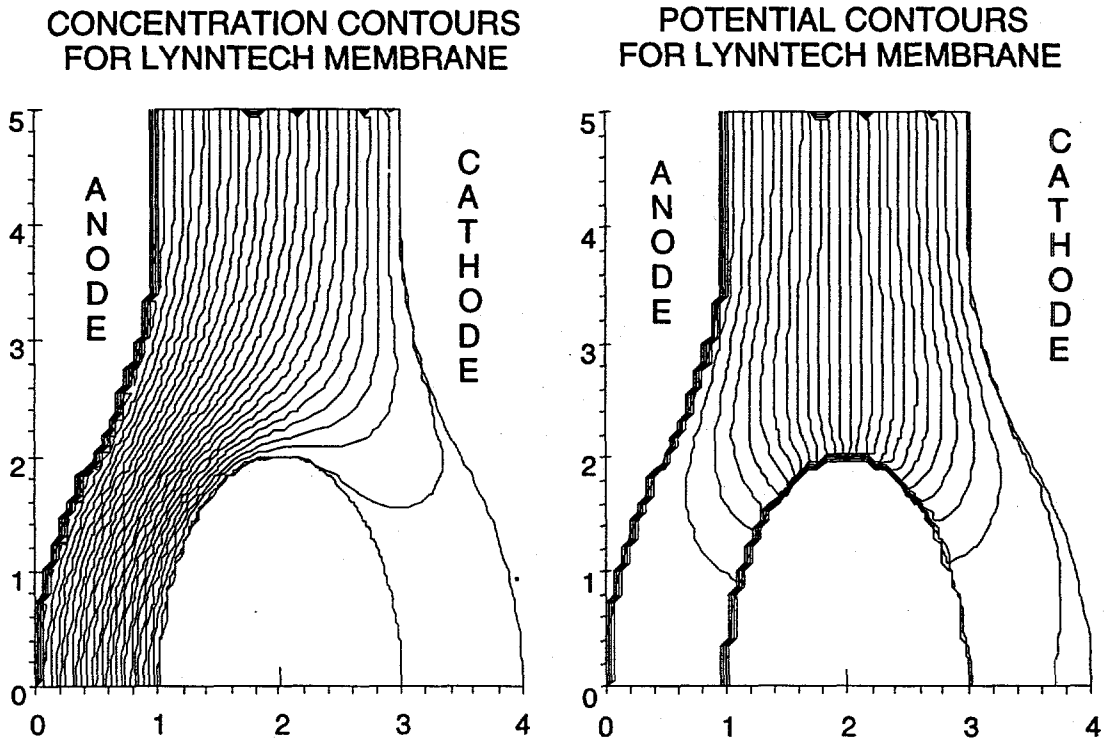

Fig. 10. Methanol concentration and proton potential contours in Lynntech geometry with zero concentration in tubes.

The Fig. 9a cathode shape is constructed of two similar arcs of circles whose centers lie on the lines AA' and BB' and which meet at the point indicated at vertical height b and horizontal position half way between the cathode intersections of the top and bottom symmetry lines (distance δ from the leftmost cathode position). The radius can now be determined.

$$r^2 = (r-\delta)^2 + b^2; \quad r = \frac{\delta^2 + b^2}{2\delta}; \quad \delta = \frac{a + t_c - t_b}{2} \qquad [33]$$

The concentration along the exposed tube boundary will increase with distance y. However, because the diffusion equations is linear, we only need make two calculations of

the Laplace equation for the methanol flow and one for the proton flow. Let I_i be the normalized integrated MeOH flux per unit length along the y direction leaving boundary i, where i is a, t, or c for anode, tube, or cathode. This is the actual integrated flux per unit length divided by the base integrated flux $K_D C_a = (D_{MeOH}\, h/\tau) C_a$ crossing a similar membrane without tubes. Since I_i is linear and since C_c is always zero, we can express the normalized integrated flux leaving the three boundaries as a function of C_a and C_t and can exactly express them by the linear terms of a Taylor series expanded about zero concentration.

$$I_i(C_a, C_t) = \left.\frac{\partial I_i}{\partial C_a}\right|_{C_t} C_a + \left.\frac{\partial I_i}{\partial C_t}\right|_{C_a} C_t = I_i(1,0)C_a + I_i(0,1)C_t \qquad [34]$$

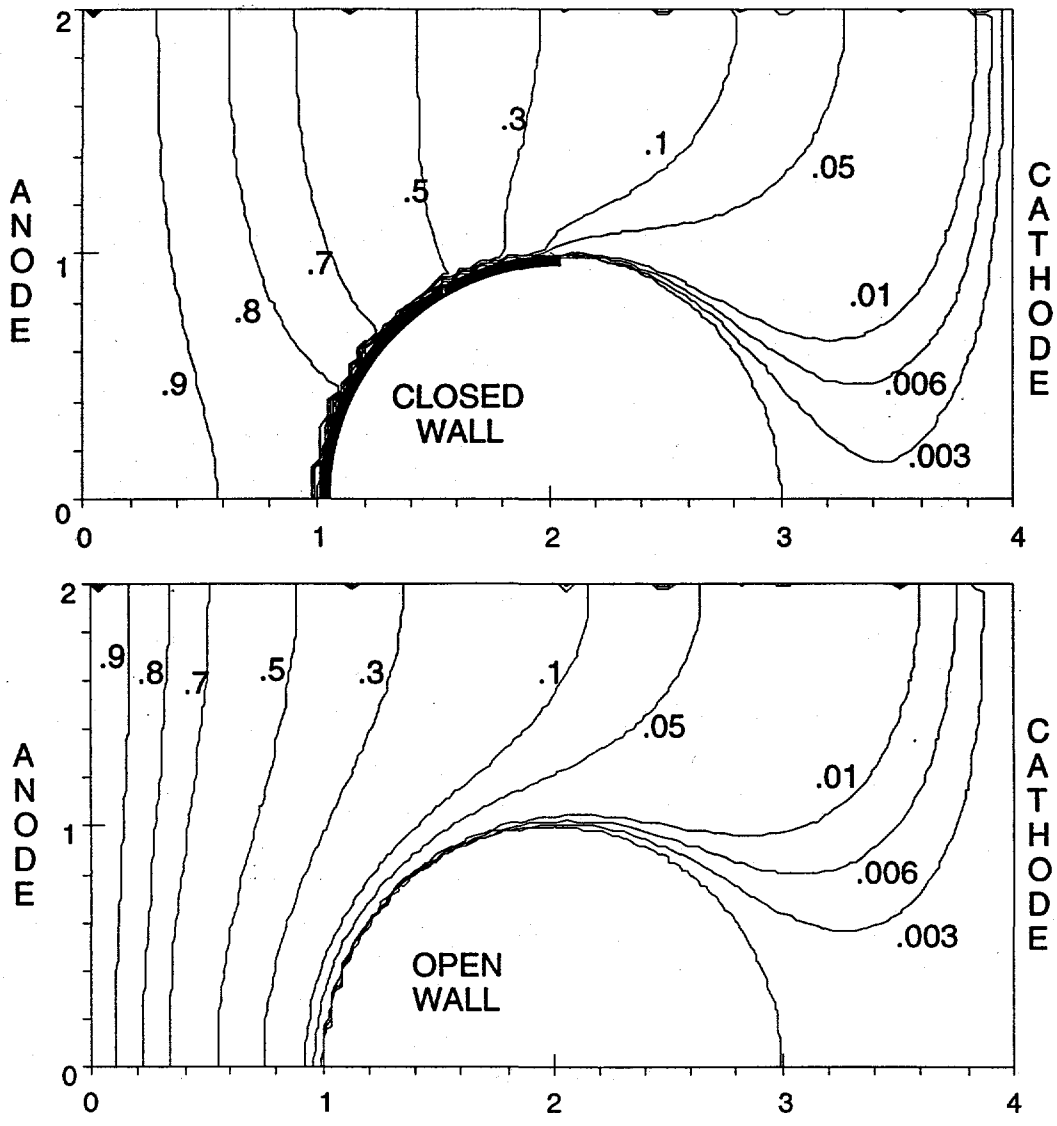

Fig. 11. Methanol concentration contours for flat edge, circular tubes with closed and open front wall facing anode with zero concentration in tube.

The partial derivatives in Eq. 7 are determined by evaluating I_i at one unit of concentration on the anode and zero on the tube, and then one on the tube and zero on the anode, so only two solutions of the Laplace equation are needed. In keeping with Eq. 28, we want to determine three normalized transport coefficients R_{ac}, R_{at}, and R_{tc}.

$$R_{ac} = \frac{K_{ac}}{K_D} = -I_c(1,0);\ R_{at} = \frac{K_{at}}{K_D} = -I_t(1,0);\ R_{tc} = \frac{K_{tc}}{K_D} = -I_c(0,1) \qquad [35]$$

The partial derivatives are not independent of each other. From symmetry,

$$I_a(0,1) = I_t(1,0). \qquad [36]$$

Because the sum of the integrated fluxes to the three boundaries must be zero:

$$I_t(0,1) = -I_c(0,1) - I_a(0,1) = R_{tc} + R_{at} \qquad [37]$$

Using Eq. 36 and 37, Eq. 38 becomes for the tube boundary:

$$I_t(C_a, C_t) = -R_{at}C_a + (R_{tc} + R_{at})C_t = R_{tc}C_t - R_{at}(C_a - C_t) \qquad [38]$$

which expresses the net integrated flux leaving the tube wall is that going to the cathode less that coming into the wall from the anode.

Tube Flow

We have just showed how to determine the methanol flux to the tube and the cathode using the concentration at the anode. However, we actually know the feed concentration C_F and need to eliminate C_a for the tube case as was done in Eq. 22 to 24 for the plane membrane case. We are ignoring electroosmotic drag. We assume uniform, one dimensional diffusion in the height direction h through the backing so C_a will be constant, as was assumed in the Laplace equation calculations. Just as K_D ($=k_m h$) was introduced because of the non uniformity in the h direction, so K_B ($=k_b h$) is introduced for the backing. C_a can still vary along the y direction if the tube methanol concentration C_t varies.

$$C_a = \frac{C_f K_B + C_t(y) K_D R_{at} - j_a / 6F}{K_B + K_D(R_{ac} + R_{at})} \qquad [39]$$

If Q is the volume flow rate (cm^3/s) of fluid in the tubes moving in the y direction, the rate of increase in MeOH concentration is

$$\frac{dC_t}{dy} = \frac{-I_t(C_a, C_t)K_D}{Q} = \frac{R_{at}C_a - (R_{at} + R_{tc})C_t(y)}{Q / K_D};\ C_t(0) = 0 \qquad [39]$$

The exact solution of Eq. 39 for the concentration at any position y in terms of C_f is

$$C_t(y) = \frac{R_{at}\left(C_f K_B - j_a\right)}{K_2}\left[1 - \exp\left(-\frac{K_2 K_D y}{K_1 Q}\right)\right], \text{ where} \qquad [40]$$

$$K_1 = K_B + (R_{ac} + R_{at})K_D,\ K_2 = K_B(R_{tc} + R_{at}) + K_D(R_{at}R_{tc} + R_{ac}R_{at} + R_{ac}R_{tc})$$

and the average concentration, which will give the same flow into and out of the tube wall is

$$C_{ave} = \frac{R_{at}(C_f K_B - j_a / 6F)}{K_2}\left(1 - \frac{K_1 Q}{K_2 K_D L}\left(1 - \exp\left[-\frac{K_2 K_D L}{K_1 Q}\right]\right)\right). \qquad [41]$$

The methanol flow to the cathode, F_{cath} is

$$F_{cath} = \int_0^L \left(R_{ac}C_a(y) + R_{tc}C_t(y)\right)K_D dy =$$

$$\frac{LK_D\left(C_f K_B - j_a/6F\right)}{K_1}\left\{R_{ac} + R_{at}\left(1 - R_{at}\frac{K_B}{K_2}\right)\left(1 - \left[1 - \exp(-\frac{K_2K_DL}{K_1Q})\right]\frac{K_1Q}{K_2K_DL}\right)\right\} \quad [42]$$

To reduce the average concentration to zero would require an infinite water flow Q , so a meaningful flow is the one that would halve the average concentration that exists with no flow. When Q approaches 0, Eq. 41 becomes $C_{ave} = R_{at}(C_f K_B - j_a/6F)/K_2$. When $C_{ave} = R_{at}(C_f K_B - j_a/6F)/(2K_2)$, then $Q_{1/2}$ satisfies the equation

$$\exp\left[-\frac{K_2K_DL}{K_1Q_{1/2}}\right] = 1 - \frac{1}{2}\frac{K_2K_DL}{K_1Q_{1/2}} \quad \text{or} \quad Q_{1/2} = \frac{K_2K_DL}{1.59362K_1}. \quad [43]$$

and at this fluid flow rate the exit concentration is $0.796881R_{at}\left(C_f K_B - j_a\right)/K_2$.

We shall always use a unit height h of 1 cm for the flow Q and the transport coefficients K. Using from Ming 0.9 A/cm^2 and 0.15 A/cm^2 at 1 M MeOH for the limiting current observed with total electrooxidation on the anode and cathode respectively, we get $hk_b = K_B =$ 0.00155 cm^2/s and $hk_m = K_D =$0.00031 cm^2/s.

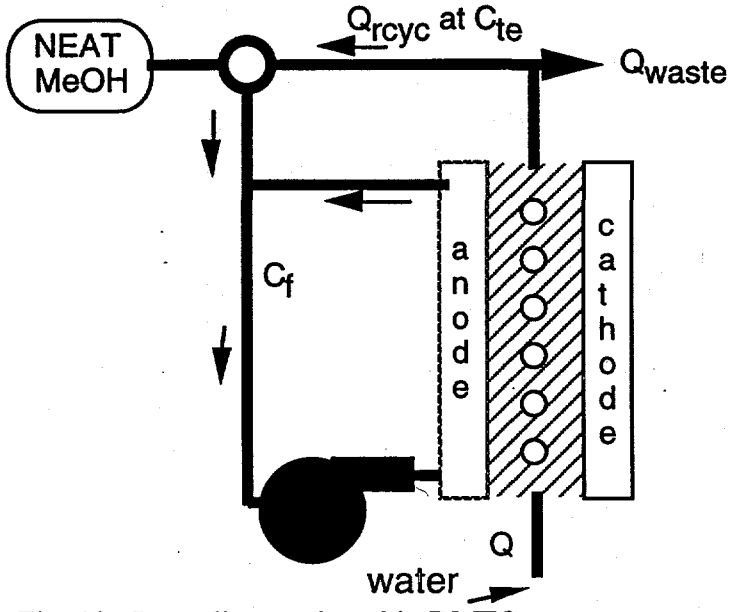

Fig. 12. Recycling methanol in DMFC

Recycling and Fuel Efficiency

Figure 12 shows a method of recycling the methanol removed from the membrane. If the tube exit flow Q at a concentration of C_{te} is mixed with neat methanol to obtain a concentration C_f, the flow that can be completely recycled will be

$$Q_{rcycl} = \frac{L(j_a + j_m)/(6F)}{C_f(1 - x_{MeOHte})}. \quad [44]$$

Basically the recycled water flows at a rate that can make the consumed feed solution at concentration C_f (1 M for our examples). Any excess flow Q_{waste} is discarded. The tube exit methanol mole fraction x_{MeOHte} is usually much less than 1%. Q_{rcyc} is the flow that will just carry the methanol that is oxidized in the anode and the cathode. The fuel efficiency is given by

$$\text{Fuel Efficiency} = 1 - \frac{F_{cath} + (Q - Q_{rcyc})C_{te}/L}{F_{cath} + (Q - Q_{rcyc})C_{te}/L + J_a/(6\text{F})}. \qquad [45]$$

Performance with Tubulated Membranes

We are now in a position to see the effect on the cell voltage, the fuel efficiency, and their product if tubulated membranes were used in a DMFC. When operating at a fixed current density, the voltage-efficiency product is a direct measure of the amount of work that can be obtained from a fixed quantity of methanol. We have seen how to determine the anode and cathode potentials and cell voltage when methanol crossover and membrane resistance is known. When we ignore electroosmotic drag, we have seen how to determine the methanol flux to cathode and tubes using the Laplace solver and how the concentration buildup and cathode flux is affected by water flow through the tubes. Tables II and III show results of the model for several different tubulated designs, for two different current densities, 0.15 and 0.3 A/cm^2, without recycling at no flow and with the recycle flow discarded, with recycling at just the recycle flow and then at 5 times the recycle flow (discarding 80%). With each current density is a base or non tubulated case which has 0.17 Ω cm^2 for R_{mem} and crossover flux all going to the cathode. The membrane resistance is increased by the factor R_{res} for the other cases. The cathode for Table II has a low loading ($A_r i^* = 0.1$ A/cm^2 and Table III has a heavy loading ($A_r i^* = 1.$). Cathode, backing and membrane parameters are listed at the beginning of each table. At the top of each tubulated design case is listed the normalized transport coefficients R_{ac}, R_{at}, and R_{tc} plus the resistance increase factor R_{res} calculated. The next line describes the membrane geometry.

The first case is the Lynntech design, which has elliptical tubes and wavy edges (see Fig. 9a). The rest of the cases are described by Fig.9b, which shows t_a, a, and t_c. These designs all have circles. Theta, representing the half arc angle in degrees from the anode side of the tube wall that is made impermeable to flow. It is either 5° or 90°. The former is essentially no covering (cannot use 0 without switching codes), the latter covers the semicircular wall toward the anode. The first half of the cases in each table have 1 unit thickness to the tube which has a 1 unit radius; the second half have 0.5 unit thickness to the same radius tube. The halfwidth between circles, h, is 2 units and 3 units. R_{at} and R_{tc} are increased with the thinner walls and R_{ac} is increased when h is increased.

The water flows Q and Q_{rcyc} have been scaled to the flow in ml/min for an L= 5 cm by h= 5 cm cell. The tube diameter, only needed for the pressure drop calculation, is 0.01 cm. The transport coefficients R are only functions of the proportional geometric shape. The flux reaching the cathode, F_{cath}, is in A/cm^2 as is J_{an} the anode current density, and the exit tube concentration C_{te} is in mol/li. The column labeled rcyl lists the base, no tube case or whether the tube flow is recycled. The no flow case will let the exit concentration exist

throughout the tube. F_{cath} drops more than C_{te} when flow is on because the average concentration, not shown, drops more than C_{te}. The reader must study the results.

Some points to be noted are that the total efficiency (Vc*feff) is always highest at the recycle flow. For the thin walled cases (ta=tc=0.5) the base case is sometimes better. The impermeable wall coating (θ=90°) always improves the performance and drops the flow required to completely recycle. The best increase (25%) in total efficiency from base case of 0.294 to 0.368 occurs in the third design of Table III (ta,a,tc,theta,hite 1 1 1 90 2). This same membrane without the coating had a total efficiency of 0.293, less than the base case. The best improvement using the current Lynntech geometry was 6.1%.

TABLE II. Tubulated Membrane Analysis for Low Loading Cathode.

A_i^*	I_D	b_c	R_{cl}	pres	xon	I_B
0.100	0.900	0.033	0.100	1.000	0.210	2.500

°C	Rmem	K_B	K_D	C_f	L	diam
80.	0.17	0.0015	0.0007	1.0	5.0	0.01

Rac Rat Rtc Rres= 0.465 1.079 2.156 1.600

Lynntech

rcyl	Q	Jan	Vcell	f eff	Vc*feff	Fcath	Cte	Qrcyc	dpsi
base		0.150	0.462	0.546	0.253	0.125			
no	0.001	0.150	0.437	0.512	0.224	0.143	0.225	0.663	0.000
no	0.663	0.150	0.457	0.489	0.224	0.106	0.198	0.663	0.059
yes	0.663	0.150	0.457	0.586	0.268	0.106	0.198	0.663	0.059
yes	3.316	0.150	0.477	0.500	0.239	0.070	0.078	0.663	0.294
base		0.300	0.342	0.751	0.256	0.100			
no	0.001	0.300	0.301	0.724	0.218	0.114	0.180	0.975	0.000
no	0.975	0.300	0.325	0.700	0.228	0.076	0.138	0.975	0.086
yes	0.975	0.300	0.325	0.797	0.259	0.076	0.138	0.975	0.086
yes	4.877	0.300	0.340	0.714	0.243	0.052	0.045	0.975	0.432

Rac Rat Rtc Rres= 0.051 2.857 2.875 1.489

ta,a,tc,theta,hite 1 1 1 5 2

rcyl	Q	Jan	Vcell	f eff	Vc*feff	Fcath	Cte	Qrcyc	dpsi
base		0.150	0.462	0.546	0.253	0.125			
no	0.001	0.150	0.424	0.467	0.198	0.171	0.320	0.700	0.000
no	0.700	0.150	0.452	0.425	0.192	0.120	0.306	0.700	0.062
yes	0.700	0.150	0.452	0.555	0.251	0.120	0.306	0.700	0.062
yes	3.500	0.150	0.493	0.419	0.207	0.047	0.149	0.700	0.310
base		0.300	0.342	0.751	0.256	0.100			
no	0.001	0.300	0.291	0.687	0.200	0.137	0.256	0.993	0.000
no	0.993	0.300	0.327	0.638	0.209	0.083	0.228	0.993	0.088
yes	0.993	0.300	0.327	0.783	0.256	0.083	0.228	0.993	0.088
yes	4.963	0.300	0.359	0.640	0.229	0.029	0.091	0.993	0.439

Rac Rat Rtc Rres= 0.132 0.909 2.785 1.489

ta,a,tc,theta,hite 1 1 1 90 2

rcyl	Q	Jan	Vcell	f eff	Vc*feff	Fcath	Cte	Qrcyc	dpsi
base		0.150	0.462	0.546	0.253	0.125			
no	0.001	0.150	0.461	0.588	0.271	0.105	0.176	0.584	0.000
no	0.584	0.150	0.477	0.571	0.272	0.076	0.166	0.584	0.052
yes	0.584	0.150	0.477	0.665	0.317	0.076	0.166	0.584	0.052
yes	2.922	0.150	0.499	0.586	0.292	0.037	0.076	0.584	0.259
base		0.300	0.342	0.751	0.256	0.100			
no	0.001	0.300	0.327	0.781	0.255	0.084	0.141	0.910	0.000
no	0.910	0.300	0.346	0.764	0.264	0.051	0.118	0.910	0.081
yes	0.910	0.300	0.346	0.854	0.296	0.051	0.118	0.910	0.081
yes	4.551	0.300	0.361	0.780	0.282	0.025	0.043	0.910	0.403

Rac Rat Rtc Rres= 0.242 2.163 2.175 1.278
ta,a,tc,theta,hite 1 1 1 5 3

rcyl	Q	Jan	Vcell	f eff	Vc*feff	Fcath	Cte	Qrcyc	dpsi
base		0.150	0.462	0.546	0.253	0.125			
no	0.001	0.150	0.438	0.489	0.214	0.157	0.328	0.671	0.000
no	0.671	0.150	0.464	0.444	0.206	0.109	0.303	0.671	0.059
yes	0.671	0.150	0.464	0.579	0.268	0.109	0.303	0.671	0.059
yes	3.357	0.150	0.495	0.441	0.219	0.053	0.132	0.671	0.297
base		0.300	0.342	0.751	0.256	0.100			
no	0.001	0.300	0.310	0.705	0.219	0.125	0.262	0.973	0.000
no	0.973	0.300	0.342	0.656	0.225	0.076	0.218	0.973	0.086
yes	0.973	0.300	0.342	0.799	0.273	0.076	0.218	0.973	0.086
yes	4.867	0.300	0.366	0.661	0.242	0.036	0.078	0.973	0.431

Rac Rat Rtc Rres= 0.353 0.715 2.044 1.278
ta,a,tc,theta,hite 1 1 1 90 3

rcyl	Q	Jan	Vcell	f eff	Vc*feff	Fcath	Cte	Qrcyc	dpsi
base		0.150	0.462	0.546	0.253	0.125			
no	0.001	0.150	0.462	0.572	0.264	0.112	0.183	0.604	0.000
no	0.604	0.150	0.478	0.555	0.265	0.083	0.160	0.604	0.053
yes	0.604	0.150	0.478	0.644	0.308	0.083	0.160	0.604	0.053
yes	3.019	0.150	0.494	0.569	0.281	0.056	0.062	0.604	0.267
base		0.300	0.342	0.751	0.256	0.100			
no	0.001	0.300	0.334	0.770	0.257	0.090	0.147	0.931	0.000
no	0.931	0.300	0.352	0.753	0.265	0.059	0.108	0.931	0.082
yes	0.931	0.300	0.352	0.835	0.294	0.059	0.108	0.931	0.082
yes	4.655	0.300	0.363	0.768	0.278	0.041	0.034	0.931	0.412

Rac Rat Rtc Rres= 0.083 3.442 3.486 1.625
ta,a,tc,theta,hite .5 1 .5 5 2

rcyl	Q	Jan	Vcell	f eff	Vc*feff	Fcath	Cte	Qrcyc	dpsi
base		0.150	0.462	0.546	0.253	0.125			
no	0.001	0.150	0.405	0.430	0.174	0.199	0.304	0.762	0.000
no	0.762	0.150	0.436	0.394	0.172	0.144	0.293	0.762	0.067
yes	0.762	0.150	0.436	0.510	0.222	0.144	0.293	0.762	0.067
yes	3.811	0.150	0.483	0.390	0.188	0.060	0.149	0.762	0.337
base		0.300	0.342	0.751	0.256	0.100			
no	0.001	0.300	0.267	0.653	0.174	0.159	0.243	1.042	0.000
no	1.042	0.300	0.308	0.610	0.188	0.102	0.222	1.042	0.092
yes	1.042	0.300	0.308	0.746	0.230	0.102	0.222	1.042	0.092
yes	5.212	0.300	0.347	0.612	0.212	0.038	0.095	1.042	0.461

Rac Rat Rtc Rres= 0.170 0.743 3.387 1.625
ta,a,tc,theta,hite .5 1 .5 90 2

rcyl	Q	Jan	Vcell	f eff	Vc*feff	Fcath	Cte	Qrcyc	dpsi
base		0.150	0.462	0.546	0.253	0.125			
no	0.001	0.150	0.460	0.598	0.275	0.101	0.130	0.588	0.000
no	0.588	0.150	0.473	0.588	0.278	0.077	0.124	0.588	0.052
yes	0.588	0.150	0.473	0.661	0.313	0.077	0.124	0.588	0.052
yes	2.940	0.150	0.493	0.606	0.298	0.042	0.061	0.588	0.260
base		0.300	0.342	0.751	0.256	0.100			
no	0.001	0.300	0.322	0.788	0.254	0.080	0.104	0.916	0.000
no	0.916	0.300	0.338	0.778	0.263	0.054	0.090	0.916	0.081
yes	0.916	0.300	0.338	0.848	0.287	0.054	0.090	0.916	0.081
yes	4.581	0.300	0.352	0.794	0.280	0.029	0.035	0.916	0.405

Rac Rat Rtc Rres= 0.315 2.446 2.475 1.344
ta,a,tc,theta,hite .5 1 .5 5 3

rcyl	Q	Jan	Vcell	f eff	Vc*feff	Fcath	Cte	Qrcyc	dpsi
base		0.150	0.462	0.546	0.253	0.125			
no	0.001	0.150	0.425	0.460	0.195	0.176	0.316	0.715	0.000
no	0.715	0.150	0.453	0.420	0.190	0.126	0.295	0.715	0.063
yes	0.715	0.150	0.453	0.544	0.246	0.126	0.295	0.715	0.063
yes	3.574	0.150	0.488	0.418	0.204	0.063	0.132	0.715	0.316
base		0.300	0.342	0.751	0.256	0.100			
no	0.001	0.300	0.295	0.680	0.201	0.141	0.253	1.008	0.000
no	1.008	0.300	0.331	0.634	0.210	0.089	0.216	1.008	0.089
yes	1.008	0.300	0.331	0.771	0.255	0.089	0.216	1.008	0.089
yes	5.039	0.300	0.358	0.640	0.229	0.044	0.080	1.008	0.446

Rac Rat Rtc Rres= 0.409 0.554 2.364 1.344
ta,a,tc,theta,hite .5 1 .5 90 3

rcyl	Q	Jan	Vcell	f eff	Vc*feff	Fcath	Cte	Qrcyc	dpsi
base		0.150	0.462	0.546	0.253	0.125			
no	0.001	0.150	0.462	0.578	0.267	0.109	0.135	0.611	0.000
no	0.611	0.150	0.475	0.568	0.270	0.086	0.120	0.611	0.054
yes	0.611	0.150	0.475	0.636	0.302	0.086	0.120	0.611	0.054
yes	3.054	0.150	0.488	0.583	0.285	0.062	0.048	0.611	0.270
base		0.300	0.342	0.751	0.256	0.100			
no	0.001	0.300	0.332	0.774	0.257	0.087	0.108	0.940	0.000
no	0.940	0.300	0.347	0.765	0.265	0.063	0.082	0.940	0.083
yes	0.940	0.300	0.347	0.827	0.287	0.063	0.082	0.940	0.083
yes	4.698	0.300	0.356	0.778	0.277	0.047	0.027	0.940	0.416

TABLE III. Tubulated Membrane Analysis for High Loading Cathode.

A_i^*	I_D	b_c	R_{c1}	pres	xon	I_B
1.000	0.900	0.033	0.100	1.000	0.210	2.500

°C	Rmem	K_B	K_D	C_f	L	diam
80.	0.17	0.0015	0.0007	1.0	5.0	0.01

Rac Rat Rtc Rres= 0.465 1.079 2.156 1.600
Lynntech

rcyl	Q	Jan	Vcell	f eff	Vc*feff	Fcath	Cte	Qrcyc	dpsi
base		0.150	0.538	0.546	0.294	0.125			
no	0.001	0.150	0.513	0.512	0.263	0.143	0.225	0.663	0.000
no	0.663	0.150	0.533	0.489	0.261	0.106	0.198	0.663	0.059
yes	0.663	0.150	0.533	0.586	0.312	0.106	0.198	0.663	0.059
yes	3.316	0.150	0.553	0.500	0.277	0.070	0.078	0.663	0.294
base		0.300	0.418	0.751	0.314	0.100			
no	0.001	0.300	0.377	0.724	0.273	0.114	0.180	0.975	0.000
no	0.975	0.300	0.401	0.700	0.281	0.076	0.138	0.975	0.086
yes	0.975	0.300	0.401	0.797	0.320	0.076	0.138	0.975	0.086
yes	4.877	0.300	0.416	0.714	0.297	0.052	0.045	0.975	0.432

Rac Rat Rtc Rres= 0.051 2.857 2.875 1.489
ta,a,tc,theta,hite 1 1 1 5 2

rcyl	Q	Jan	Vcell	f eff	Vc*feff	Fcath	Cte	Qrcyc	dpsi
base		0.150	0.538	0.546	0.294	0.125			
no	0.001	0.150	0.500	0.467	0.234	0.171	0.320	0.700	0.000
no	0.700	0.150	0.528	0.425	0.225	0.120	0.306	0.700	0.062
yes	0.700	0.150	0.528	0.555	0.293	0.120	0.306	0.700	0.062
yes	3.500	0.150	0.569	0.419	0.238	0.047	0.149	0.700	0.310
base		0.300	0.418	0.751	0.314	0.100			
no	0.001	0.300	0.367	0.687	0.252	0.137	0.256	0.993	0.000
no	0.993	0.300	0.403	0.638	0.257	0.083	0.228	0.993	0.088
yes	0.993	0.300	0.403	0.783	0.316	0.083	0.228	0.993	0.088
yes	4.963	0.300	0.435	0.640	0.278	0.029	0.091	0.993	0.439

Rac Rat Rtc Rres= 0.132 0.909 2.785 1.489
ta,a,tc,theta,hite 1 1 1 90 2

rcyl	Q	Jan	Vcell	f eff	Vc*feff	Fcath	Cte	Qrcyc	dpsi
base		0.150	0.538	0.546	0.294	0.125			
no	0.001	0.150	0.537	0.588	0.316	0.105	0.176	0.584	0.000
no	0.584	0.150	0.553	0.571	0.315	0.076	0.166	0.584	0.052
yes	0.584	0.150	0.553	0.665	0.368	0.076	0.166	0.584	0.052
yes	2.922	0.150	0.574	0.586	0.337	0.037	0.076	0.584	0.259
base		0.300	0.418	0.751	0.314	0.100			
no	0.001	0.300	0.402	0.781	0.314	0.084	0.141	0.910	0.000
no	0.910	0.300	0.422	0.764	0.322	0.051	0.118	0.910	0.081
yes	0.910	0.300	0.422	0.854	0.360	0.051	0.118	0.910	0.081
yes	4.551	0.300	0.437	0.780	0.341	0.025	0.043	0.910	0.403

Rac Rat Rtc Rres= 0.242 2.163 2.175 1.278
ta,a,tc,theta,hite 1 1 1 5 3

rcyl	Q	Jan	Vcell	f eff	Vc*feff	Fcath	Cte	Qrcyc	dpsi
base		0.150	0.538	0.546	0.294	0.125			
no	0.001	0.150	0.514	0.489	0.251	0.157	0.328	0.671	0.000
no	0.671	0.150	0.540	0.444	0.240	0.109	0.303	0.671	0.059
yes	0.671	0.150	0.540	0.579	0.312	0.109	0.303	0.671	0.059
yes	3.357	0.150	0.571	0.441	0.252	0.053	0.132	0.671	0.297
base		0.300	0.418	0.751	0.314	0.100			
no	0.001	0.300	0.386	0.705	0.272	0.125	0.262	0.973	0.000
no	0.973	0.300	0.418	0.656	0.274	0.076	0.218	0.973	0.086
yes	0.973	0.300	0.418	0.799	0.334	0.076	0.218	0.973	0.086
yes	4.867	0.300	0.441	0.661	0.292	0.036	0.078	0.973	0.431

Rac Rat Rtc Rres= 0.353 0.715 2.044 1.278
ta,a,tc,theta,hite 1 1 1 90 3

rcyl	Q	Jan	Vcell	f eff	Vc*feff	Fcath	Cte	Qrcyc	dpsi
base		0.150	0.538	0.546	0.294	0.125			
no	0.001	0.150	0.538	0.572	0.308	0.112	0.183	0.604	0.000
no	0.604	0.150	0.554	0.555	0.307	0.083	0.160	0.604	0.053
yes	0.604	0.150	0.554	0.644	0.357	0.083	0.160	0.604	0.053
yes	3.019	0.150	0.569	0.569	0.324	0.056	0.062	0.604	0.267
base		0.300	0.418	0.751	0.314	0.100			
no	0.001	0.300	0.410	0.770	0.315	0.090	0.147	0.931	0.000
no	0.931	0.300	0.428	0.753	0.323	0.059	0.108	0.931	0.082
yes	0.931	0.300	0.428	0.835	0.357	0.059	0.108	0.931	0.082
yes	4.655	0.300	0.438	0.768	0.337	0.041	0.034	0.931	0.412

Rac Rat Rtc Rres= 0.083 3.442 3.486 1.625
ta,a,tc,theta,hite .5 1 .5 5 2

rcyl	Q	Jan	Vcell	f eff	Vc*feff	Fcath	Cte	Qrcyc	dpsi
base		0.150	0.538	0.546	0.294	0.125			
no	0.001	0.150	0.481	0.430	0.207	0.199	0.304	0.762	0.000
no	0.762	0.150	0.512	0.394	0.202	0.144	0.293	0.762	0.067
yes	0.762	0.150	0.512	0.510	0.261	0.144	0.293	0.762	0.067
yes	3.811	0.150	0.558	0.390	0.217	0.060	0.149	0.762	0.337
base		0.300	0.418	0.751	0.314	0.100			
no	0.001	0.300	0.343	0.653	0.224	0.159	0.243	1.042	0.000
no	1.042	0.300	0.384	0.610	0.234	0.102	0.222	1.042	0.092
yes	1.042	0.300	0.384	0.746	0.286	0.102	0.222	1.042	0.092
yes	5.212	0.300	0.423	0.612	0.259	0.038	0.095	1.042	0.461

Rac Rat Rtc Rres= 0.170 0.743 3.387 1.625
ta,a,tc,theta,hite .5 1 .5 90 2

rcyl	Q	Jan	Vcell	f eff	Vc*feff	Fcath	Cte	Qrcyc	dpsi
base		0.150	0.538	0.546	0.294	0.125			
no	0.001	0.150	0.535	0.598	0.320	0.101	0.130	0.588	0.000
no	0.588	0.150	0.549	0.588	0.323	0.077	0.124	0.588	0.052
yes	0.588	0.150	0.549	0.661	0.363	0.077	0.124	0.588	0.052
yes	2.940	0.150	0.568	0.606	0.344	0.042	0.061	0.588	0.260
base		0.300	0.418	0.751	0.314	0.100			
no	0.001	0.300	0.398	0.788	0.313	0.080	0.104	0.916	0.000
no	0.916	0.300	0.414	0.778	0.322	0.054	0.090	0.916	0.081
yes	0.916	0.300	0.414	0.848	0.351	0.054	0.090	0.916	0.081
yes	4.581	0.300	0.428	0.794	0.340	0.029	0.035	0.916	0.405

Rac Rat Rtc Rres= 0.315 2.446 2.475 1.344
ta,a,tc,theta,hite .5 1 .5 5 3

rcyl	Q	Jan	Vcell	f eff	Vc*feff	Fcath	Cte	Qrcyc	dpsi
base		0.150	0.538	0.546	0.294	0.125			
no	0.001	0.150	0.501	0.460	0.230	0.176	0.316	0.715	0.000
no	0.715	0.150	0.529	0.420	0.222	0.126	0.295	0.715	0.063
yes	0.715	0.150	0.529	0.544	0.287	0.126	0.295	0.715	0.063
yes	3.574	0.150	0.563	0.418	0.235	0.063	0.132	0.715	0.316
base		0.300	0.418	0.751	0.314	0.100			
no	0.001	0.300	0.371	0.680	0.253	0.141	0.253	1.008	0.000
no	1.008	0.300	0.407	0.634	0.258	0.089	0.216	1.008	0.089
yes	1.008	0.300	0.407	0.771	0.314	0.089	0.216	1.008	0.089
yes	5.039	0.300	0.434	0.640	0.277	0.044	0.080	1.008	0.446

Rac Rat Rtc Rres= 0.409 0.554 2.364 1.344
ta,a,tc,theta,hite .5 1 .5 90 3

rcyl	Q	Jan	Vcell	f eff	Vc*feff	Fcath	Cte	Qrcyc	dpsi
base		0.150	0.538	0.546	0.294	0.125			
no	0.001	0.150	0.538	0.578	0.311	0.109	0.135	0.611	0.000
no	0.611	0.150	0.551	0.568	0.313	0.086	0.120	0.611	0.054
yes	0.611	0.150	0.551	0.636	0.350	0.086	0.120	0.611	0.054
yes	3.054	0.150	0.564	0.583	0.329	0.062	0.048	0.611	0.270
base		0.300	0.418	0.751	0.314	0.100			
no	0.001	0.300	0.408	0.774	0.316	0.087	0.108	0.940	0.000
no	0.940	0.300	0.423	0.765	0.323	0.063	0.082	0.940	0.083
yes	0.940	0.300	0.423	0.827	0.350	0.063	0.082	0.940	0.083
yes	4.698	0.300	0.432	0.778	0.336	0.047	0.027	0.940	0.416

DMFC STACK FLOW FIELD PRESSURE DROP STUDY

Several different bipolar plate flow field designs have been proposed for a DMFC stack by Ming, Chuck and Simon.. We have evaluated some of the dimensions needed to get proper flow balancing in three of the designs and have determined the approximate pressure drop expected for each. The cell area of each is 50 cm^2. In order to minimize the thickness of each cell, the bipolar plate is formed from a metal foil between the methanol electrode of one cell and the adjacent air electrode of the next cell in series. The foil is shaped with a series of ridges extending from the midplane to either the adjacent air or methanol electrodes maintaining a total electrode spacing of approximately 63 mils between adjacent electrodes of neighboring cells. The shaping can form channels for methanol and air flow on the two sides of the foil. The exercise is to distribute the flow uniformly over the entire cell area, keep the entrance and exit feed paths design simple to fabricate, and have reliable and simple sealing.

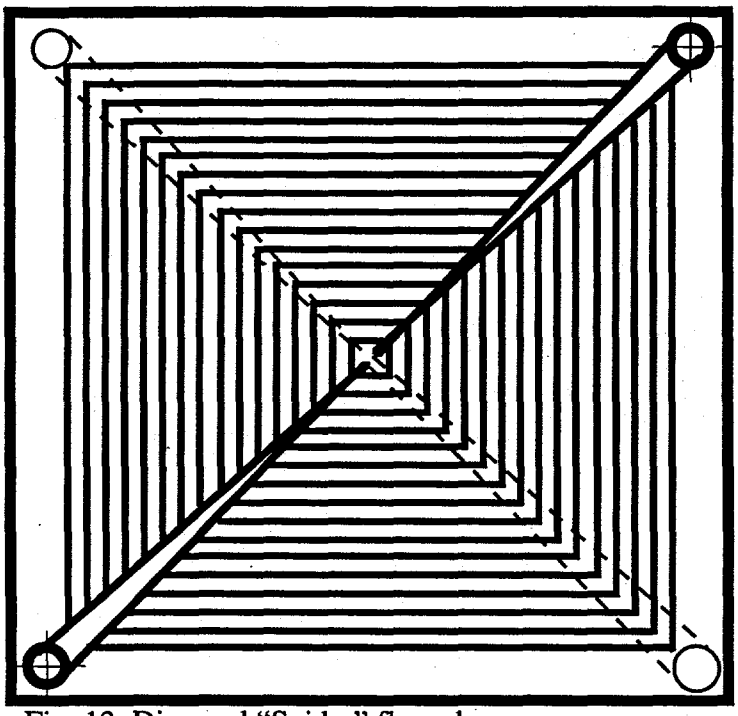

Fig. 13 Diagonal "Spider" flow shape.

The first potential design, referred to as "Spider" and one that has been discarded at present as being too difficult to implement quickly, is shown in Fig. 13. In the drawing the black lines represent methanol flow channels and the white spaces between represent the air channels. Details of the diagonal flow channels and the actual foil shape can better be understood by viewing Fig. 14, which shows a bottom and a top view of a three dimensional foil surface with 3 channels instead of 16. In order to have approximately uniform flow through each of the parallel channels, it is necessary to vary the channel widths, a detail not shown in either Fig. 13 or 14. The method and results of calculating widths of these channels will be given in the next section. The calculated channel widths

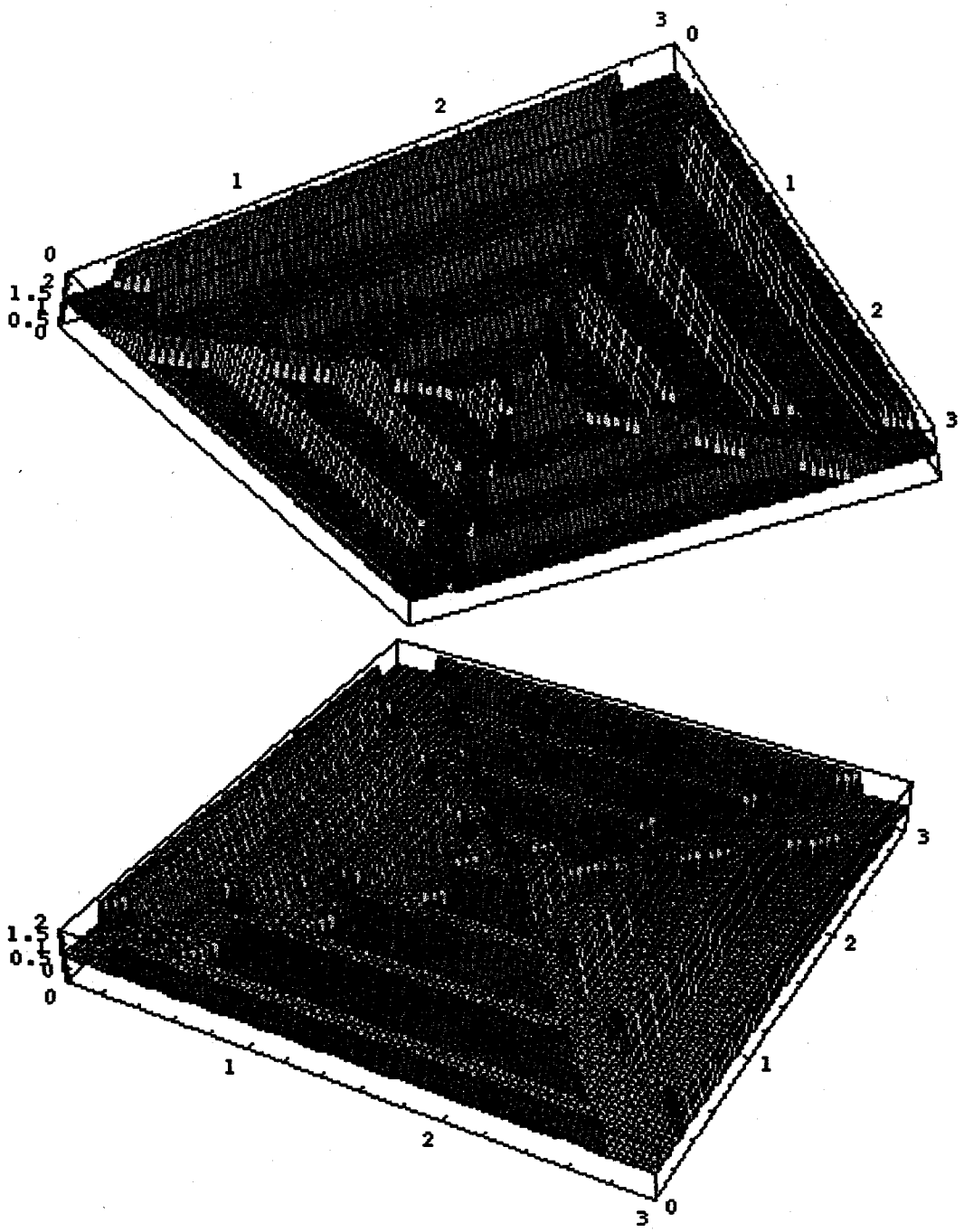

Fig.14. Three D surface plot of a smaller diagonal "Spider" flow design.

assuming laminar flow with no additional pressure drop for lengths are proportional to 1, 2, 3...., 16 are given in Table IV. Distances are measured from the diagonal line. The length of the shortest channel L_1 determined from the total area A and the widths w of the 16 methanol channels , 16 air channels, and the foil thickness.

$$\frac{A}{2} = L_1 \sum_{i=1}^{16} i\left(w_i^m + w_i^a + 2w^f\right) \qquad [46]$$

The sum of the methanol channel widths is designed to be one half the sum of the air channel widths. Note that for the shorter lengths the air to methanol channel width ratios are less than 2 and for the longer lengths are greater than 2. The pressure drop across each channel is the same, the drop along the diagonal feed channel is negligible. The advantage of this design is that there is no external manifolding required and that there is a low pressure drop. The methanol enters at one corner and exits diagonally opposite with the flow being on the bottom side of the foil. The air likewise flows between the remaining two opposite corners, but on top of the foil where the channel widths are on the average twice as wide as the methanol channels. The supporting frame for the foil is represented by the enclosing box with arbitrary numbers. Feed ports pass through this frame at the corners either above or below the foil. When passing the corner half way between entrance and exit, there is an open region between parallel channels, but no flow should pass between the channels because the pressures are the same. We have used a Fortran program to generate the data for Mathematica to render the surface plots for any of the foil designs for bipolar DMFC stack flow fields.

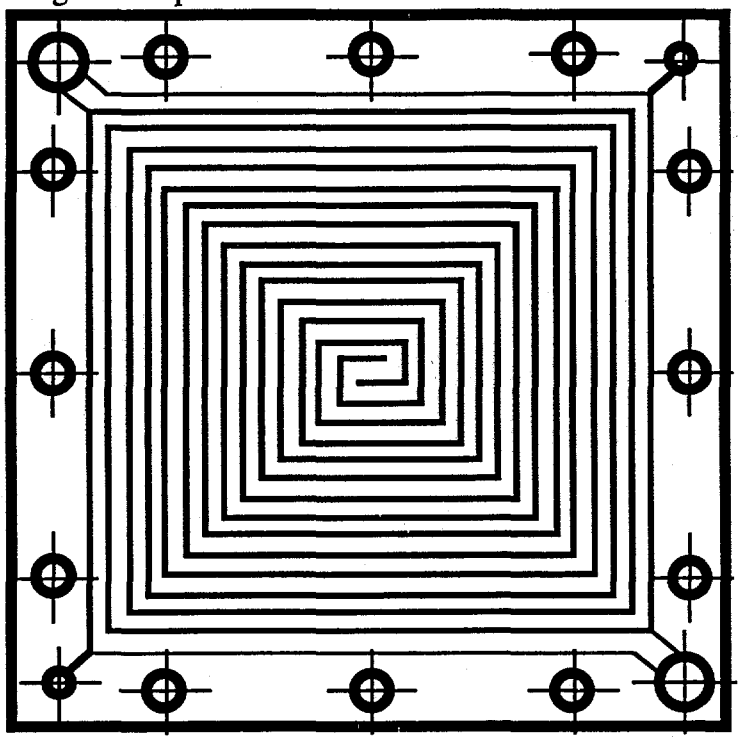

Fig. 15. Spiraling single series channel design.

The next design, referred to as "Spiral", shown in Fig. 15 is a single channel that spirals to the center and out to the diagonally opposite corner with the remaining two corners being used for the flow of the other reactant. The air channels are twice the width of the methanol channel. Figure 16 is a 3D rendering of the foil shape with only 5 instead of 16 spirals. Here we can see the center where the foil returns to mid plane to allow the methanol and air to pass from the ingoing spirals to the outgoing ones. The 90° corners are actually rounded to cut turbulence and maintain laminar flow. This design has a much

higher pressure drop than the first design but the channel widths remain constant and uniform flow is assured. As in Fig. 12, the black lines represent the methanol channels and the white the air channels. In the center the foil returns to midplane to allow the methanol path to cross below the air path.

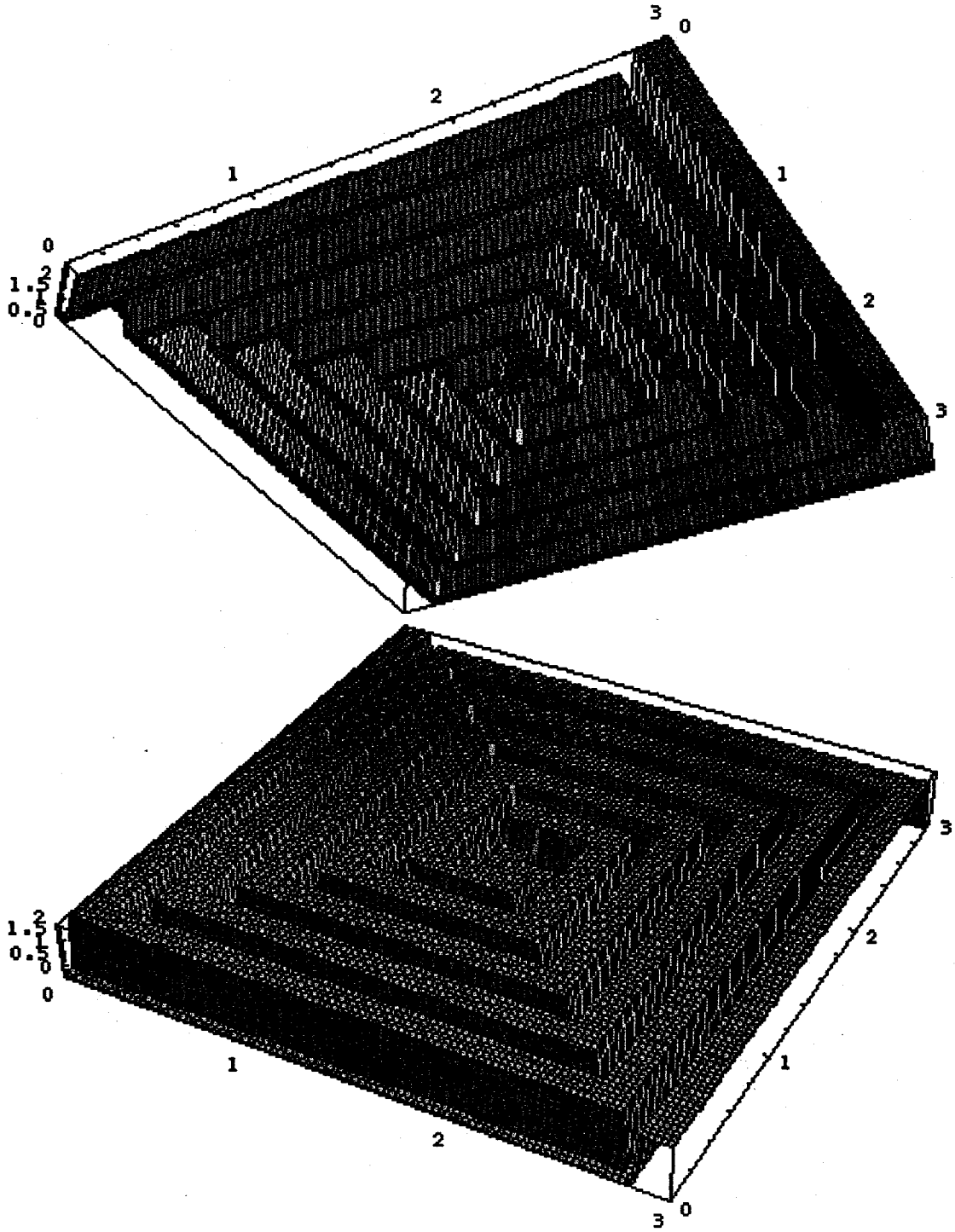

Fig. 16. 3 D surface of smaller spiral design.

TABLE IV. Channel width in mils for 16 channel lengths for 2 depths for a 50 cm^2 cell.

Length Ratio	Depth MeOH	30 mils Air	Depth MeOH	50 mils Air ir
1	10.8	17.5	11.8	20.7
2	14.1	23.5	15.1	27.1
3	16.5	28.3	17.5	32.0
4	18.6	32.7	19.5	36.2
5	20.4	37.0	21.2	39.9
6	22.1	41.0	22.7	43.4
7	23.7	45.0	24.1	46.6
8	25.1	48.8	25.4	49.7
9	26.5	52.7	26.6	52.8
10	27.9	56.4	27.8	55.9
11	29.2	60.2	28.9	58.8
12	30.5	63.9	29.9	61.7
13	31.8	67.7	30.9	64.6
14	33.0	71.4	31.9	67.4
15	34.3	75.1	32.9	70.2
16	35.5	78.8	33.8	72.9
TOTALS	399.9	799.9	399.9	799.9

The third design, referred to as "Internal Manifold", shown in Fig. 17 has internal manifolds to split the methanol and air flows into 47 and 46 parallel channels respectively for the initial single cell machined from aluminum end plates and which would probably drop to 41 and 40 channels when 6 mil foil is used. Figure 18 shows a foil for a smaller 8 channel version. Methanol enters the back left and exits the right front corner. The frame through which methanol and air pass is not shown. Air enters and through six holes to the air manifold on each side.

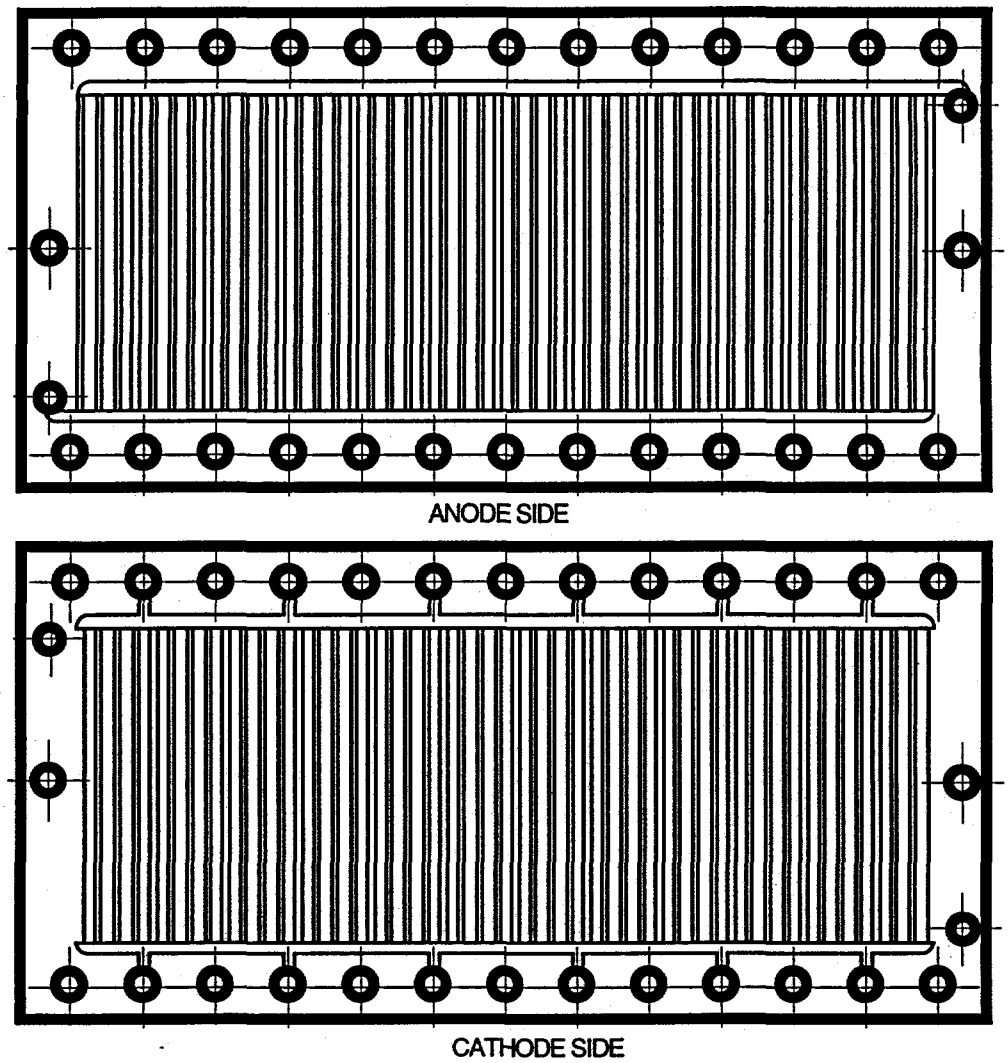

Fig.17. Internally manifolded parallel flow design..

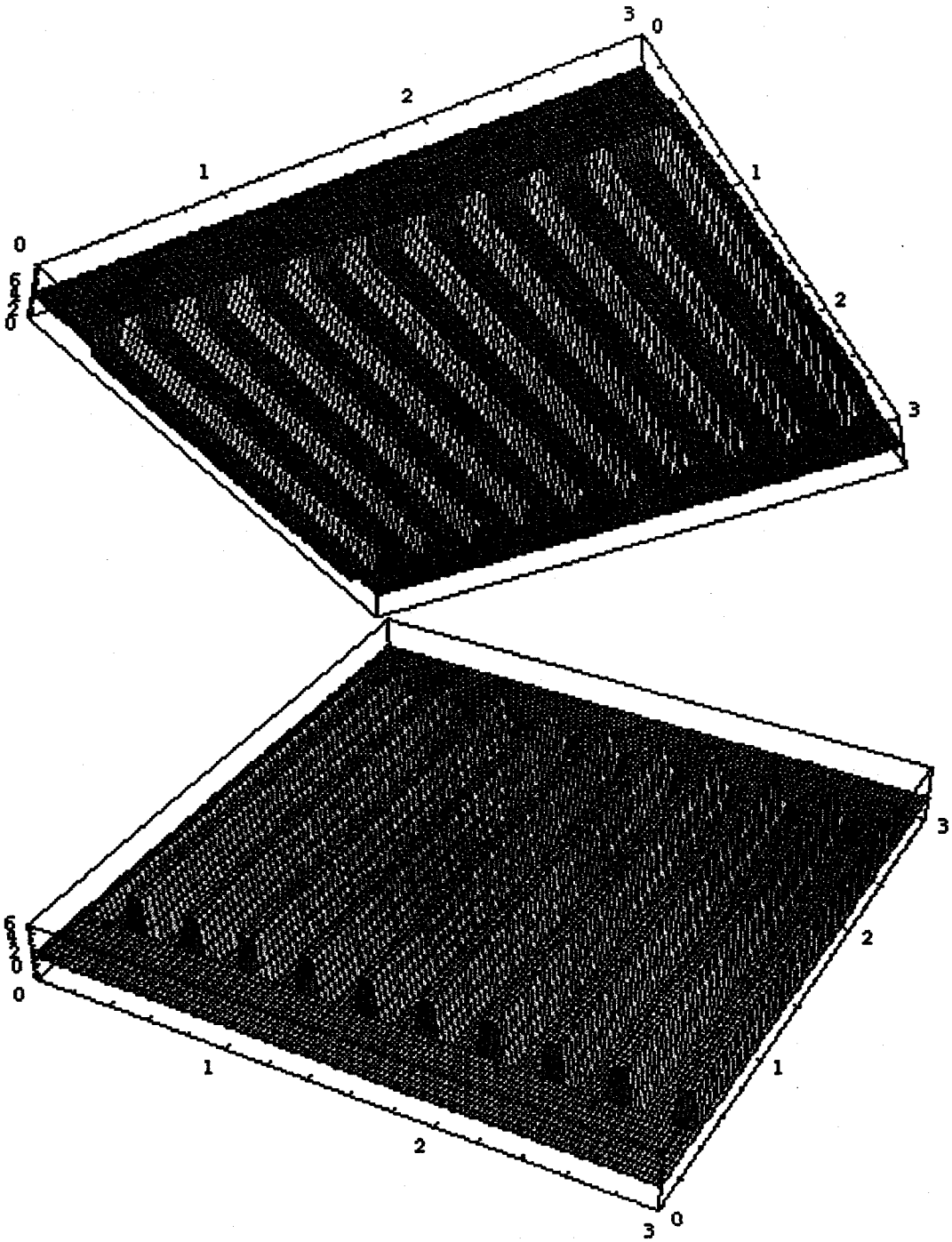

Fig. 18. 3 D surface of a smaller internal manifold parallel flow design

Pressure-Flow Relations

Methanol and air flows will be calculated for 150 mA/cm^2 current density in a 50 cm^2 cell or 7.5 A/cm^2 at 1 atm and 80°C.. The methanol flow for 1 Stoich for 1 mol/l methanol concentration is

$$\frac{7.5\ \text{A}}{6\ \text{F C/mol}} = 1.3\times10^{-5}\frac{\text{mol}}{\text{s}}\times\frac{1000\ \text{cm}^3}{\text{mol}} = 0.013\frac{\text{cm}^3}{s}\times 60\frac{\text{s}}{\text{min}} = 0.78\frac{\text{ml}}{\text{min}}$$

The air flow for 1 stoich is:

$$\frac{7.5\ \text{A}}{4\text{F C/mol}} = 1.94\times10^{-5}\frac{\text{mol O}_2}{\text{s}}\times\frac{22414\times353/273\ \text{cm}^3\ \text{O}_2}{0.21\ \text{cm}^3\ \text{O}_2/\text{cm}^3\text{air}} = 2.677\frac{\text{cm}^3\ \text{air}}{\text{s}} = 160.6\frac{\text{ml}}{\text{min}}$$

We will use a 6 Stoich flow for methanol and a 3.5 Stoich flow for air in the three designs.

For a filled rectangular channel of height a and width b the volume flow rate q or the mass flow rate $\dot{m}$ divided by density is[16]:

$$q = \frac{\dot{m}}{\rho} = \frac{ab^3\Delta P}{\mu L\left(12.123+5.433(b/a)+10.836(b/a)^2\right)}, a \geq b. \qquad [47$$

If the width is greater than the height, the a and b are interchanged. Units are c.g.s. with cm, poise, and dyne/cm^2 for distances a, b, and L, viscosity μ, and pressure drop ΔP respectively. The viscosity for the methanol is taken as that for water. The Reynold's number, a ratio of kinetic to viscous forces in the fluid, for a filled rectangular channel is $N_{Re} = \frac{\rho v}{\mu}\frac{2ab}{(a+b)} = \frac{2\rho q}{(a+b)\mu}$. The pressure drop associated with entrances to a laminar flow rectangular are determined by adding an equivalent entrance length L_e determined by the correlation L_e=h(0.39+.0363 N_{Re}). The numbers used here are a compromise between several sets of numbers discussed by Perry[16]. The distance h is the narrowest width of the channel.

Table V shows the internal and feed channel dimensions, and calculated pressure drops, velocity and Reynold's numbers expected in various portions of the three feed geometries. These calculations should only be considered rough estimates because the actual flow conditions are not well established. For the "spider" design the greatest drop is in the entrance. All the Reynolds number can be seen to be well below the 2100 level where transition from laminar to turbulent flow can occur. The greatest pressure drop occurs in the "spiral" design. The final "Internal Manifold" design appears to have a low pressure drop and a simple flow path if liquid does not block some of the passages.

Table V. Dimensions, pressure drop, velocity and Reynolds number for various portions of the three design feed geometries. Anode flow is 0.79.8 ml/min and cathode flow is 160.6 ml/min.

SPIDER

32 Parallel Channels - Same flow see Table IV - shortest and longest

	a cm	b cm	L cm	L_e cm	ΔP psi	VEL cm/s	N_{REY}
MeOH L_1	.0762	.0274	0.815	0.0239	$9.0 \cdot 10^{-4}$*	1.16	13.3
Air L_1	.0762	.0445	0.815	0.0542	$1.9 \cdot 10^{-3}$*	86.6	22.9
MeOH L_{16}	.0762	.0902	13.04	0.0525	$9.0 \cdot 10^{-4}$*	0.35	8.3
Air L_{16}	.0762	.2002	13.04	0.0574	$1.9 \cdot 10^{-3}$*	19.2	10.0
			Single Entrance				
MeOH	.0787	.1588	0.639	0.339	$1.1 \cdot 10^{-3}$	6.2	185
Air	.0787	.1588	0.639	0.651	$1.1 \cdot 10^{-2}$	750	372

* entrance pressure not added to show that the short and long channel ΔP's are equal

SPIRAL

Single Channel

	a cm	b cm	L cm	L_e cm	ΔP psi	VEL cm/s	N_{REY}
MeOH	.0762	.0762	193	0.827	0.66	13.4	288
Air	.0762	.1524	193	1.100	1.47	807	387
			Single Entrance				
MeOH	.0787	.3175	0.639	0.339	$1.1 \cdot 10^{-3}$	6.2	185
Air	.0787	.3175	0.639	0.651	$1.1 \cdot 10^{-2}$	750	372

INTERNAL MANIFOLD

40 Parallel Channels

	a cm	b cm	L cm	L_e cm	ΔP psi	VEL cm/s	N_{REY}
MeOH	.0889	.0794	4.128	0.827	$2.4 \cdot 10^{-4}$	0.28	6.5
Air	.0889	.1588	4.128	1.100	$5.1 \cdot 10^{-3}$	16.6	8.9
			Single Plenum HalfFlow Total Length				
MeOH	.0381	.1588	11.43	0.169	$3.8 \cdot 10^{-2}$	6.4	112
			6 Air Feed Channels				
Air	.0508	.1588	0.508	0.150	$2.3 \cdot 10^{-3}$	194	223
			Single Feed Channel				
MeOH	.0508	.1588	1.63	0.32	$1.3 \cdot 10^{-2}$	12.9	223

TASK 3 COMPUTER CODES

In order to display properly the contour lines of constant potential or concentration obtained from the Laplace equation solver[15] for some of the tubulated membrane, it was necessary to write a new contour plotting program, CONDR. The Lynntech geometry indicated in Fig. 9a is such a case. Data for contour plotting consists of potentials computed on a rectangular grid of up to 100 by 100 points. When the points on the grid fall outside the problem area as above and to the left of the anode side or above and to the right of the cathode side, a special number (-1.e-20) is inserted to indicate no contour is to

be plotted. This worked properly in the past on the large LANL computers where NCAR contour plotting routines were used, but such routines were not available conveniently for use on the Macintosh computer. In the near past we had partly solved the problem by setting points outside the boundary equal to the potential of the nearest boundary, so no contour lines would show in that region, but this doesn't work when, with a Neumann boundary (no current flow), the potential varies along the boundary. The new CONDR routine generates the plotting vectors and thus does not plot in the regions that contain the special number.

The FORTRAN source and execution codes developed for this task are stored in the same computer indicated in Task 1 and in the directories TES HD/MPW/MEOH or TES HD MPW/LARECT/LAP MEOH. Source codes have ".f" appended to the program name. NEWCATH is the new cathode model. ETANODE is the methanol anode model with electronic and ionic resistance. LARECTEL is the general Laplace solver modified to handle elliptical boundaries. CIRTUBE, LYNNTUBE and LARTUBE include the Laplace solver for which the boundary data are automatically generated and the transport coefficients (R_{ac}, R_{at}, R_{tc}, and R_{res}) are calculated for the circular tube - flat edge geometry, Lynntech geometry, and elliptical tube - flat edge geometry. TUBEPERF evaluates the cell performance with and without recycling, generating Tables II and III. FKAB calculates pressure drops, velocities and Reynold's numbers for rectangular channel laminar flow. SHOWFEED and FEED100 generate data files to be read by a MATEMATICA program that generated Fig. 14, 16 and 18.

TASK 3 CONCLUSIONS

In this task we have developed a calculational method of determining the anode and cathode overpotentials, including catalyst layer resistance and concentration effects that require only iteration on simple implicit functions and do not require integration or matrix solving. These should be useful for systems studies such as was done here for the tubulated membrane.

We showed that electrode overpotential from ionic and electronic resistance is increased if the resistance is split between the two, rather than being exclusively one or the other.

We developed simple equations for the concentration and fluxes in the DMFC considering diffusion and electroosmotic drag, but showed that with concentrations no higher than 1 M it was reasonable to analyze the tubulated membranes ignoring drag in order to eliminate for a minor effect the lengthy development of two dimensional transport codes modeling both diffusion and drag.

For the parameters we used in the model, which reasonably match those observed in the lab, we determined that Nafion 117 has a relatively well optimized thickness for its conductivity and diffusional properties.

If we choose, Lynntech, Inc. will sell us a tubulated membrane and attached electrodes and will loan us a fixture to test it. We have developed codes to evaluate the effect of tubulated membranes decreasing methanol flux to the cathode by calculating cell

voltage, fuel efficiency, and total efficiency. We found the Lynntech membrane could improve total efficiency by 6% by recycling and mixing with neat methanol.

The best increase in total efficiency was 25 % achieved with flat edged membranes containing circular tubes whose diameter was half the total membrane thickness and with the anode-facing half of the tubes made impermeable. The pressure requires to flow water through the tubes was less than 0.5 psi for flows 5 times the recycle rate, so that is are no problem.

In general, recycling e crossover methanol using tubulated membranes may hold some promise, but more detailed study and experiment need to be done before any final conclusions.

Pressure drop and velocities were calculated for some bipolar metal foil flow fields. Pressure drop of 1.5 psi is expected in the Spiral design. We found use of the 3D surface plotting capability in MATHEMATICA® provides a good method for describing the shapes of these flow fields.

REFERENCES

1. H. A. Gasteiger, N. Marcovic, P. N. Ross, and E. J. Cairns, *J. Electrochem. Soc.* **141,** 1795 (1994).
2. T. E. Springer, M. S. Wilson and S. Gottesfeld, *J. Electrochem. Soc.* **140,** 3513 (1993).
3. T. A. Zawodzinski, C. Derouin, S. Radzinski, R.J. Sherman, V. T. Smith, T. E. Springer, and S. Gottesfeld, *J. Electrochem. Soc.* **140**, 1041 (1993).
4. T. A. Zawodzinski, J. Davey, J. Valerio, and S. Gottesfeld, *Electrochimica Acta* **40**, 297 (1995).
5. X. Ren, T. A. Zawodzinski, F. Uribe, H. Dai, and S. Gottesfeld, in *Proton /conducting Membrane Fuel Cells 1*, S. Gottesfeld, G. Halpert, and A. Landgrebe, Eds. (The Electrochemical Society, Pennington, NJ, 1995), p. 284.
6. X. Ren, T. A. Zawodzinski, F. Uribe, H. Dai, and S. Gottesfeld, in *Proton /conducting Membrane Fuel Cells 1*, S. Gottesfeld, G. Halpert, and A. Landgrebe, Eds. (The Electrochemical Society, Pennington, NJ, 1995), p. 284.
7. T. E. Springer, T. A. Zawodzinski, and S. Gottesfeld, *J. Electrochem. Soc.* **138,** 2334 (1991).
8. M. S. Wilson and S. Gottesfeld, *J. Appl. Electrochem.* **22**, 1 (1992).
9. X. Ren, W. Henderson, and S. Gottesfeld, *J. Electrochem. Soc.* **144,** L267 (1997).
10. S. Gottesfeld, I. D. Raistrick, and S. Srinivasan,*J. Electrochem. Soc.* **134,** 1455 (1987).
11. D. A. Gough and J. K. Leypoldt, *Anal. Chem.* **51,** 439 (1979).
12 M. S. Wilson, *private communication.*

13. O. J. Murphy, A. J. Cisar, A. Gonzalez-Martin, C. E. Salinas, and S. F. Simpson, "*A Novel Untized Proton Exchange Membrane Fuel Cell*", NASA Conference Publication 3337, Space Electrochemistry Research and Technology Conference, NASA Lewis, Cleveland, OH (May 1-3, 1995).

14. X. Ren, *private communication.*

15. J. K. Hayes, "Four Computer Programs Using Green's Third Formula to Numerically Solve Laplace's Equation in Inhomogeneous Media", Los Alamos Scientific Laboratory Report LA-4423 (1970).

16. R. H. Perry and D. W. Green, Chemical Engineers' Handbook 6th Ed, McGraw-Hill (1984).